Technische Universität München

TUM School of Natural Sciences

CO_2 hydrogenation to C_2+ products with the adjustment of intermediates

Chuanlei Li

Vollständiger Abdruck der von der TUM School of Natural Sciences der Technischen Universität München zur Erlangung des akademischen Grades eines

Doktors der Naturwissenschaften (Dr. rer. nat.)

genehmigten Dissertation.

Vorsitz: Prof. Dr. Jennifer Strunk

Prüfer der Dissertation:

1. Prof. Dr. Johannes A. Lercher

2. Prof. Dr. Max J. Hülsey

Die Dissertation wurde am 15.12.2025 bei der Technischen Universität München eingereicht und durch die TUM School of Natural Sciences am 07.01.2026 angenommen.

Acknowledgements

Pursuing a PhD in chemical engineering has been one of the most intellectually and personally transformative experiences of my life. This thesis, centered on CO_2 hydrogenation and catalytic system design, is the culmination of not only rigorous academic work but also countless moments of collaboration, mentorship, and inspiration across disciplines and borders.

First and foremost, I would like to express my profound gratitude to my supervisor, Prof. Johannes A. Lercher, for their exceptional guidance, academic integrity, and continuous encouragement. Their deep knowledge in heterogeneous catalysis, kinetic mechanisms, and reaction engineering has profoundly shaped my understanding of how fundamental science can address pressing global challenges, such as carbon neutrality and sustainable fuel production. The freedom they gave me to explore complex reaction networks, coupled with their unwavering support at critical moments, was invaluable in defining the scientific direction of this work.

I am sincerely thankful to the mentor (Dr. Ruixue Zhao), the research group members and colleagues at the School of Natural Sciences, Technical University of Munich, whose technical expertise and intellectual generosity made this journey collaborative and rewarding. I am also deeply appreciative of the collaboration and support from my group members and colleagues Rachit Khare, Wei Zhang, Yue Ma, Fuli Deng, Hongwen Chen, Yifei Ye, Yunxiang Sheng, Wenshu Wang, Xiaomai Chen, Tao Yin, Yuyang Fan, Bettina Federmann, Markus Drees, Rafael Holtmann and Jibin Thomas, whose contributions have been invaluable both academically and in daily life. From long days in the lab synthesizing and characterizing catalysts using techniques such as operando XRD, H_2 chemisorption, TPR, BET, and the fixed bed reactor, to late night discussions finalizing setups and analyzing product (Paraffins/olefins, ethanol, DME) selectivity and intermediate coupling pathways, every moment was enriched by their contributions. From daily scientific files to defense process, every event was unforgettable. The freedom and difficulties they gave me to explore complex reaction networks, coupled with their unwavering support at critical moments, was invaluable in defining the scientific direction of this work. I would also like to acknowledge the administrative and technical staff who ensured a smooth and efficient environment for research.

This journey would not have been possible without the broader support from Technical University of Munich and the generous funding from Chinese Scholarship Center, which enabled access to state-of-the-art facilities and high-level collaborations. I extend my gratitude to international collaborators and visiting scholars whose insight brought invaluable perspective to our work on multi-functional catalysts, CO_2 valorization strategies, and catalyst deactivation mitigation.

Living and studying in Germany has been a truly enriching experience. Beyond the academic rigor, I have found deep appreciation for the cultural diversity, the rhythm of everyday life, and the welcoming spirit of the people. The opportunities to engage with a global community of researchers, to navigate life in a multilingual and multicultural environment, and to explore both the urban and natural landscapes of this country, have left a lasting mark on my personal development. This country's remarkable natural beauty offered not only academic inspiration but also a personal spatial realization. Weekend hikes through its mountains, forests, and coastal trails became an essential part of my routine-a space for reflection, clarity, and resilience. These solitary moments in nature often mirrored the highs and lows of research: uphill challenges, unexpected detours, and, ultimately, rewarding views that made the effort worthwhile.

To my friends in and out of the lab, thank you for the laughter, solidarity, and encouragement that sustained me along this challenging but rewarding journey. Weekend hikes through your mountains, forests, and coastal trails became an essential part of my routine-a space for reflection, clarity, and resilience. Whether over shared meals, conference trips, or quiet late evenings spent revising manuscripts, your companionship reminded me that science is not only about knowledge but also about human connection. Over the past several years, hiking has become an integral part of my daily life, offering both resilience during challenging times and joy during moments of celebration. The shared experiences in the mountains have not only enriched my personal life but also strengthened bonds beyond the laboratory. I am especially grateful for the companionship of Wei Liang, Sheng Hu, Shenxi Zhong, Xu Jia, Chao Zhou, Wenxing Hu, Tao Yang, Qiao Yuan, Wei Ding and Tianxu Huang, whose presence during these hikes has made the journey both memorable and meaningful.

To my family, whose love transcends distance and time zones: your belief in me gave me strength even when experiments failed, and the finish line seemed far away. Your unwavering support has been the quiet force behind everything I have achieved.

To my exam committee, thank you for your support without any hesitation, innovative ideas for my research that helped me a lot in future research.

Last but not least, I would like to express my deepest gratitude to my country, the People's Republic of China, for its unwavering support throughout the past several years. This journey would not have been possible without the strong backing and encouragement I had received. Despite being far from home, the enduring connection to my country and loved ones has remained a constant source of strength and inspiration, especially during the most challenging times.

This thesis stands not only as a scientific contribution to the field of CO_2 hydrogenation, but also as a testament to the people and places that have shaped this journey.

真理与自由在实践这里获得统一！

Abstract

The selective hydrogenation of CO_2 into value added chemicals remains a critical challenge in sustainable catalysis, particularly in steering product distribution toward paraffins, olefins, higher alcohols and Dimethyl ether (DME). In this study, we present a comprehensive investigation into three classes of multifunctional catalysts, each rationally designed to address key mechanistic bottlenecks in the CO_2 hydrogenation pathway. Sodium (Na)-modified Co_3O_4 catalysts selectively promote light hydrocarbon formation of C_2-C_5 paraffins and olefins, modifying the amount of CH_2 and CH_3 intermediates by adjusting the ratio of metallic cobalt and $Co^{\&+}$. $CoCuZrO_x$ and Na-promoted catalysts enable selective ethanol synthesis by leveraging the CH_x and CH_xO intermediate forming ability of Cu-Zr interfaces and the C-C coupling propensity of fcc-Cobalt with a lower CO* desorption energy. Additionally, a bifunctional CuZr-H-MCM-22 catalyst achieves one-pass DME synthesis via the integration of methanol formation and acid-catalyzed dehydration at spatially organized redox and Bronsted acid sites. Collectively, these systems provide mechanistic insights and material design strategies for the tailored transformation of CO_2 into specific chemical targets.

Kurzzusammenfassung

Die selektive Hydrierung von CO_2 zu wertvollen Chemikalien stellt nach wie vor eine große Herausforderung in der nachhaltigen Katalyse dar insbesondere in Bezug auf die gezielte Steuerung der Produktverteilung hin zu Paraffinen, Olefinen, höheren Alkoholen und Dimethylether (DME). In dieser Studie präsentieren wir eine umfassende Untersuchung dreier Klassen multifunktionaler Katalysatoren, die jeweils gezielt entwickelt wurden, um zentrale mechanistische Engpässe im Reaktionsweg der CO_2 Hydrierung zu überwinden. Natrium (Na)-modifizierte Co_3O_4 Katalysatoren fördern selektiv die Bildung leichter Kohlenwasserstoffe (C_2-C_5 Paraffine und Olefinen), indem sie die Menge an CH_2 und CH_3 Intermediaten durch Anpassung des Verhältnisses von metallischem Cobalt zu $Co^{\&+}$ steuern. $CoCuZrO_x$ und Na-dotierte Katalysatoren ermöglichen die selektive Ethanolsynthese, indem sie die Fähigkeit der Cu-Zr Grenzflächen zur Bildung von CH_x und CH_xO Intermediaten nutzen und gleichzeitig die C-C Kopplungsneigung von fcc-Cobalt mit einer geringeren CO* Desorptionsenergie ausschöpfen. Darüber hinaus erreicht ein bifunktionaler CuZr-H-MCM-22 Katalysator die einstufige DME-Synthese durch die räumliche Integration von Methanolbildung und säurekatalysierter Dehydratisierung an gezielt angeordneten Redox und Bronsted-Säurezentren. Zusammengenommen liefern diese Systeme mechanistische Einblicke und Strategien für das materialgestützte Design zur gezielten Umwandlung von CO_2 in spezifische chemische Produkte.

Table of Contents

List of Figures

List of Tables

Abbreviations

STY	**Space time yield**
DME	**Dimethyl ether**
CCUS	**Carbon capture, utilization and storage**
BET	**Brunauer-Emmett-Teller**
CO	**Carbon monoxide**
CO_2	**Carbon dioxide**
CH_4	**Methane**
C_2H_5OH	**Ethanol**
GC	**Gas chromatography**
h	**Hour**
(k)J	**(Kilo) joule**
(k)Pa	**(Kilo) pascal**
(m)L	**(Milli) liter**
min	**Minute**
nm	**Nanometer**
SEM	**Scanning electron microscopy**
TOF	**Turnover frequency**
TPR	**Temperature programmed reduction**
wt.%	**Weight percent**
XRD	**X-ray diffraction**
XPS	**X-ray photoelectron spectroscopy**
AAS	**Atomic absorption spectroscopy**
TPD	**Temperature programmed desorption**
ΔH	**Enthalpy**
R	**Gas constant**
T	**Absolute temperature**
n	**molar**
E_a	**Apparent activation energy**
DRIFTS	**Diffuse reflectance infrared fourier transform spectroscopy**

Chapter 1

Introduction

1.1 General background of CO_2

Carbon dioxide (CO_2) is one of the most important greenhouse gases (GHGs)[1] in earth's atmosphere, playing a critical role in climate regulation and the global carbon cycle. However, human activities, particularly the burning of fossil fuels and industrial processes, have significantly increased atmospheric CO_2 concentrations, leading to global warming and climate change. Understanding CO_2, its sources, impact, and potential utilization strategies is essential for addressing environmental challenges and developing sustainable solutions.

1.1.1 Properties and role in the carbon cycle

CO_2 is a colorless, odorless gas at standard temperature and pressure. It is a naturally occurring component of Earth's atmosphere and a key player in the carbon cycle[2], which involves processes such as photosynthesis, respiration, oceans as a carbon sink and geological carbon storage. The balance of these natural processes regulates atmospheric CO_2 levels. However, human activities have significantly disrupted this equilibrium, thus underscoring the urgent need for effective strategies to reduce carbon emissions and mitigate climate change.

The major contributors to CO_2 emissions include fossil fuel combustion, industrial processes, deforestation and land-use changes, and agriculture. Fossil fuel combustion from power generation, transportation, and industrial activities remains the dominant source of anthropogenic CO_2 emissions, driven by the reliance on coal, oil, and natural gas[3]. Industrial processes, such as cement production, steel manufacturing, and chemical synthesis, release substantial amounts of CO_2 as byproducts of chemical reactions. Deforestation and land-use changes further exacerbate CO_2 emissions by reducing the planet's natural carbon sinks, diminishing the ability of forests to absorb atmospheric CO_2. Meanwhile, agriculture contributes through soil degradation, biomass burning, and livestock-related methane emissions, which indirectly impact the carbon cycle. Addressing these emission sources requires a multifaceted approach, including transitioning to renewable energy, improving industrial efficiency, protecting forests, and adopting sustainable agricultural practices.

1.1.2 Impact on climate and environment

Excess CO_2 in the atmosphere leads to several environmental and climatic consequences like global warming, extreme weather events, ocean acidification, ice melting and sea-level rise, which highlight the urgent need for CO_2 emission reductions and sustainable management strategies[4]. A gradual and pervasive deterioration of the environment has been observed, with consequences for all living beings, including humans.

To combat rising CO_2 levels, scientists and policymakers are exploring various mitigation and utilization strategies from carbon capture, utilization, and storage (CCUS)[4], Renewable energy and decarbonization, natural climate solutions by afforestation and reforestation enhance CO_2 absorption by increasing forest cover and CO_2 to value technologies. The capture process can occur after combustion, before combustion, or via direct air capture, depending on the source. Captured CO_2 can be used to produce fuels, chemicals, building materials, or injected into oil fields for enhanced oil recovery. Alternatively, it can be stored in geological formations such as depleted oil and gas reservoirs or deep saline aquifers. CCUS is crucial for reducing emissions from hard-to-decarbonize sectors like cement, steel, and chemicals, and supports net-zero goals by preventing CO_2 from entering the atmosphere. Despite its potential, CCUS faces challenges such as high costs, infrastructure demands, and the need for strict monitoring and regulation.

1.2 World energy situation

1.2.1 Trends, challenges and future outlook

The global energy landscape is experiencing a pivotal transformation, driven by the convergence of rapid economic development, technological innovation, geopolitical dynamics, and escalating environmental concerns. While fossil fuels, like including coal, oil, and natural gas, which continue to account for the majority of global energy consumption, their dominance is increasingly challenged by the urgent need to decarbonize and transition toward low-carbon energy systems. This urgency is amplified by international commitments to climate goals such as those outlined in the Paris Agreement, prompting a surge in investment in renewable energy technologies, green hydrogen, and carbon capture, utilization, and storage (CCUS). As countries seek to diversify their energy portfolios and enhance energy security, the deployment of clean technologies, improvements in energy efficiency, and integration of smart grids are accelerating. Together, these trends signal not only a structural shift in how energy is produced and consumed, but also a strategic redefinition of national energy policies and industrial innovation pathways[5].

1.2.2 Global energy consumption and mix

Despite the rise of renewable energy, fossil fuels such as oil, coal, and natural gas still account for nearly 80% of the world's total energy consumption[6,7]. Coal remains a primary energy source in many industrialized and developing nations, particularly in China and India. However, renewable energy, including solar, wind, and hydropower, is experiencing rapid

expansion, contributing nearly 30% of global electricity generation. Additionally, nuclear power continues to play a crucial role in supplying low-carbon electricity, particularly in countries like the United States, France, and China.

Energy consumption varies significantly by region, reflecting economic development, industrialization, and policy priorities. China is the world's largest energy consumer, leading in both coal consumption and renewable energy investment. The United States remains a major producer and consumer, with a growing reliance on natural gas and renewables. Europe is at the forefront of clean energy transitions, aiming to reduce dependence on fossil fuels through ambitious decarbonization policies[8]. Meanwhile, developing nations, particularly in Africa, India, and Southeast Asia are experiencing rapid energy demand growth, driven by industrialization and urbanization.

1.2.3 Global carbon neutrality commitments (2030-2060)

Many countries have announced net-zero emissions targets in alignment with the Paris agreement. The European union (EU) has committed to achieving net-zero emissions by 2050 through the European green deal, while the United Kingdom, Japan and South Korea have set similar targets. China aims to peak carbon emissions by 2030 and reach carbon neutrality by 2060, while the United States has also pledged to achieve net-zero emissions by 2050. To reach these goals, significant milestones must be met. By 2030, there must be a sharp decline in fossil fuel dependency, rapid scaling of renewables, and the implementation of carbon pricing mechanisms. By 2040, a large-scale hydrogen economy and advanced carbon capture and storage (CCS) technologies will be essential. By 2050-2060, near-complete decarbonization of power, transport, and heavy industry sectors will be necessary to meet net-zero targets[9].

1.2.4 Key challenges in the global energy sector

The global energy system faces several pressing challenges. Energy security has become a critical issue due to geopolitical conflicts, such as the wars, which can disrupt global energy supply chains and increase volatility in oil and gas markets. Climate change remains a major concern, as fossil fuel combustion continues to be the largest contributor to global CO_2 emissions, necessitating a shift toward low-carbon alternatives[10]. Additionally, the transition to renewable energy requires significant investments in infrastructure and storage technologies to address intermittency issues. Energy affordability and accessibility also remain critical challenges, with over 700 million people worldwide still lacking access to electricity.

Looking ahead, the global energy sector is expected to undergo profound changes. Many nations have set net-zero emissions targets by 2030-2060, accelerating investments in green

energy and carbon-neutral technologies[11]. Hydrogen energy is emerging as a potential game-changer for decarbonizing industries, particularly in steelmaking, transportation, and energy storage. Energy efficiency measures, including smart grids and artificial intelligence-driven optimization, will play an essential role in reducing waste and enhancing sustainability. Additionally, decentralized energy systems, such as microgrids and distributed solar power, are gaining momentum, allowing local communities to become more self-sufficient in energy production.

1.3 Global carbon release and climate change

1.3.1 Global carbon release

Carbon emissions originate from both natural and anthropogenic (human-induced) sources. Fossil fuel combustion from coal, oil, and natural gas accounts for the majority of CO_2 emissions, contributing nearly 75% of total greenhouse gas emissions. Deforestation and land-use changes further exacerbate the problem by reducing the planet's ability to absorb CO_2. Additionally, industrial activities, such as cement production and chemical manufacturing, release significant amounts of carbon[12]. Agriculture is also a major contributor, with methane emissions from livestock and rice paddies adding to the greenhouse effect.

To combat climate change, international agreements and policies aim to reduce carbon emissions. The Paris agreement sets a global target to limit temperature rise to below 2 °C, with efforts to keep it under 1.5 °C above pre-industrial levels[13,14]. Governments and industries are investing in renewable energy, carbon capture and storage (CCS), energy efficiency, and reforestation efforts. Additionally, carbon pricing mechanisms, such as carbon taxes and cap-and-trade systems, are being implemented to incentivize emission reductions.

1.3.2 Impact on climate change

Rising carbon emissions have led to an increase in global temperatures, triggering climate change-related consequences such as: Rising sea levels due to polar ice melting and thermal expansion of seawater. More frequent and intense extreme weather events, including hurricanes, heatwaves, and droughts[15]. Disruptions to ecosystems and biodiversity, affecting food security and species survival. Ocean acidification, which threatens marine life, particularly coral reefs and shell-forming organisms.

1.4 The necessity of using CO_2

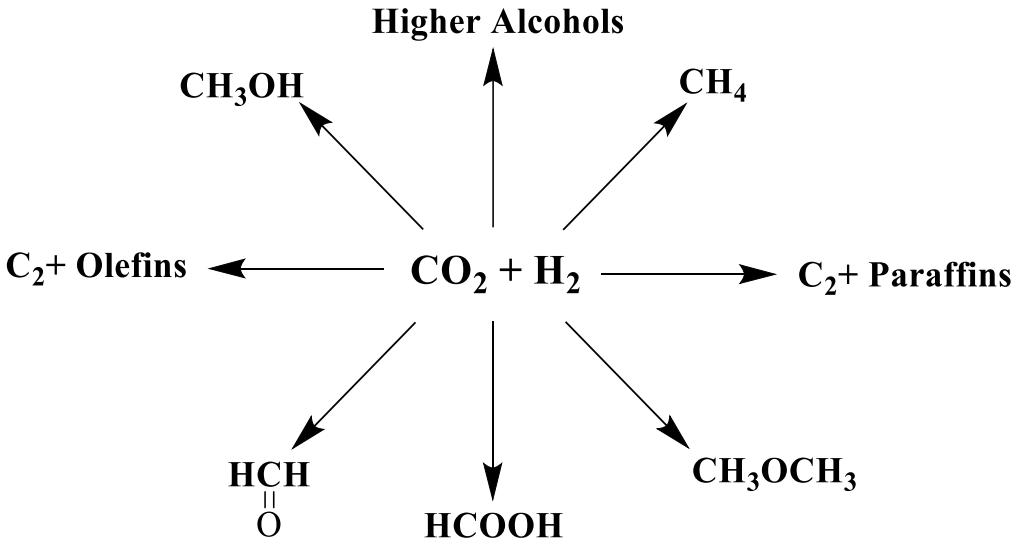

Figure 1-1 The possible products from CO_2 hydrogenation

1.4.1 CO_2 as a feedstock for chemical and fuel production

One of the most promising applications of CO_2 is its conversion into valuable chemicals and fuels. CO_2 hydrogenation can produce methanol, hydrocarbons, and alcohols, which serve as important intermediates in the chemical industry. Additionally, thermochemical, electrochemical and photocatalytic CO_2 reduction technologies aim to transform CO_2 into useful carbon-based fuels (**Figure 1-1**), such as synthetic methane or ethanol, providing a pathway for sustainable energy storage and utilization[16].

1.4.2 CO_2 utilization in carbon capture and storage (CCS) and carbon capture and utilization (CCU)

To mitigate climate change, carbon capture and storage (CCS) and carbon capture and utilization (CCU) technologies play a key role in reducing atmospheric CO_2 levels. In CCS, CO_2 is captured from industrial emissions and stored underground, preventing its release into the atmosphere. In CCU, captured CO_2 is recycled into useful products, such as building materials, plastics, or fuels, providing an economic incentive for carbon reduction[4,17].

1.4.3 CO_2 in enhanced oil recovery (EOR) and industrial applications

CO_2 is widely used in enhanced oil recovery (EOR), where it is injected into oil reservoirs to increase oil extraction efficiency while simultaneously storing CO_2 underground[18]. Additionally, industries use CO_2 for food and beverage carbonation (e.g., soft drinks), medical applications (e.g., anesthesia), and as a coolant in supercritical fluid technologies, demonstrating its versatility across multiple sectors.

1.4.4 CO_2 for sustainable agriculture and algae cultivation

CO_2 is essential for photosynthesis, making it a valuable resource for enhancing plant growth in greenhouses. Controlled CO_2 enrichment can boost crop yields while reducing water consumption. Moreover, microalgae cultivation using CO_2 can produce biofuels, animal feed, and bioplastics, offering a sustainable approach to carbon recycling and resource utilization[19].

1.5 CO_2 reduction technologies (Table 1-1)

1.5.1 Thermochemical CO_2 reduction

High-temperature reactions offer a pathway for CO_2 conversion into valuable fuels and chemicals, leveraging thermal catalytic processes to achieve high conversion efficiencies. One such reaction is the reverse water-gas shift (RWGS) reaction, which reduces CO_2 to CO using hydrogen. This CO can then serve as a key intermediate for Fischer-Tropsch synthesis, enabling the production of hydrocarbons and oxygenates. The RWGS reaction is particularly attractive for CO_2 utilization due to its compatibility with syngas-based industrial processes, though challenges such as equilibrium limitations and catalyst stability at elevated temperatures must be addressed to enhance efficiency and selectivity[20].

1.5.2 Carbon capture and storage (CCS)

Carbon capture and storage (CCS) is a widely explored strategy for mitigating CO_2 emissions from industrial and energy sectors, comprising three fundamental stages. Capture involves the separation of CO_2 from flue gases in power plants and industrial facilities through absorption (e.g., amine scrubbing), adsorption, or membrane-based technologies. Transport follows where the captured CO_2 is conveyed via pipelines or shipping networks to designated storage sites. Storage is achieved by injecting CO_2 into deep geological formations, such as depleted oil and gas reservoirs or saline aquifers, ensuring long-term sequestration. While CCS presents a viable pathway for reducing emissions from fossil fuel dependent industries, its widespread deployment is hindered by challenges including high operational costs, energy-intensive processes, and public concerns regarding the safety and permanence of underground storage. Advancements in cost-effective capture technologies, policy incentives, and public engagement strategies are critical for facilitating large scale CCS implementation[21].

1.5.3 Carbon capture and utilization (CCU)

Table 1-1 The comparison of different technologies for CO_2 hydrogenation

Technologies for CO_2 hydrogenation	Energy source	Products	Advantages	Disadvantages
Thermo-catalysis	Heat	CO, MeOH, CH_4, C_2+	1. At industrial levels 2. Tandem routes for value-added chemicals 3. High product outputs	1. Excessive energy consumption 2. Inferior selectivity 3. Poor stability 4. Coke formation
Photocatalysis	Sunlight	CO, MeOH, CH_4	1. Renewable solar energy 2. Sunlight sensitivity 3. Simple reactors	1. Low energy efficiency 2. Inferior selectivity 3. Poor stability
Electrocatalysis	Electricity	CO, MeOH, Formic acid, CH_4, C_2+	1. Highly controllable 2. Energy-efficient 3. Renewable-compatible platform	1. Low product selectivity for C_2+ Products 2. Limited current density and reaction rate 3. High overpotentials and energy inefficiency 4. Catalyst instability and degradation
Biological catalysis	Sunlight, biomass	CO, Formic acid, CH_4, Alcohols	1. High selectivity 2. Mild reaction conditions 3. Environmentally friendly & biodegradable	1. Slow reaction rates and low productivity 2. Sensitivity to temperature, pH, and contaminants 3. Requires careful control of microbial environment 4. Difficult product recovery in some systems

Instead of storing CO_2, CCU technologies aim to convert CO_2 into valuable products, integrating economic benefits with environmental sustainability. Some promising CCU applications like mineralization that CO_2 reacts with alkaline materials to form stable carbonates used in construction (e.g., concrete production), chemical synthesis that CO_2 can be used as a feedstock for producing methanol, urea, and polycarbonates in the chemical industry and fuel production that CO_2 can be converted into synthetic fuels such as methane, methanol, or gasoline through catalytic hydrogenation[22]. While CCU provides economic incentives, its scalability depends on energy efficiency, catalyst development, and the availability of renewable hydrogen for CO_2 conversion.

1.5.4 Electrochemical CO_2 reduction reaction (CO_2RR)

Electrochemical CO_2 reduction uses electricity to convert CO_2 into fuels and chemicals through catalytic processes. This method can produce: Carbon monoxide, a precursor for synthetic fuels. Formic acid (HCOOH), used in fuel cells and the chemical industry. Hydrocarbons (e.g., ethylene, ethanol), potential renewable energy carriers. The efficiency of CO_2RR depends on catalyst design, electrode materials, and renewable electricity sources[23]. Recent advances in nanomaterials and electrocatalysts have improved selectivity and conversion efficiency.

1.5.5 Photocatalytic and photoelectrochemical CO_2 reduction

Photocatalytic and photoelectrochemical (PEC) technologies harness solar energy to drive CO_2 reduction, mimicking the principles of artificial photosynthesis. Photocatalysis utilizes light activated catalysts, such as TiO_2 and metal organic frameworks, to facilitate the conversion of CO_2 into value-added products like methane and methanol. PEC reduction, in contrast, integrates light absorption with electrochemical CO_2 conversion, enabling direct solar to fuel energy conversion. While these approaches offer a sustainable route for CO_2 utilization, challenges including low conversion efficiency, limited selectivity, and catalyst stability must be overcome to enable practical implementation[24]. Advancements in catalyst design, charge carrier management, and reaction engineering are essential to enhance the efficiency and scalability of solar driven CO_2 reduction technologies.

1.5.6 Biological CO_2 reduction

Microorganisms and engineered biological systems can convert CO_2 into valuable products. Examples include microalgae cultivation that algae use CO_2 for photosynthesis, producing biomass for biofuels and bioplastics[25]. Synthetic biology approaches: Engineered microbes can convert CO_2 into biochemicals, biofuels, or proteins. Biological methods are attractive due to their mild reaction conditions and potential for large scale carbon recycling, but they require optimization for higher yields and cost effectiveness.

1.6 Challenges in catalyst development

1.6.1 Activity and efficiency limitations

One of the central challenges in catalyst design lies in achieving high catalytic activity under mild operating conditions, thereby minimizing external energy input. Thermo-catalytic processes such as CO_2 hydrogenation typically demand elevated temperatures and pressures to

overcome kinetic barriers and drive the reaction forward, which in turn leads to substantial energy consumption and operational costs. As a result, enhancing the intrinsic activity of catalysts is a key focus of ongoing research. Strategies to address this include nanoscale engineering to increase active surface area, controlled synthesis of specific crystal facets that favor desired reaction pathways, and electronic modifications via dopants or alloying to optimize adsorption energies of key intermediates. Collectively, these approaches aim to lower activation barriers, improve turnover frequencies, and enable more energy-efficient catalytic processes, which are essential for the sustainable deployment of CO_2 conversion technologies at scale[26].

1.6.2 Selectivity control

Table 1-2 The comparison of active metals and supports materials

Active metals		**Supports materials**			
Noble	**Non-noble**	**Metal oxides**	**Basic oxides**	**Clay**	**MOFs**
1. Ruthenium 2. Rhodium 3. Palladium 4. Platinum	1. Nickel 2. Cobalt 3. Molybdenum	1. TiO_2 2. Al_2O_3 3. SiO_2	1. CeO_2 2. Y_2O_3 3. MgO	1. Bentonite (montmorillonite) 2. Volkonskoite	1. Large surface area 2. Adsorption of CO_2 3. Tunable porous structure
1. Noble metals have an excellent ability to dissociate H_2 2. Ru, Rh has excellent activity and stability 3. High cost	1. Cheap, abundant 2. Ni shows good activity but deactivates easily 3. Co has higher resistance towards sintering	1. High surface area 2. Crates high dispersion of active phase on the surface of support	Basic nature, promoting CO_2 adsorption, which is slightly acidic	1. Abundance, low cost and naturally available 2. Provides adequate surface area 3. Naturally basic	**Structured Catalysts** Monolith, Structured Foam, Nanosheets, Fibrous Networks
Can be used to produce metallic, nitride, sulfide and carbide-based catalysts through different synthesis methods					1. Easier heat management and evacuation 2. Deliver high heat and mass transfer 3. Able to support high flow rates

Selective catalysis is critical for maximizing desired products and minimizing byproducts. However, controlling reaction pathways remains challenging, particularly in complex reactions like CO_2 hydrogenation or Fischer-Tropsch synthesis. Advanced strategies, such as noble/non-

noble catalysis, metallic/bimetallic/alloy catalysts, basic oxides catalysts and clay/MOFs support engineering, are being explored to improve selectivity (**Table 1-2**) [27].

1.6.3 Stability and deactivation issues

Catalyst deactivation, driven by sintering, poisoning, coking, and redox induced structural changes, remains a critical challenge in sustaining long term catalytic performance under industrial conditions. Metallic catalysts such as Ni, Co, and Cu are particularly susceptible to sintering at elevated temperatures, resulting in a progressive decline in active surface area. Additionally, exposure to impurities, including sulfur, chlorine, and carbonaceous deposits, leads to irreversible poisoning, further diminishing catalytic activity. The structural instability of catalysts under harsh operating environments exacerbates performance degradation, necessitating strategies to enhance thermal stability, mitigate poisoning effects, and improve regeneration capabilities[28]. Developing robust catalysts with tailored physicochemical properties is essential for ensuring prolonged catalytic lifetime and industrial viability.

1.6.4 Scalability and cost constraints

Many advanced catalysts rely on noble metals (Pt, Pd, Ru, Rh) or rare elements, which are expensive and have limited availability. Developing earth abundant, low-cost alternatives, such as transition metal catalysts (Fe, Co, Ni) or metal-free carbon-based catalysts, is a key challenge. Additionally, scaling up laboratory-developed catalysts to industrial-scale production while maintaining performance remains difficult[29].

1.6.5 Catalyst-support interactions

Catalyst performance is often influenced by the interaction between active sites and the support material. Optimizing metal-support interactions, porosity, and electronic properties are essential for designing high-efficiency catalysts[30]. Advanced characterization techniques, such as in situ spectroscopy and microscopy, help in understanding these interactions for better catalyst design.

1.6.6 Sustainable and green catalysis

Developing environmentally friendly catalysts that reduce energy consumption, avoid toxic materials, and enable circular chemistry is increasingly important. Challenges include eliminating the use of toxic solvents and harsh reaction conditions, designing recyclable catalysts to minimize waste, incorporating bio-inspired and enzymatic catalytic systems for sustainable chemistry[31].

1.7 Challenges in CO_2 hydrogenation

1.7.1 High energy demand and thermodynamic limitations

CO_2 is a highly stable molecule, making its activation thermodynamically and kinetically challenging. The hydrogenation of CO_2 typically requires: High temperatures (200-400°C) and pressures (10-50 bar) to drive the reaction forward. High H_2 consumption, which depends on the availability of green hydrogen from renewable sources[32]. These conditions lead to significant energy input requirements, making the process costly unless coupled with renewable energy sources or waste heat utilization.

1.7.2 Controlling selectivity in CO_2 hydrogenation

CO_2 hydrogenation offers a versatile pathway to produce a range of products, including methane (CH_4), methanol (CH_3OH), higher hydrocarbons (C_2+), and oxygenates such as ethanol and propanol. However, precise control over product selectivity remains a fundamental challenge, governed by catalyst composition, active site structure, and reaction conditions[33].

(1) Methanation vs. methanol formation

The selectivity between methanation and methanol synthesis is largely dictated by the nature of the active metal. Transition metals such as Ni and Ru preferentially facilitate CO_2 methanation via the Sabatier reaction, often leading to undesired CH_4 formation. In contrast, Cu-based catalysts favor methanol production, although their selectivity is highly sensitive to operating conditions and the presence of promoters or structural modifiers. Optimizing Cu-ZnO based systems with improved reducibility and adsorption properties is critical for enhancing methanol yield while minimizing side reactions.

(2) Challenges in Fischer-Tropsch synthesis (FTS)

Fe-based and Co-based catalysts enable the conversion of CO_2 into higher hydrocarbons through Fischer-Tropsch chemistry. However, product selectivity remains difficult to control due to a broad distribution of hydrocarbons and secondary reactions such as chain termination and over-hydrogenation, which suppress the formation of desired C_2+ products. Strategies to modulate chain growth probability, such as tuning catalyst reducibility, modifying support properties, and optimizing H_2/CO_2 ratios, are essential for improving selectivity toward long chain hydrocarbons.

(3) Alcohols vs. hydrocarbons

The selective formation of oxygenates, particularly ethanol, over hydrocarbons requires precise catalyst design. Alkali and transition metal promoters (e.g., K, Na, Mn) have been shown to enhance oxygenate selectivity by modifying electronic and adsorption properties.

However, excessive promoter loading can lead to catalyst deactivation or undesirable product shifts. Achieving a high ethanol to methanol ratio remains a challenge due to competing reaction pathways, necessitating the development of bifunctional catalysts that balance CO_2 activation, C-C coupling, and oxygenate stabilization.

Ultimately, optimizing selectivity in CO_2 hydrogenation requires a multifaceted approach, integrating rational catalyst design, promoter effects, and advanced reaction engineering. Fine-tuning these parameters will be key to unlocking efficient and scalable CO_2 into chemical processes.

1.7.3 Mass transfer and kinetic limitations

The reaction kinetics of CO_2 hydrogenation are governed by a complex interplay of mass transfer, adsorption/desorption dynamics, and the availability of active sites. Several key challenges must be addressed to enhance catalytic efficiency and product selectivity[34].

(1) H_2 and CO_2 adsorption competition

Effective CO_2 hydrogenation requires a delicate balance between CO_2 activation and sufficient H_2 adsorption to drive hydrogenation reactions. Catalysts must possess active sites capable of selectively activating CO_2 while preventing excessive H_2 adsorption that could lead to unwanted side reactions, such as methanation. Tailoring metal-support interactions and optimizing electronic properties can enhance selective CO_2 activation while maintaining efficient hydrogenation kinetics.

(2) Surface diffusion limitations

Mass transfer constraints within porous catalysts can hinder reactant and intermediate mobility, thereby limiting reaction rates. Restricted diffusion can lead to uneven active site utilization, particularly in microporous materials. Strategies such as nanoengineering, hierarchical porosity design, and optimized catalyst particle size can alleviate diffusion limitations, ensuring more efficient reactant accessibility and intermediate transport.

(3) Product inhibition and active site blocking

The accumulation of byproducts, particularly water and CO, can poison active sites, leading to performance degradation. Water promotes sintering or oxidation of metal sites, while CO strongly binds to catalytic surfaces, suppressing further CO_2 conversion. Engineering hydrophobic supports, introducing oxygen vacancies to mitigate CO poisoning, and employing dynamic reactor operation strategies (e.g., periodic regeneration or selective water removal) can help maintain catalyst stability over prolonged reaction cycles.

1.7.4 Reactor and process challenges

CO_2 hydrogenation can be conducted in various reactor configurations, such as fixed-bed, slurry-phase, and fluidized-bed reactors, each presenting challenges related to heat and mass transfer, catalyst deactivation, catalyst recovery, and high-pressure operation. Fixed-bed reactors suffer from heat and mass transfer limitations, while slurry-phase reactors face issues with catalyst separation and recovery. High-pressure operation, although necessary for higher conversion, increases costs and safety concerns. To overcome these limitations, integrating renewable H_2 sources, real-time catalyst regeneration, and hybrid catalytic approaches (e.g., thermo-electrocatalysis or plasma catalysis) offer promising solutions[35]. These innovations, coupled with advanced reactor designs and process intensification, are crucial to enhancing the efficiency, scalability, and sustainability of CO_2 hydrogenation processes, making them more viable for industrial applications.

1.7.5 Scale up and industrial feasibility

Although CO_2 hydrogenation holds great promise, its large-scale implementation faces significant barriers. One major challenge is the availability of hydrogen, as sustainable CO_2 hydrogenation relies on green hydrogen produced via water electrolysis, a process that remains costly. Furthermore, the technoeconomic feasibility of CO_2 hydrogenation is constrained by the need for further optimization of current catalysts and processes to compete with fossil fuel-based production methods. Additionally, the integration with carbon capture is another hurdle, as efficient gas separation technologies are required to capture and utilize CO_2 from industrial sources. Overcoming these challenges will necessitate innovations in low cost catalysts, process intensification, and carbon neutral hydrogen production, which are essential to make CO_2 hydrogenation commercially viable and sustainable in the long term[36].

1.8 Overview of the research work

1.8.1 The significance of the chosen topic

CO_2 is particularly in the context of global climate challenges and the urgent need for sustainable energy solutions. As atmospheric CO_2 levels continue to rise due to fossil fuel combustion, industrial activities, and land-use changes, innovative carbon utilization technologies have become critical to achieving carbon neutrality targets set for 2030-2060 by major economies worldwide.

CO_2 hydrogenation offers a promising pathway to convert a greenhouse gas into value-added chemicals and fuels, such as methanol, dimethyl ether (DME), and hydrocarbons. This

not only mitigates emissions but also closes the carbon loop, aligning with circular economy principles. Moreover, when coupled with green hydrogen derived from renewable energy sources, CO_2 hydrogenation becomes a cornerstone of power to value-added products strategies, transforming intermittent renewable energy into storable and transportable chemical energy.

From a research perspective, this field involves fundamental and applied challenges across catalysis, reaction engineering, materials science, and process integration. Enhancing selectivity, improving catalyst stability, understanding mechanistic pathways, and scaling up efficient reactor systems are active areas of investigation. As such, CO_2 hydrogenation serves as a multidisciplinary research platform with the potential to revolutionize sustainable chemical manufacturing and contribute meaningfully to the global decarbonization agenda.

1.8.2 Research ideas

For analyzing the fundamental cases of CO_2 hydrogenation, the challenges are focused on selectivity and conversion.

To address the ongoing challenges in CO_2 hydrogenation, particularly the trade-off between high conversion efficiency and product selectivity, this research focuses on unraveling the mechanistic pathways leading to the formation of value-added C_2+ products. Central to this investigation is the role of key surface-bound intermediates like methyl (CH_x) and methoxy/formyl (CH_xO) species, which are widely recognized as crucial precursors in the progression toward multi-carbon products. By systematically analyzing their reactivity and coupling behavior, three primary routes are proposed: CH_x-CH_x, CH_x-CH_xO, and CH_xO-CH_xO (methanol dehydration). These elementary reactions are hypothesized to govern the formation of diverse molecular architectures including saturated hydrocarbons (paraffins), unsaturated hydrocarbons (olefins), oxygenates (ethanol), and ethers (dimethyl ether).

Advanced characterization and kinetic modeling are employed to probe the energy profiles and surface dynamics of these intermediates under varying reaction conditions. This mechanistic insight enables a more granular understanding of the interplay between hydrogenation, C-O cleavage, and C-C bond formation steps. In particular, we explore how the balance of acidic and metallic functionalities on bifunctional catalysts can steer reaction selectivity by stabilizing desired intermediates and suppressing undesired side pathways, such as over-hydrogenation to methane or excessive CO formation via the reverse water-gas shift (RWGS) reaction.

Ultimately, this study aims to construct a comprehensive mechanistic framework that not only elucidates the fundamental steps of CO_2 activation and transformation but also informs the

rational design of next generation catalysts for selective C_2+ synthesis. The findings have significant implications for the development of sustainable CO_2 valorization technologies aligned with carbon neutrality goals.

1.8.3 Thermodynamic favorability

1.8.3.1 Reverse water gas shift (RWGS)

The reverse water gas shift (RWGS) reaction plays a pivotal role as the initial step in the CO_2 hydrogenation process, particularly in pathways targeting the production of CO derived fuels and chemicals. As a thermodynamically endothermic reaction, RWGS involves the conversion of CO_2 and H_2 into CO and H_2O. This transformation serves not only as a critical CO_2 activation route but also as a precursor to subsequent processes such as Fischer-Tropsch synthesis (FTS) and alcohol synthesis.

Therefore, understanding and optimizing the RWGS step is essential for enhancing the overall efficiency and selectivity of CO_2 hydrogenation systems. The activation of CO_2 is an inherently stable and linear molecule, which requires significant energy input and often proceeds via the formation of surface-bound intermediates, such as carbonates, bicarbonates, or formates. Catalysts with oxygen vacancies or reducible metal oxides (e.g., CeO_2, ZrO_2) are particularly effective in facilitating this activation. Concurrently, hydrogen activation on metallic sites such as Cu, Ni, or Co ensures the availability of dissociated hydrogen atoms necessary for the reduction of the activated CO_2 species. The balance between CO_2 activation and H_2 dissociation is crucial to drive the RWGS reaction forward under typical operating conditions (e.g., 500-700 K). From a mechanistic perspective, the RWGS step dictates the product selectivity of the entire CO_2 hydrogenation process. For example, the formation of CO via RWGS shifts the reaction pathway toward hydrocarbon production through FTS-type chain growth mechanisms. Conversely, bypassing RWGS in favor of direct hydrogenation of CO_2 may favor oxygenate products like methanol or DME, depending on the nature of the catalyst. Thus, tuning the RWGS pathway can strategically control the distribution of products.

In summary, the first step of the RWGS reaction is not merely a preparatory transformation, it is a thermodynamic and kinetic gatekeeper that determines the success and direction of CO_2 hydrogenation. Effective catalyst design must therefore focus on enhancing CO_2 adsorption, stabilizing intermediate species, and ensuring dynamic H_2 activation. Advancing our understanding of this fundamental step will be key to unlocking the potential of CO_2 as a feedstock for sustainable chemical production.

1.8.3.2 Fischer-Tropsch synthesis (FTS)

Once CO is formed via the RWGS reaction, it becomes a critical intermediate for Fischer-Tropsch synthesis (FTS), which converts syngas (CO + H_2) into long-chain hydrocarbons. FTS is a surface polymerization process catalyzed by transition metals such as Fe, Co, Ni or Ru. In the context of CO_2 hydrogenation, the in-situ generation of CO via RWGS enables a tandem reaction strategy, where the product distribution depends heavily on catalyst choice, reaction temperature, pressure, and H_2/CO ratio. Mechanistically, the process involves CO adsorption, dissociation into C* and O* on the catalyst surface, followed by sequential hydrogenation and C-C coupling steps. The rate-determining steps often include CO dissociation and the initial C-C bond formation. Cobalt based catalysts typically favor paraffin (alkane) production with high chain growth probability, while iron catalysts are more flexible and can generate both hydrocarbons and oxygenates, especially under CO_2 rich environments where secondary reactions (e.g., water-gas shift) remain active.

The challenge in applying FTS to CO_2 hydrogenation lies in managing the RWGS-FTS coupling efficiently. A key limitation is the potential accumulation of water from RWGS, which can oxidize active metal sites and inhibit hydrocarbon chain growth. Moreover, the thermodynamic competition between methanation and FTS must be controlled to avoid excessive CH_4 formation. Catalyst supports high water tolerance and promoters that regulate CO dissociation kinetics (e.g., K, Mn, or rare earth oxides) are vital in steering selectivity toward desired C_2+ products.

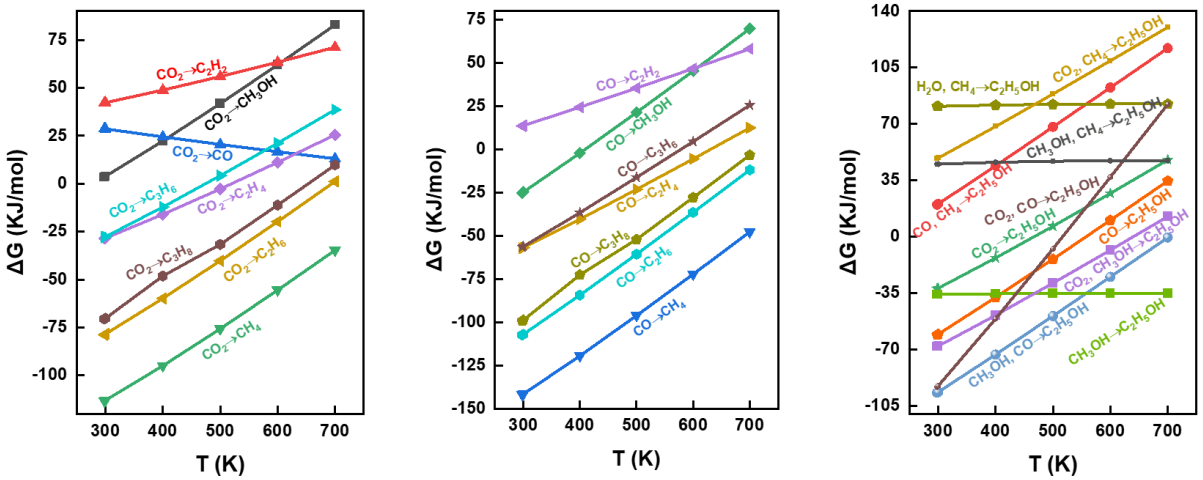

Figure 1-2. The calculation of Gibbs free energy for each reaction.

1.8.3.3 Alcohol synthesis following RWGS

Alternatively, the CO formed via RWGS can be directed toward alcohol synthesis, including methanol, ethanol, and higher oxygenates. This pathway typically utilizes Cu, Zn, or Zr based catalysts, which facilitate CO hydrogenation via associative mechanisms involving surface formyl (HCO*), hydroxy methylene (H_2CO*), and methoxy (CH_3O*) intermediates. Ethanol and higher alcohol formation generally requires C-C bond formation between intermediates like CH_x and CH_xO, which remains a fundamental challenge due to competing hydrogenation routes.

Cu based systems exhibit high methanol selectivity but are limited by poor C-C coupling capability. The introduction of Co or Ni into the Cu matrix enhances the formation of hydrocarbon fragments (CH_x), enabling coupling with oxygenates to form ethanol. ZrO_2, serving as a support or promoter, provides strong metal support interactions and oxygen vacancies, which improve CO_2/CO adsorption and intermediate stabilization. Furthermore, alkali doping (e.g., Na, K) has been reported to suppress over hydrogenation and promote C_2+ alcohols by altering electronic properties and modifying acid-base balance on the catalyst surface.

From a process design perspective, alcohol synthesis is often more compatible with lower-temperature conditions compared to FTS, reducing thermal stress on catalysts and allowing better control over product selectivity. However, maintaining high selectivity toward specific alcohols (e.g., ethanol) requires fine-tuning of reaction parameters and the active site ensemble capable of both oxygenate formation and selective C-C coupling[37].

1.8.4 Research contents

In this thesis, three series of catalysts were strategically synthesized and evaluated with the aim of promoting the selective hydrogenation of CO_2 toward distinct product classes, including saturated hydrocarbons (paraffins), unsaturated hydrocarbons (olefins), oxygenates (e.g., ethanol), and ethers, with a particular emphasis on dimethyl ether (DME). Each catalyst system was tailored to probe the structure, activity and selectivity relationships that govern the formation pathways of these target compounds under thermos-catalytic conditions.

The tandem reaction pathways of CO_2 hydrogenation whether proceeding via the reverse water-gas shift (RWGS) followed by Fischer-Tropsch synthesis (FTS), or through the formate-mediated route coupled with FTS are both thermodynamically feasible, as indicated by the standard Gibbs free energy changes associated with each step (**Figure 1-2**). These parallel mechanistic possibilities underscore the inherent complexity of CO_2 hydrogenation chemistry.

In this context, a critical challenge lies in steering reaction selectivity toward desired products, as multiple intermediates and competing pathways coexist. Tailoring catalyst composition, surface properties, and reaction conditions is therefore essential to selectively favor specific transformation routes and suppress undesired side reactions.

(1) Na-doped Co_3O_4 catalysts were engineered to modulate the electronic environment of active sites, thereby impeding both C-O and C-H bond cleavage processes. This modification resulted in a delayed onset of hydrocarbon formation at lower temperatures and induced a distinct selectivity shift, favoring the formation of paraffins and olefins through suppression of over-hydrogenation and enhanced stabilization of reaction intermediates.

(2) Trimetallic $CoCuZrO_x$ and Na-doped catalysts were rationally designed to enhance ethanol selectivity by leveraging the synergistic integration of CH_x and CH_xO intermediates. As for fcc-Co, CO* is easier to desorb to CO product, which has with a lower CO* desorption energy. Thus, it appears that there is less C-O bond cleavage compared with hcp-Co. Meanwhile, the Cu-Zr interface promotes methanol-related CH_xO intermediates. Sodium incorporation was found to inhibit the terminal hydrogenation step from CH_2 to CH_3, thereby favoring C-C coupling pathways and directing product distribution toward ethanol.

(3) CuZr-H-MCM-22 bifunctional catalyst was strategically developed to enable the one-step synthesis of dimethyl ether (DME) from CO_2 hydrogenation. The Cu-Zr component efficiently facilitates methanol formation through CO_2 activation and hydrogenation, while the integrated H-MCM-22 zeolite provides abundant Brønsted acid sites that promote rapid methanol dehydration. The intimate proximity of the redox and acidic functionalities ensures effective intermediate transfer, thereby enhancing DME selectivity and minimizing undesirable side reactions.

From the results, the formation and evolution of CH_x and CH_xO intermediates can be systematically described as arising from their random coupling with each other. However, product distribution obtained from fixed-bed reactors highlights a critical limitation that the intrinsic difficulty in steering these coupling pathways exclusively toward ethanol. This underscores why conventional approaches often fail to achieve high ethanol selectivity. By contrast, our mechanistic framework and analytical methodology provide a rational basis for identifying the plausible reaction channels that can, in principle, deliver nearly 100% selectivity to ethanol.

1.9 References

1 D. A. Lashof & D. R. Ahuja. Relative Contributions of Greenhouse Gas Emissions to Global Warming. *Nature*, 344 (1990) 529-531.

2 M. Reichstein, M. Bahn, P. Ciais *et al.* Climate extremes and the carbon cycle. *Nature*, 500 (2013) 287-295.

3 P. Friedlingstein, R. A. Houghton, G. Marland *et al.* Update on CO_2 emissions. *Nat. Geosci.*, 3 (2010) 811-812.

4 N. M. Dowell, P. S. Fennell, N. Shah & G. C. Maitland. The role of CO_2 capture and utilization in mitigating climate change. *Nat. Clim. Change*, 7 (2017) 243-249.

5 R. York. Do alternative energy sources displace fossil fuels? *Nat. Clim. Change*, 2 (2012) 441-443.

6 A. Rode, T. Carleton, M. Delgado *et al.* Estimating a social cost of carbon for global energy consumption. *Nature*, 598 (2021) 308-314.

7 S. Bilgen. Structure and environmental impact of global energy consumption. *Renewable Sustainable Energy Rev.*, 38 (2014) 890-902.

8 Y. Wang, R. Wang, K. Tanaka *et al.* Accelerating the energy transition towards photovoltaic and wind in China. *Nature*, 619 (2023) 761-767.

9 T. Lei, D. Wang, X. Yu *et al.* Global iron and steel plant CO_2 emissions and carbon-neutrality pathways. *Nature*, 622 (2023) 514-520.

10 J. Cheng, D. Tong, H. Y. Zhao *et al.* Trade risks to energy security in net-zero emissions energy scenarios. *Nat. Clim. Change*, 15 (2025) 505-513.

11 H. Z. Pan, J. Page, R. Shi *et al.* Contribution of prioritized urban nature-based solutions allocation to carbon neutrality. *Nat. Clim. Change*, 13 (2023) 862-870.

12 R. E. Zeebe, A. Ridgwell & J. C. Zachos. Anthropogenic carbon release rate unprecedented during the past 66 million years. *Nat. Geosci.*, 9 (2016) 325-329.

13 B. Bruckner, K. Hubacek, Y. L. Shan, H. L. Zhong & K. S. Feng. Impacts of poverty alleviation on national and global carbon emissions. *Nat. Sustain.*, 5 (2022) 311-320.

14 M. Steinacher, F. Joos & T. F. Stocker. Allowable carbon emissions lowered by multiple climate targets. *Nature*, 499 (2013) 197-201.

15 M. Hulme, E. M. Barrow, N. W. Arnell *et al.* Relativeimpactsof humaninduced climate change and natural climatevariability. *Nature*, 397 (1999) 688–691.

16 J. Ye, N. Dimitratos, L. M. Rossi *et al.* Hydrogenation of CO_2 for sustainable fuel and chemical production. *Science*, 387 (2025) eadn9388.

17 D. Ravikumar, D. Zhang, G. Keoleian *et al.* Carbon dioxide utilization in concrete curing or mixing might not produce a net climate benefit. *Nat. Commun.*, 12 (2021) 855.

18 L. C. Burrows, F. Haeri, P. Cvetic *et al.* A Literature Review of CO_2, Natural Gas, and Water-Based Fluids for Enhanced Oil Recovery in Unconventional Reservoirs. *Energy Fuels*, 34 (2020) 5331-5380.

19 C. M. Duarte, A. Bruhn & D. Krause-Jensen. A seaweed aquaculture imperative to meet global sustainability targets. *Nat. Sustain.*, 5 (2022) 185-193.

20 Q. Ou, M. Zhu, Z. Yang & Y. F. Han. Pathway regulation of carbon dioxide hydrogenation on iron-based-zeolite bifunctional catalysts. *Appl. Catal., B*, 357 (2024) 124211.

21 V. Scott, S. Gilfillan, N. Markusson, H. Chalmers & R. S. Haszeldine. Last chance for carbon capture and storage. *Nat. Clim. Change*, 3 (2012) 105-111.

22 S. Sgouridis, M. Carbajales-Dale, D. Csala, M. Chiesa & U. Bardi. Comparative net energy analysis of renewable electricity and carbon capture and storage. *Nat. Energy*, 4 (2019) 456-465.

23 I. Sullivan, A. Goryachev, I. A. Digdaya *et al.* Coupling electrochemical CO_2 conversion with CO_2 capture. *Nat. Catal.*, 4 (2021) 952-958.

24 B. Shan, S. Vanka, T. T. Li *et al.* Binary molecular-semiconductor p-n junctions for photoelectrocatalytic CO_2 reduction. *Nat. Energy*, 4 (2019) 290-299.

25 H. S. Shafaat & J. Y. Yang. Uniting biological and chemical strategies for selective CO_2 reduction. *Nat. Catal.*, 4 (2021) 928-933.

26 S. Navarro-Jaen, M. Virginie, J. Bonin *et al.* Highlights and challenges in the selective reduction of carbon dioxide to methanol. *Nat. Rev. Chem.*, 5 (2021) 564-579.

27 X. Wang, H. Shi & J. Szanyi. Controlling selectivities in CO_2 reduction through mechanistic understanding. *Nat. Commun.*, 8 (2017) 513.

28 A. J. Martín, S. Mitchell, C. Mondelli, S. Jaydev & J. Pérez-Ramírez. Unifying views on catalyst deactivation. *Nat. Catal.*, 5 (2022) 854-866.

29 C. Hepburn, E. Adlen, J. Beddington *et al.* The technological and economic prospects for CO_2 utilization and removal. *Nature*, 575 (2019) 87-97.

30 A. Parastaev, V. Muravev, E. H. Osta *et al.* Boosting CO_2 hydrogenation via size-dependent metal-support interactions in cobalt/ceria-based catalysts. *Nat. Catal.*, 3 (2020) 526-533.

31 Q. W. Song, Z. H. Zhou & L. N. He. Efficient, selective and sustainable catalysis of carbon dioxide. *Green Chem.*, 19 (2017) 3707-3728.

32 P. Nugent, Y. Belmabkhout, S. D. Burd *et al.* Porous materials with optimal adsorption thermodynamics and kinetics for CO_2 separation. *Nature*, 495 (2013) 80-84.

33 R. Ye, J. Ding, T. R. Reina *et al.* Design of catalysts for selective CO_2 hydrogenation. *Nat. Synth.*, 4 (2025) 288-302.

34 R. P. Ye, J. Ding, W. Gong *et al.* CO_2 hydrogenation to high-value products via heterogeneous catalysis. *Nat. Commun.*, 10 (2019) 5698.

35 M. S. Frei, C. Mondelli, R. Garcia-Muelas *et al.* Atomic-scale engineering of indium oxide promotion by palladium for methanol production via CO_2 hydrogenation. *Nat. Commun.*, 10 (2019) 3377.

36 T. Moore, A. A. Wong, B. Giera *et al.* Accelerating climate technologies through the science of scale-up. *Nat. Chem. Eng.*, 1 (2024) 731-740.

37 W. M. Haynes, D. R. Lide & T. J. Bruno. *CRC Handbook of Chemistry and Physics*. (2014).

Chapter 2

Tuning sodium mass ratio in cobalt oxide catalysts to modulate paraffin and olefin selectivity in CO_2 hydrogenation

Optimizing catalytic systems for CO_2 hydrogenation is crucial for directing product selectivity toward paraffins and olefins. Here, we investigate the role of sodium as a dopant in metallic cobalt catalysts, elucidating its impact on structural and electronic properties of metallic Co and CoO_x. It has been demonstrated that by tuning the hydrogenation capability of CH_x intermediates to enhance CH_2 amounts and improve the distribution of C_2+ products, sodium incorporation alters catalyst reducibility and active site distribution, thereby modulating selectivity. Kinetic studies have demonstrated that sodium exerts a significant influence on the electronic environment and active site accessibility, resulting in alterations in product distribution. The findings presented herein offer fundamental insights into sodium-modulated cobalt catalysts and inform the design of tailored catalytic systems for efficient CO_2 conversion.

2.1. Introduction

The pressing necessity to address climate change has prompted the development of effective CO_2 utilization technologies that convert emissions into valuable chemicals and fuel[1-5]. CO_2 hydrogenation has been identified as a potentially viable catalytic process for the production of hydrocarbons, enabling the integration of renewable hydrogen into the carbon cycle as evidenced by numerous studies[6-9]. However, achieving high selectivity towards specific products (e.g., paraffins vs. olefins) remains a significant challenge, governed by the complex interplay of CO_2 activation, C-O cleavage, and C-C coupling. The electronic and structural properties of catalysts have been shown to exert a significant influence on product distribution, thereby underscoring the necessity for rational design to regulate reaction pathways. Cobalt-based catalysts, most notably Co_3O_4, have been shown to exhibit high stability and tunable activity, however, they demonstrate a high degree of selectivity that is highly sensitive to electronic modifications. While alkali metals are recognised for their role as structural and electronic promoters, capable of altering charge transfer, adsorption energetics, and intermediate stability[10-14], as demonstrated by the enhanced light olefin production on Fe catalysts facilitated by potassium, and the alkane selectivity exhibited in alkali-doped CoRu/γ-Al_2O_3[15]. The atomic-scale impact of sodium doping on cobalt catalysts remains underexplored. Specifically, its role in modulating active site distribution, electronic structure, and kinetic pathways requires further elucidation.

The formation of C_1 and C_2+ products follows distinct mechanistic routes, dictated by the nature of the active sites. Metallic Co sites exhibit a strong propensity for H_2 activation and C-O bond dissociation, promoting the RWGS and direct C-O scission pathways, leading primarily to methane and CO production. In contrast, oxygen vacancies and $Co^{\delta+}$ sites, formed through Na incorporation, exhibit lower H_2 dissociation capability but stronger CO_2 adsorption, favoring the formate pathway, which facilitates C_2+ paraffins production. It can thus be concluded that the modulation of active sites through Na incorporation is therefore a key determinant in controlling the selectivity between C_1 and C_2+ hydrocarbons.

With regard to the process of CO_2 hydrogenation to C_1 products, it is evident that two discrete mechanistic pathways are observed, each exhibiting a distinct influence on product selectivity and energy efficiency (**Figure 2-1**). The reverse water gas shift (RWGS) pathway involves the initial hydrogenation of CO_2 to form the HOCO intermediate, which undergoes C-O bond cleavage to generate CO. The CO may either desorb as a final product or undergo further hydrogenation, forming CH_xO intermediates that eventually yield methane (CH_4) through stepwise C-O bond cleavage and hydrogenation[18-21]. In the formate pathway, CO_2 first

undergoes hydrogenation to form a formate intermediate (HCOO), which subsequently undergoes C-H bond formation and C-O cleavage, leading to CH_xO species. These intermediates can undergo further hydrogenation to yield methanol, or alternatively, undergo C-O bond scission, resulting in the generation of CH_x species that subsequently form methane. The selectivity between paraffins and oxygenates is determined by the competition between C-O cleavage and CH_xO hydrogenation[22-26].

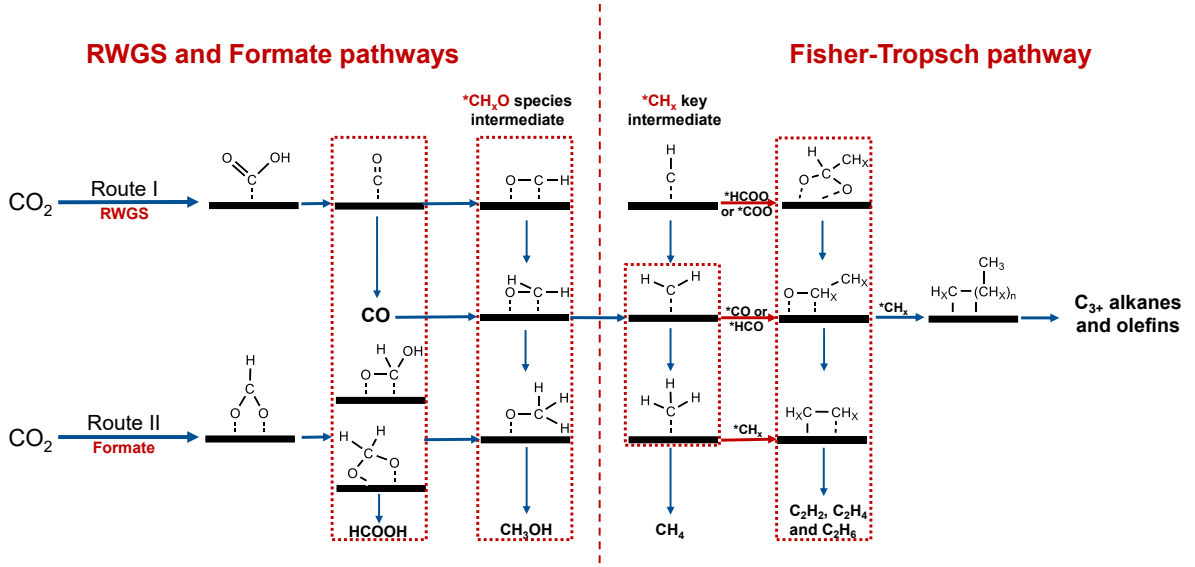

Figure 2-1. Catalytic mechanism of C_2+ paraffins and olefins synthesis

Among these pathways, the RWGS and formate mechanisms proceed through hydrogenation steps, forming more stable intermediates that facilitate subsequent reactions. It is imperative to comprehend these mechanistic routes in order to optimize CO_2 hydrogenation catalysts, given that the predominant pathway exerts a substantial influence on product distribution and overall catalytic efficiency. The formation of C_2+ hydrocarbons and oxygenates follows a distinct mechanism in which CH_x species, originating from CO, formate (HCOO), or methanol dehydroxylation, serve as key intermediates for C-C bond formation via insertion. It has been established that repeated coupling and hydrogenation steps extend the carbon chain, yielding C_2+ hydrocarbons. Notably, the regulation of H_2 and CO_2 activation exerts a direct influence on the C/H ratio of intermediates, thereby controlling product selectivity[27,28].

The principal contribution of this study is the determination of the disparate hydrogenation capabilities of Co^0 and $Co^{\delta+}$ and noticed the existence of $Co^{\delta+}$ after reduction of Na-CoO_x catalyst. In this study, the impact of sodium doping on Co_3O_4 catalysts is investigated, with the aim of elucidating its effect on CO_2 hydrogenation selectivity. The integration of in situ spectroscopy, surface characterization techniques, and kinetic analyses enables a systematic

examination of the manner in which sodium alters the electronic and structural properties of cobalt catalysts, thereby increasing the apparent activation energy for CH_2 to CH_3 conversion and regulating products distribution. The results of this study demonstrate that sodium doping has the capacity to modify the active site environment, thereby influencing the equilibrium between CO_2 activation and hydrocarbon chain growth, ultimately steering selectivity toward paraffins or olefins. The insights provided in this study offer a comprehensive understanding of alkali-metal-modulated catalysis and establish guiding principles for the design of next-generation catalysts with programmable hydrocarbon selectivity, advancing CO_2 hydrogenation as a scalable and sustainable route for carbon-neutral chemical synthesis.

2.2 Methods

2.2.1 Chemicals and materials

Cobalt nitrate ($Co(NO_3)_2 \cdot 6H_2O$), 1,8-Diazabicyclo[5.4.0]undec-7-ene (DBU), NaOH were purchased from Sigma-Aldrich and used without further purification. Deionized (DI) water (18.2 $M\Omega \cdot cm^{-1}$) was used to prepare all aqueous solutions.

2.2.2 Sample preparation

2.2.2.1 Precipitation method to synthesis Co_3O_4 and impregnation method to synthesis Na-CoO_x

The Co_3O_4 catalysts were synthesized via a precipitation method, followed by a controlled thermal treatment to achieve optimal dispersion of Co_3O_4. Firstly, 1 mol/L aqueous solutions of cobalt nitrate ($Co(NO_3)_2 \cdot 6H_2O$) are prepared for the subsequent precipitation process. The DBU bio-based solution was added dropwise into the cobalt solution under vigorous stirring, with the pH maintained at 10. This precipitation process led to the formation of Co hydroxide precursors, which were then aged at room temperature for a duration of 12 hours. The resulting precipitate was filtered, washed with deionized water until almost neutral, and dried at 60°C overnight. The dried samples were subsequently calcined at a temperature of 400°C for a duration of 5 hours in air to convert the hydroxides to metal oxides (Co_3O_4). In conclusion, the 0.1 mol/L sodium hydroxide solution and the calcined Co_3O_4 catalyst were amalgamated in varying 0.15wt%, 0.3wt%, 0.75wt%, 1.50wt% and 2.00wt% Na mass ratios and the resultant sample was then desiccated using a rotary evaporator at 60 °C. The precursor was subsequently calcined at a temperature of 400°C for a duration of 5 h in an air atmosphere to convert the sodium hydroxide to sodium composite to generate the desired catalyst with partially Na composite within a mixture of metals oxide (Na-CoO_x).

2.2.3 Catalyst testing

The catalytic performance of all catalysts was evaluated within a high-pressure, continuous-flow, fixed-bed reactor. A mixture 10-120 mg of cobalt-based catalysts (250-300цm) with 600 mg of SiC (150-250 цm) was prepared and subjected to a pretreatment process in an $2H_2/N_2$ atmosphere at 310 °C with a flow rate of 50 mL·min^{-1} for a duration of 0.5 h. The temperature was then reduced to 300 °C, and $CO_2/H_2/N_2$ (24/72/4, 3 MPa) was introduced with a flow rate of 50 mL·min^{-1}. Subsequent to the stabilization of pressure and temperature, the gas flow was maintained at 50 mL·min^{-1} and an Agilent chromatograph equipped with a flame ionization detector and a tuning Methanizer, was utilized for the online analysis of products. The catalytic performance of the catalysts was evaluated in terms of CO_2 conversion, product selectivity and space-time yield (STY) of products.

2.2.4 The computational formulas were as follows:

CO_2 conversion, C_{CO2} (%) = $(X_{CO2,\,in} - X_{CO2,\,out})/X_{CO2,\,in} \times 100\%$

Product selectivity, Sel% = $X_{product}/(X_{CO2,\,in} - X_{CO2,\,out}) \times 100\%$

STY of paraffin, $STY_{paraffin/olefin}(mmol \cdot g_{cat}^{-1} \cdot h^{-1}) = (F_{CO2,\,in} \times C_{CO2} \times Sel_{paraffin/olefin})/W_{cat}$, where $X_{CO2,\,in}$ and $X_{CO2,\,out}$ are the mole fractions of CO_2 in pristine and exit mixed gas, respectively; $F_{CO2,\,in}$ (mol·h^{-1}) is the molar flow rate of CO_2 in pristine mixed gas; $STY_{paraffin/olefin}$ is the space time yield of paraffin/olefin; $Sel_{paraffin/olefin}$ is the selectivity of paraffin/olefin; W_{cat} (g) is the weight of catalyst.

Space velocity $(L \cdot g_{cat}^{-1} \cdot h^{-1}) = (V_{flow}/W_{cat}) * 0.06$

Space time (s) = $(V_{cat}/V_{flow}) * 60$, where V_{flow} (mL/min) is the total flow rate of the pristine mixed gas; W_{cat} (g) is the weight of catalyst; V_{cat} (mL) is the volume of catalyst

2.3 Characterizations

2.3.1 In-situ XRD

The crystalline structure of the catalyst was determined using powder X-ray diffraction. The X-ray diffraction patterns were collected using a Panalytical Empyrean System diffractometer with Cu Kα radiation (λ = 0.1542 nm), operating at 45 kV/40 mA, using a nickel K_β filter and a solid-state detector.

2.3.2 H_2 TPR

The H_2 temperature-programmed reduction (TPR) was conducted utilizing a Chemstar instrument manufactured by Quantachrome instruments company. Prior to TPR measurement,

100 mg of the catalyst was flushed with Ar (>99.999%) at 150 °C for a duration of 1 h then cooled to 50 °C. Subsequently, the temperature was increased from 50 to 500 °C at a rate of 2 °C·min^{-1} under H_2/Ar (volume ratio 1/9, flow rate 30 mL·min^{-1}). The temperature was then maintained at 500 °C for a period of 30 min. The H_2 concentration was monitored by means of a thermal conductivity detector (TCD). The H_2-TPR profile was recorded as H_2 consumption versus reduction temperature.

2.3.3 H_2 TPD

The process of H_2 chemisorption on reduced catalysts was carried out using the same instrument of H_2-TPR, namely the Chemstar instrument from Quantachrome instruments company, which is utilized for H_2-TPD. A 0.10 g portion of the Co-based sample was subjected to reduction at a temperature of 310 °C for a duration of 1 h in H_2 flow (>99.999%, 30 mL·min^{-1}) and then cooled to 100 °C. Subsequently, the same H_2 flow was maintained at 100 °C for a further hour, with the objective of saturating the surface-active sites. Afterward, Ar was introduced instead of H_2 (>99.999%, 10 mL·min^{-1}) for a duration of 30 min, with the objective of eradicating physiosorbed H_2. Subsequently, the temperature was elevated from 100 to 450 °C at a rate of 10 °C·min^{-1} and maintained at 450 °C for a duration of 2 h under Ar flow. The desorbed H_2 was monitored by TCD and used for quantification.

2.3.4 BET

Adsorption measurements with N_2 (99.999 vol%) at 77 K were carried out on a NOVAtouch system from H. A. Shah Group company, which uses a volumetric method to determine the adsorbed amount under equilibrated gas pressure. The processing of adsorption data was conducted utilizing the TouchWin Software Version 1.21. Samples were transferred into pre-weighed sample tubes and capped with glass sticks. Samples were subsequently activated at 583 K for 0.5 h under hydrogen atmosphere of 1bar to ensure the absence of unwanted adsorbates and identical premeasurement states of all samples. In particular, this unusually activated temperature and time were chosen for all samples to ensure the same in the fixed bed reactor which is used to activate the catalyst under the same condition. The mass of the adsorbents was then recorded, with the result generally around 100 mg of each catalyst. A liquid nitrogen bath was used for measurements at 77 K. The apparent surface area was derived using the Brunauer-Emmett-Teller (BET) model and is hence given as the "BET area" based on N_2 isotherms measured at 77K. To determine this value for microporous materials, care was taken to adhere to the Rouquerol criteria. The pore size distribution was derived by fitting N_2 isotherms measured at 77 K with sets of theoretical isotherms (kernel) derived from two-

dimensional non-local density functional theory (2D-NLDFT) based methods for specific pore sizes and geometry. The fitting process was executed utilising the designated kernel, which was accessible via the TouchWin Software Version 1.21.

2.3.5 Atomic absorption spectroscopy

The elemental composition of the samples was determined by atomic absorption spectroscopy in a Unicam M Series Flame-AAS apparatus that was equipped with an FS 95 autosampler and a GF 95 graphite furnace.

2.3.6 SEM measurements

The morphology of the samples was measured with a scanning electron microscope (Carl Zeiss SMT NVision 40) equipped with a field emission cathode (FESEM) at an acceleration voltage of 5 kV.

2.3.7 In-situ DRIFTS

In situ FTIR spectra were collected on a Thermofisher Scientific 4700 FTIR spectrometer equipped with a DRIFTS accessory and a high temperature cell (Harrick). Each spectrum was recorded at a resolution of 4 cm^{-1}, with the average of 64 scans, and reported as pseudo-absorbance. The Co_3O_4 and 0.75wt% Na-CoO_x powders were meticulously placed into the sample holder cup of the high-temperature cell with 1:10 SiO_2 dilution. Prior to the acquisition of spectra at 523 Kelvin, the catalyst sample underwent a reduction in hydrogen at 583 Kelvin for a duration of one hour. Thereafter, the sample was subjected to a cooling process in a hydrogen flow, accompanied by a continuous purging of hydrogen at room temperature for a designated period. Subsequently, an infrared spectrum was recorded at the reaction temperature of 523 Kelvin in hydrogen, with a flow rate of 20 $mL \cdot min^{-1}$ and a pressure of 20 bar. A gas feeding manifold, equipped with electronic mass flow controllers manufactured by Brooks, was utilized to introduce gases with controlled flow rates and compositions. For the transient experiments, gases (25% CO_2, 75% H_2) with a flow rate of 20 $mL \cdot min^{-1}$ were introduced into the cell and switched when necessary. The acquisition of DRIFTS spectra was conducted at an interval of approximately 180 seconds.

2.3.8 XPS

The X-ray photoelectron spectroscopy data were collected using an AXIS Supra$^+$ X-ray photoelectron spectrometer from SHIMADZU company.

2.4 Results and discussion

2.4.1 The activity and selectivity of metallic cobalt

In order to enhance C_2+ hydrocarbon selectivity, Co_3O_4 catalysts with systematically varied Na loadings were synthesized to modulate surface hydrogenation kinetics and suppress excessive C-H bond formation that favors methane. Preparation of both pristine and Na-modified Co_3O_4 catalysts was undertaken via a precipitation method, followed by incipient wetness impregnation (IWI) using a NaOH solution to introduce sodium species with controlled dispersion. The unmodified Co_3O_4 catalyst demonstrated high methane selectivity (approximately 90%), indicative of rapid hydrogenation of CO* intermediates but limited chain propagation toward C_2+ hydrocarbons (**Figure 2-2**).

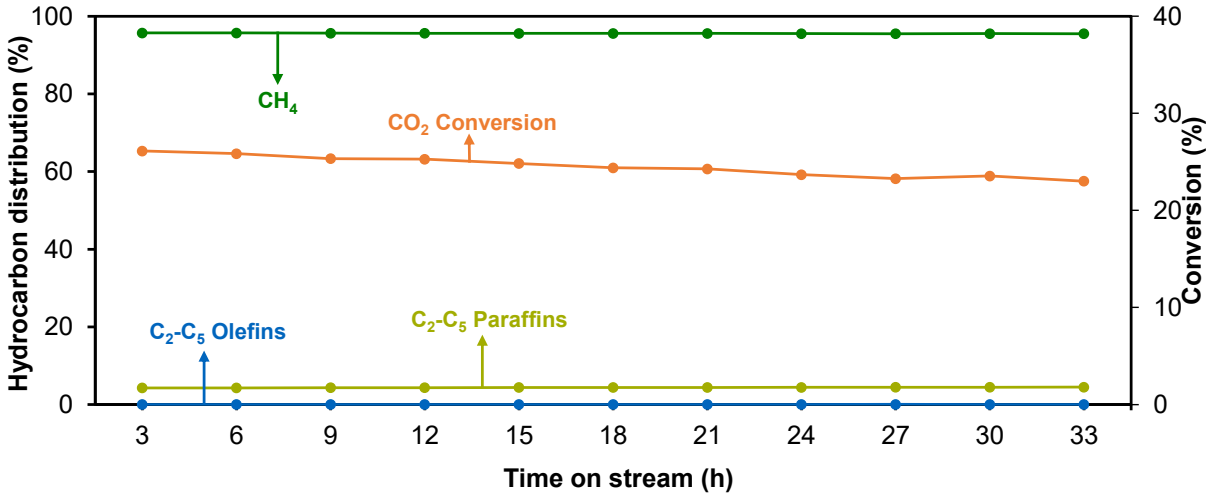

Figure 2-2. The stability of catalytic yield and selectivity of the products (methane, C_2-C_5 olefins and paraffins HCs) of metallic cobalt. All the experiments are regarded as CO free and analyzed at 300°C, 3.0 MPa, space velocity = 150 $L \cdot g_{cat}^{-1} \cdot h^{-1}$, $H_2/CO_2 = 3$.

Conversely, the incorporation of Na was anticipated to effect modifications to the electronic structure and basicity of the Co surface, thereby weakening H_2 adsorption and impeding terminal hydrogenation, thereby promoting C-C coupling and improving higher hydrocarbon selectivity.

2.4.2 Effect of Na loading on the activity and selectivity of CoO_x

To investigate the influence of Na on the CoO_x system, catalysts with varying sodium mass ratios were synthesized and their performance systematically compared. The systematic evaluation of 0-2 wt% Na-CoO_x catalysts under identical reaction conditions was conducted to ascertain the synergistic interaction between Na and CoO_x, which promotes C-C coupling while inhibiting methane formation (**Figure 2-3**). The incorporation of Na alkali metal has been

demonstrated to exert a substantial influence on the hydrogenation of CO_2 to C_2+ paraffins and olefins over Co-based catalysts[17]. The 0.75 wt% Na-CoO_x catalyst exhibited the highest C_2+ space time yield (STY), with C_2+ paraffins reaching 13.5 $\mathrm{mmol \cdot g_{cat}^{-1} \cdot h^{-1}}$ and C_2+ olefins reaching 7.8 $\mathrm{mmol \cdot g_{cat}^{-1} \cdot h^{-1}}$. Furthermore, the 0.75 wt% Na-CoO_x catalyst demonstrated a CO_2 conversion of 8.6 % and a C_2+ selectivity of 41.4% with CO free, whereas the unmodified Co catalyst predominantly facilitated methane production with negligible 4.5% C_2+ hydrocarbon formation. The volcano-like trend observed with increasing Na loading suggests an optimal balance between CO_2 activation and chain propagation, beyond which excessive Na incorporation may suppress active Co sites and hinder C_2+ formation. The catalytic activity of catalysts for CO_2 hydrogenation was evaluated under controlled reaction conditions to assess its intrinsic performance. During the reaction, CO_2 conversion was maintained below equilibrium concentrations of alkanes and olefins to ensure that intrinsic activity measurements could be taken. The precise sodium content was analyzed using atomic absorption spectroscopy (AAS), with the precise loading being of paramount importance (**Table S2-1**).

It is evident that incorporation of sodium at moderate levels gives rise to discernible alterations in the surface morphology. As demonstrated in **Figure 2-3 D, E and S2-9**, scanning electron microscopy (SEM) images reveal an enhancement in particle coalescence and a modest degree of agglomeration, which can be ascribed to the interaction between sodium species and metal oxides.

The formation of sodium modified domains has the potential to influence catalytic behavior by altering active site exposure and modifying electronic properties. At elevated sodium concentrations, the catalyst surface manifests significant aggregation and the presence of larger crystallites. SEM micrographs reveal the formation of distinct sodium-rich clusters, which could lead to pore blockage and a reduction in the number of exposed active sites, thus, the volcano shape of the products distribution in (**Figure 2-3**). Additionally, an increase in surface roughness is observed, which has the potential to affect mass transfer during catalysis. These structural modifications at elevated sodium levels have the potential to contribute to catalyst deactivation, a process that is characterized by the hindrance of reactant accessibility and the promotion of undesired side reactions. The BET result provides further evidence in support of the aggregation with the Na doped, which exhibits a significantly reduced surface area after loading Na (**Figure S2-10** and **Table S2-3**). The result of H_2 chemisorption and AAS demonstrate that cobalt dispersion is also obtained (**Table S2-4**), which is consistent with the shift in reactivity.

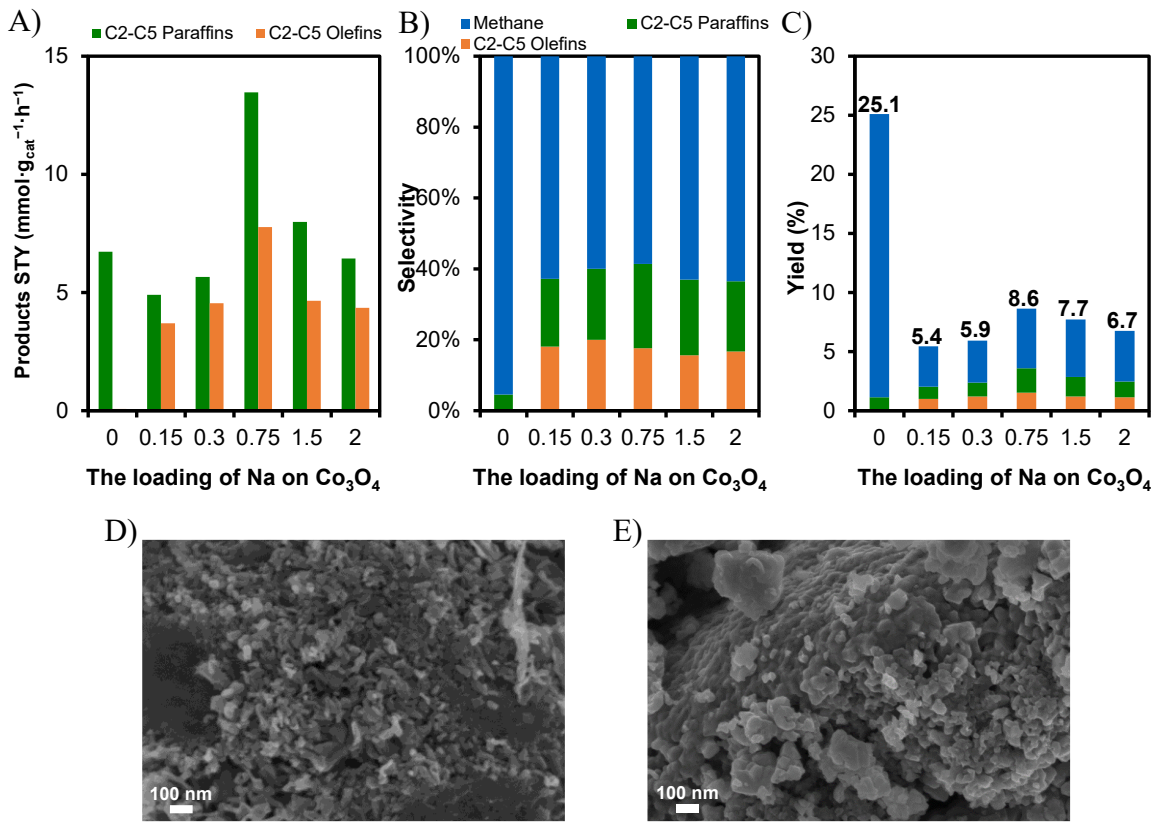

Figure 2-3. (**A**) C_2-C_5 olefins and paraffins HCs space time yield (STY) for adjusted Na loading. (**B**) Catalytic performance on x wt% Na-CoO_x. (**C**) Catalytic yield for x wt% Na-CoO_x. (**D**) SEM image of Co_3O_4 (**E**) SEM image of 0.75 wt% Na-CoO_x. All the experiments are regarded as CO free and analyzed at 300°C, 3.0 MPa, space velocity = 150 L·g_{cat}^{-1}·h^{-1}, H_2/CO_2 = 3.

2.4.3 Kinetic analysis for promoting C_2+ STY by alkali promoters

The reaction order can be utilized to identify the change of rate-determined step and to ascertain the influence on the selectivity of C_2+ products. From the results of **Figure 2-4, 2-5**, the presence of an alkali promoter increases the STY of C_2+ by influencing the kinetic reaction order and apparent activation energy. Kinetic analyses further support the mechanistic distinctions between Na-CoO_x and metallic Co catalysts. The apparent reaction orders for H_2 (α) and CO_2 (β) were α = 1.42 and β = 0.89, respectively, for metallic Co (**Figure 2-4**), whereas for 0.75 wt% Na-CoO_x, α = 0.91 and β = 0.40, indicating a less efficient C-C coupling pathway over metallic Co. The presence of sodium in the form of Na-doped has been shown to enhance the ability of catalysts to adsorb and activate both CO_2 and H_2, thereby reducing the dependence of the reaction rate on reactant concentration and lowering the apparent reaction order. The present study suggests that the suppression of CO_2 and H_2 activation through the promotion of Na benefits C_2+ formation while impeding CH_2 to CH_3 conversion and reducing CH_4 selectivity,

which leads to a change in the rate-determined step. The CO_2/H_2 ratio exerts a further modulatory effect on product distribution, with increasing CO_2 concentration leading to a reversed volcano shaped on C_2+ space time yield (STY).

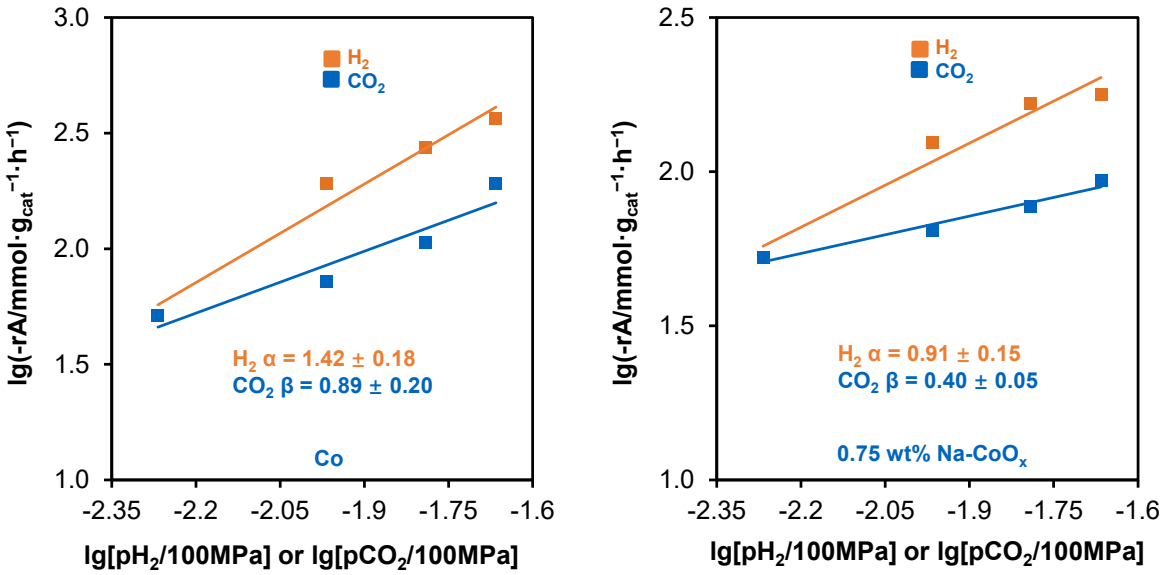

Figure 2-4. (**Left**) CO_2 and H_2 overall reaction orders for metallic cobalt. (**Right**) CO_2 and H_2 overall reaction orders for 0.75 wt% Na-CoO_x. All the experiments are analyzed at 300°C, 3.0 MPa, space velocity = 150 $L \cdot g_{cat}^{-1} \cdot h^{-1}$, H_2/CO_2 = 1/4-4/1. A: the total conversion of CO_2.

A comparison of the metallic cobalt and Na-CoO_x catalysts was conducted, with the results indicating the highest C_2+ selectivity at approximately 9.2% to 40.8%, while CO_2 conversion changes from 5.9% to 15.0% separately with the adjustment of CO_2/H_2 ratio from 1:4 to 4:1 (**Figure S2-1, S2-2 and S2-4, S2-5**). The Na-CoO_x catalyst reveals that suppressing excessive CO_2 and H_2 activation facilitates chain growth, whereas a CO_2/H_2 ratio of 1:1 yields the lowest C_2+ selectivity, likely due to competitive adsorption or unfavorable surface reaction dynamics. The high reaction rate observed over metallic cobalt is strongly dependent on the reactant concentration, suggesting that the adsorption and activation of CO_2 and H_2 constitute the primary kinetic bottlenecks. The observed shift for the Na-CoO_x catalyst suggests a mechanistic transition in which the activation modes of CO_2 and H_2 are fundamentally modified. This alteration likely mitigates the kinetic constraints of the original rate determining step, lowering its energy barrier and redirecting the reaction toward an olefin selective pathway.

Concurrently, the reduction in apparent activation energy for targeting products is a further incentive to encourage the C_2+ hydrocarbon formation. It is evident that the composite catalyst

Na-CoO_x displays a considerably lower apparent activation energy for the formation of C_2+ paraffins (101 kJ/mol) and C_2+ olefins (105 kJ/mol) in comparison to pure metallic Co for C_2+ paraffins (129 kJ/mol) and C_2+ olefins (117 kJ/mol) (**Figure 2-5**), and a similar trend for apparent activation energy for methane production. In consideration of the outcomes pertaining to selectivity and Co dispersion (**Table S2-4**), it is postulated that the structure or electron property of the Na-CoO_x catalyst enhances the efficiency with which C_2+ is produced, indicating an enhancement in the catalytic performance with regard to C_2+ formation.

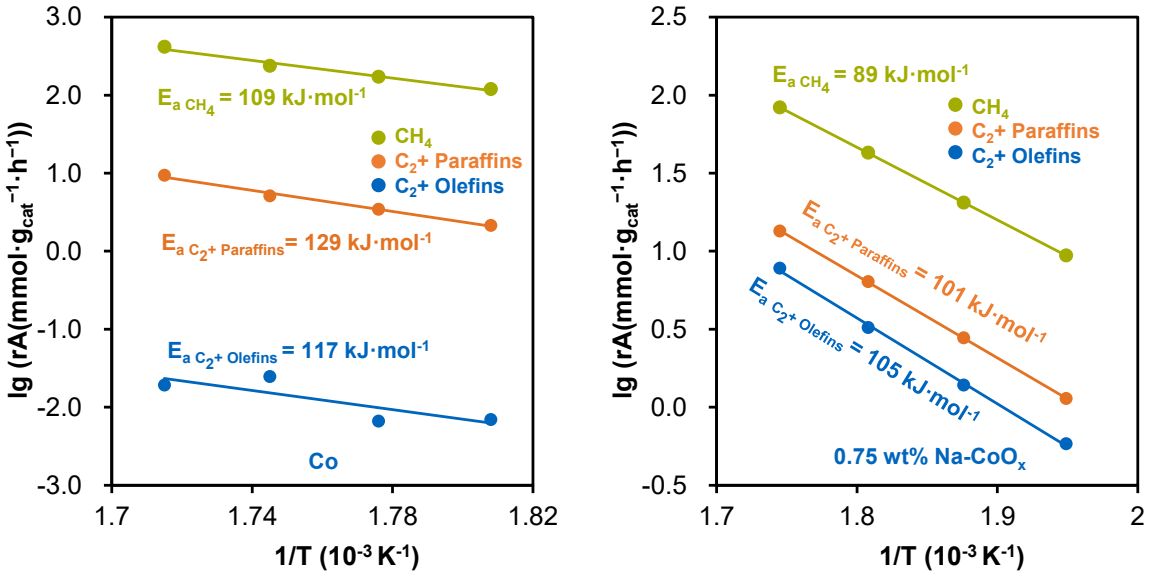

Figure 2-5. (**Left**) Apparent activation energies for overall CH_4, C_2+ paraffins and C_2+ olefins formation on metallic cobalt. (**Right**) Apparent activation energies for overall CH_4, C_2+ paraffins and C_2+ olefins formation on 0.75 wt% Na-CoO_x. All the experiments are analyzed at 240-300°C, 3.0 MPa, space velocity = 150 $L \cdot g_{cat}^{-1} \cdot h^{-1}$, H_2/CO_2 = 3:1.

The slight decrease in apparent activation energy for CH_4 production efficiency on the composite catalyst suggests potential roughness in catalytic activity from 513 K to 573 K (**Figure S2-3 and S2-6**). The TOF results (**Table S2-2**) demonstrate an optimal temperature range within which catalytic performance is optimized. At elevated temperatures, there is dynamic restructuring of active sites, which enhances activity. Conversely, at lower temperatures, excessive surface coverage and electronic deactivation suppress intrinsic turnover.

2.4.4 Optimizing the parameters to increase the C_2+ STY and analyzing the reaction stability

As demonstrated in **Figure 2-6**, elevated reaction pressure significantly enhances both CO_2 conversion and C_2+ hydrocarbon formation by enhancing the effective concentration of reactants, thus facilitating more efficient C-C coupling. An increase in both CO_2 conversion and C_2+ space time yield (STY) was observed as pressure increased from 0.1 to 3 MPa. In particular, there was a substantial improvement in C_2+ selectivity, which increased from 9.7% to 41.4%, while the corresponding C_2+ STY rose from 0.48 to 21.3 mmol·g_{cat}^{-1}·h^{-1} under CO free conditions. Concurrently, there was an increase in CO_2 conversion from 0.8% to 8.6%. The results obtained demonstrate unequivocally that pressure is a pivotal factor in the direction of CO_2 hydrogenation towards higher hydrocarbons, with both conversion and C_2+ productivity exhibited a linear relationship with increasing pressure.

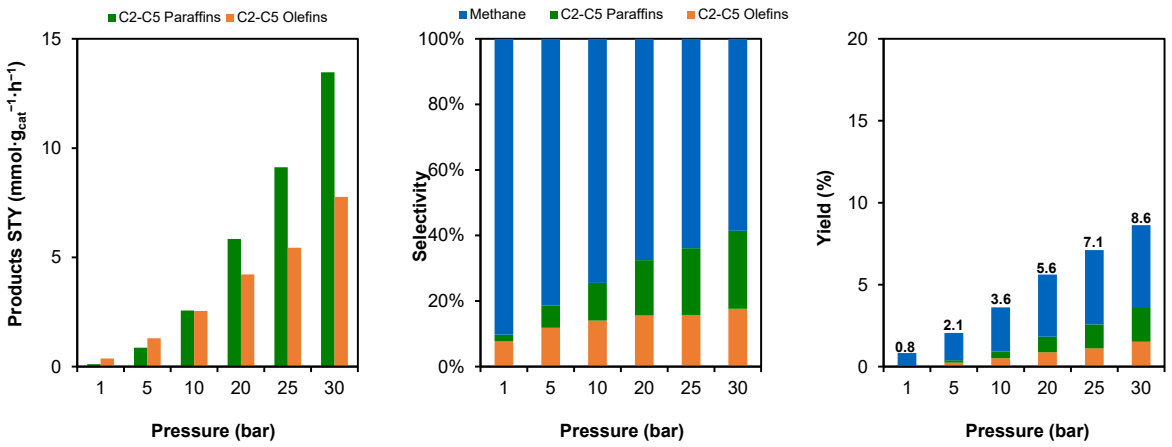

Figure 2-6. (**Left**) C_2-C_5 olefins and paraffins HCs space time yield (STY) for different pressure. (**Center**) Catalytic performance on 0.75 wt% Na-CoO_x at 300°C with pressure shift. (**Right**) Catalytic yield for 0.75 wt% Na-CoO_x at 300°C with pressure shift. All the experiments are regarded as CO free and analyzed at 0.1-3.0 MPa MPa, space velocity = 150 L·g_{cat}^{-1}·h^{-1}, H_2/CO_2 = 3.

The effect of space time has been demonstrated to manifest a complex dependence on paraffin and olefin formation[17]. At the optimized pressure of 3 MPa, an increase in the space time from 0.02-0.25 s resulted in a gradual decrease in the STY of olefins from 9.2 to 3.3 mmol·g_{cat}^{-1}·h^{-1}. However, the STY of paraffins exhibited a mountain-like trend, reaching a peak of 14.0 mmol·g_{cat}^{-1}·h^{-1} before declining to approximately 9.8 mmol·g_{cat}^{-1}·h^{-1}(**Figure 2-7**). In circumstances where a low space time is established, the activation of CO_2 and the subsequent formation of hydrocarbons are constrained by the reduction in C-O bond cleavage, C-H bonding and secondary hydrogenation of olefins, thereby promoting their selectivity while concurrently

limiting paraffin formation. The lower space time indicates that there is a lower CO_2 conversion and somehow demonstrates a lower products yield by the inadequate C-O bond cleavage and C-H hydrogenation, thus, the increase in the yield compared to conversion as the space time increases. (**Figure S2-7**)

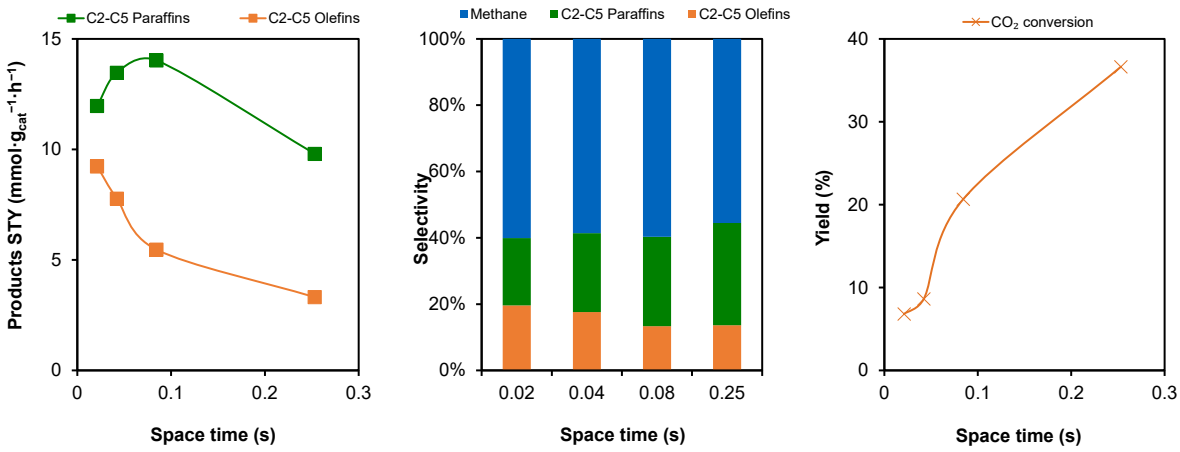

Figure 2-7. (**Left**) C_2-C_5 olefins and paraffins HCs space time yield (STY) for adjusted space time. (**Center**) Catalytic performance for 0.75 wt% Na-CoO_x with space time shift. (**Right**) Catalytic yield for 0.75 wt% Na-CoO_x with space time shift. All the experiments are regarded as CO free and analyzed at 300°C, 3.0 MPa, space time = 0.02-0.25 s, H_2/CO_2 = 3.

The present study sets out to evaluate the stability of the activated 0.75 wt% Na-CoO_x catalyst under demanding reaction conditions. The reaction conditions refer to a total pressure of 30 bar, a ratio of H_2 and CO_2 of 3:1, a space velocity of 150 $L \cdot g_{cat}^{-1} \cdot h^{-1}$, and a temperature of 300 °C. It is noteworthy that the catalyst exhibited consistent CO_2 conversion over a duration of 50 h, accompanied by a steady selectivity towards long-chain hydrocarbons (C_2+ paraffins and olefins), as demonstrated in **Figure 2-8**. The findings indicate that the activated 0.75 wt% Na-CoO_x catalyst possesses remarkable stability and durability under conditions of high pressure CO_2 hydrogenation, maintaining both activity and product distribution without undergoing deactivation or selectivity drift.

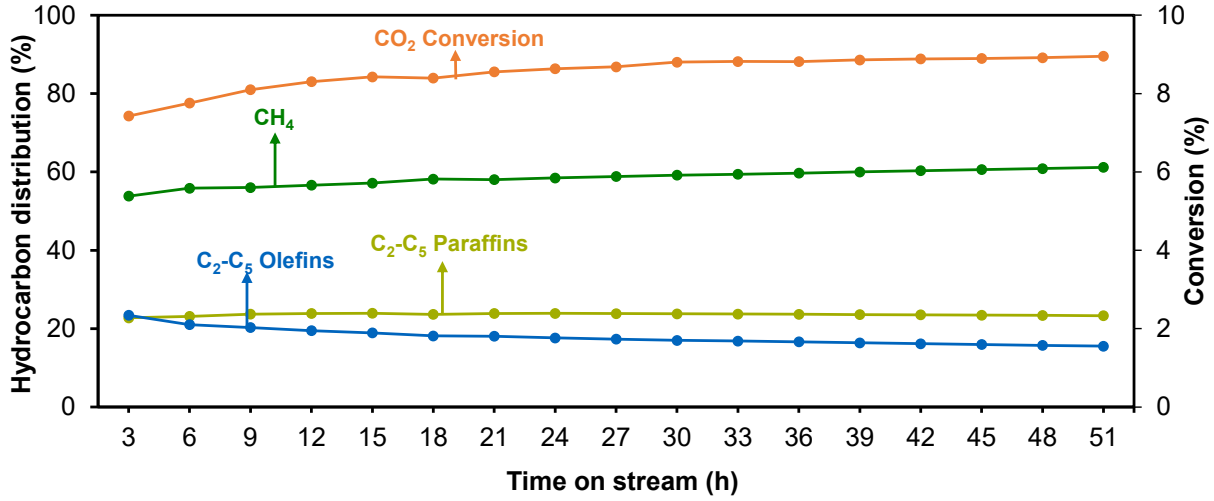

Figure 2-8. The stability of catalytic yield and selectivity of the products (methane, C_2-C_5 olefins and paraffins HCs) of 0.75 wt% Na-CoO_x. All the experiments are regarded as CO free and analyzed at 300°C, 3.0 MPa, space velocity = 150 $L \cdot g_{cat}^{-1} \cdot h^{-1}$, $H_2/CO_2 = 3$.

2.4.5 The intermediate analysis of the alkali promoted and blank catalysts

The primary focus of this discussion will be on the intermediate's ratio of CH_2/CH_3 as a means of enhancing the C-C coupling capability. In order to gain mechanistic insights into the reaction pathways, in situ diffuse reflectance infrared Fourier transform spectroscopy (DRIFTS) was employed to probe surface intermediates formed during the RWGS-FTS reaction over metallic Co and Na-modified CoO_x catalysts (**Figures 2-9, Table S2-5**).

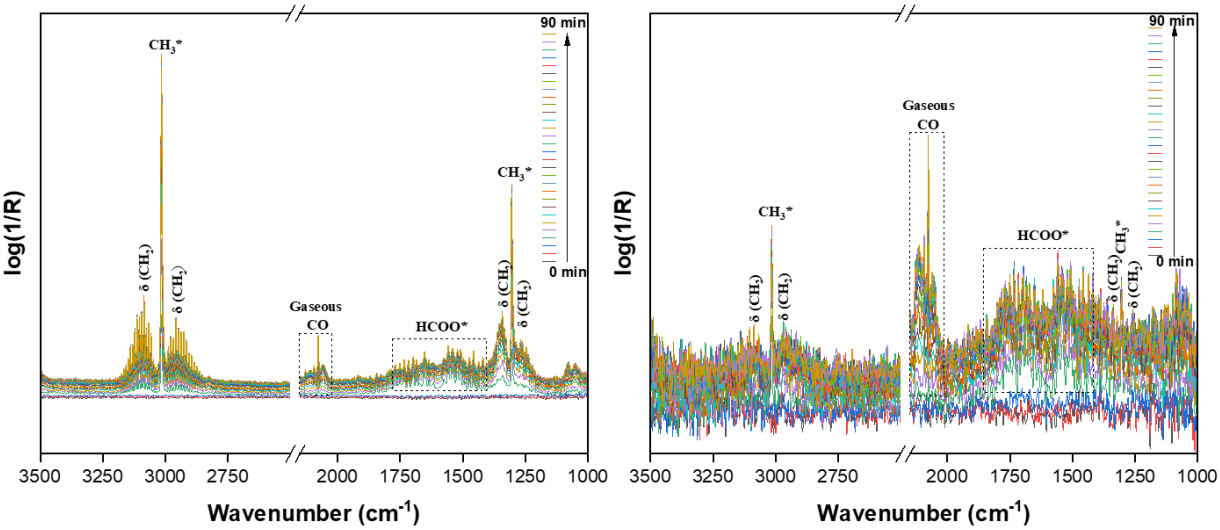

Figure 2-9. In situ DRIFTS spectra of the CO_2 + H_2 reaction over the metallic Co and 0.75wt% Na-CoO_x catalyst. (**Left**) dynamic spectra at the region of 1000–3500 cm^{-1} at 250 °C temperatures of metallic Co after 90 min and

(**Right**) dynamic spectra at the region of 1000–3500 cm^{-1} at 250 °C temperatures of 0.75wt% Na-CoO_x after 90 min. Conditions: 2 MPa, 20 mL·min^{-1}, H_2/CO_2 = 3.

Upon heating to 250 °C, the emergence of gaseous CO and CH_4 was observed, alongside the appearance of characteristic vibrational bands corresponding to adsorbed *CH_x and *CH_xO species intermediates typically associated with CO-mediated Fischer-Tropsch synthesis (FTS) pathways. Time-resolved DRIFTS spectra collected at 250 °C reveals a progressive increase in the intensities of bands assigned to *CH_x, *HCOO, and *CO species, further supporting the involvement of a CO-intermediate mechanism in the FTS process (**Figures 2-9 Left**). It is noteworthy that the formation of *CH_x intermediates was found to be significantly suppressed in the presence of Na (**Figures 2-9 Right**). This observation indicates that Na modifies not only the surface electronic environment but also the dynamics of hydrogenation. Specifically, it is likely to promote the coupling of surface *CH_2 species, thereby favoring C-C bond formation over their direct hydrogenation to methane. It can be hypothesized that the enhanced probability of *CH_2-*CH_2 coupling over the Na-CoO_x surface may account for the increased selectivity towards C_2+ hydrocarbons.

The valence theory is the fundamental principle that enables the observation of the change in CH_x by Co^{2+} and Co^{3+}. Consequently, the XPS analysis was employed to elucidate the variation in the amount of Co^{3+}/ Co^{2+}. Moreover, the XPS results (**Figure 2-10**) indicate the electron transfer from Na to Co and O species, which influences the adsorption/activation of reactants and intermediates at the Na-Co interfaces.

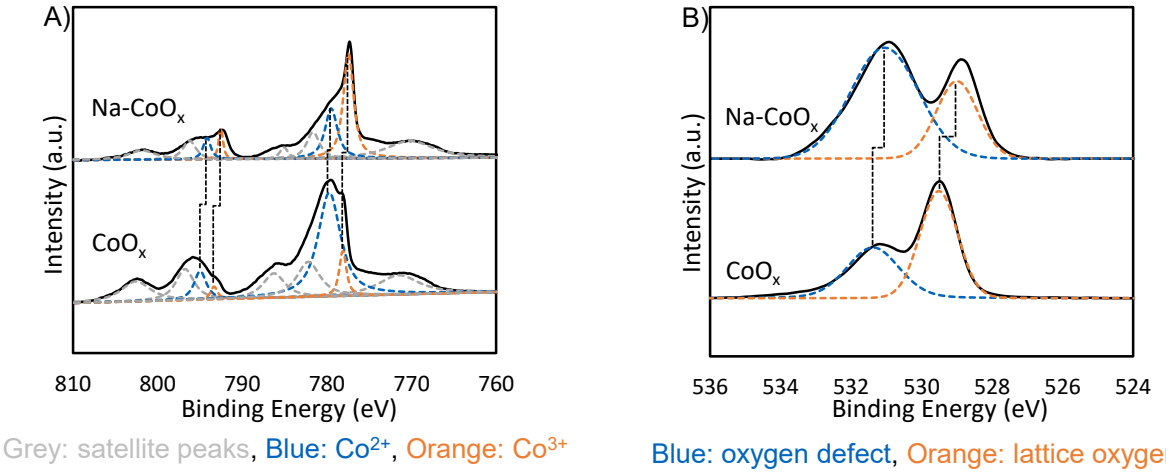

Figure 2-10. Identification the interfaces valence of the Na-CoO_x and CoO_x. (**Left**) Deconvolution of Co 2p XPS spectra (Grey: satellite peaks, Blue: Co^{2+}, Orange: Co^{3+}); (**Right**) Deconvolution of O 1s XPS spectra (Blue: oxygen vacancies, Orange: lattice oxygen); of reduced samples of Co_3O_4 and 0.75wt% Na-CoO_x.

Sodium doping has been demonstrated to exert a dual electronic effect on the catalyst surface. XPS analysis provides compelling evidence that Na plays a decisive role in restructuring the electronic and surface properties of cobalt oxides. It has been demonstrated that Na functions as an electron donor, thereby enhancing the electron shielding within the lattice and thereby lowering the binding energies of Co 2p and O 1s in the XPS spectra. Concurrently, to maintain overall charge neutrality, a charge compensation mechanism is initiated, whereby a proportion of Co^{2+} is oxidized to Co^{3+} as a consequence of the partial substitution of Co^{3+} sites by Na^{+} (**Figure 2-10 left and S2-11**). This process leads to an increased Co^{3+}/Co^{2+} ratio, thereby modulating the redox balance of the catalyst surface. Of particular significance is the observation that the O 1s spectra displays a marked increase in oxygen vacancy concentration upon Na incorporation (**Figure 2-10 right**), which in turn exposes a greater density of Na-Co interfacial sites as pivotal centers that facilitate C-C coupling. Finally, the Na 1s spectra provides unequivocal verification of the presence of Na in the doped catalysts (**Figure S2-12**), thereby reinforcing its structural and functional integration.

Collectively, these spectroscopic insights demonstrate that Na not only alters the reducibility and electronic state of cobalt, as well as creating highly active interfacial environments that drive selective C-C bond formation. The presence of Na^{+} within the structure has been demonstrated to increase CO_2 adsorption, adjust the valence of metals and hinder the further hydrogeantion of the intermediates, thus the olefins products were increased. .

In-situ XRD has been demonstrated to reveal the state of real active sites, thus enabling confirmation of the valence influence with the support of TPR. Operando X-ray diffraction (XRD) patterns of the synthesized catalysts revealed distinct peaks corresponding to the cubic phase of Co_3O_4 catalyst. As the temperature increased in the Co_3O_4 sample with hydrogen flow, a slight shift from Co_3O_4 to hcp-Co and CoO to hcp-Co diffraction peaks was observed, suggesting the reduction of Co_3O_4 into Co around 553 K. Similarly, as the temperature of the 0.75wt% Na-CoO_x sample was increased in the presence of hydrogen, a slight shift from Co_3O_4 to hcp-Co and CoO diffraction peaks were observed, suggesting the existence of a small amount of CoO during the reaction (**Figure 2-11**).

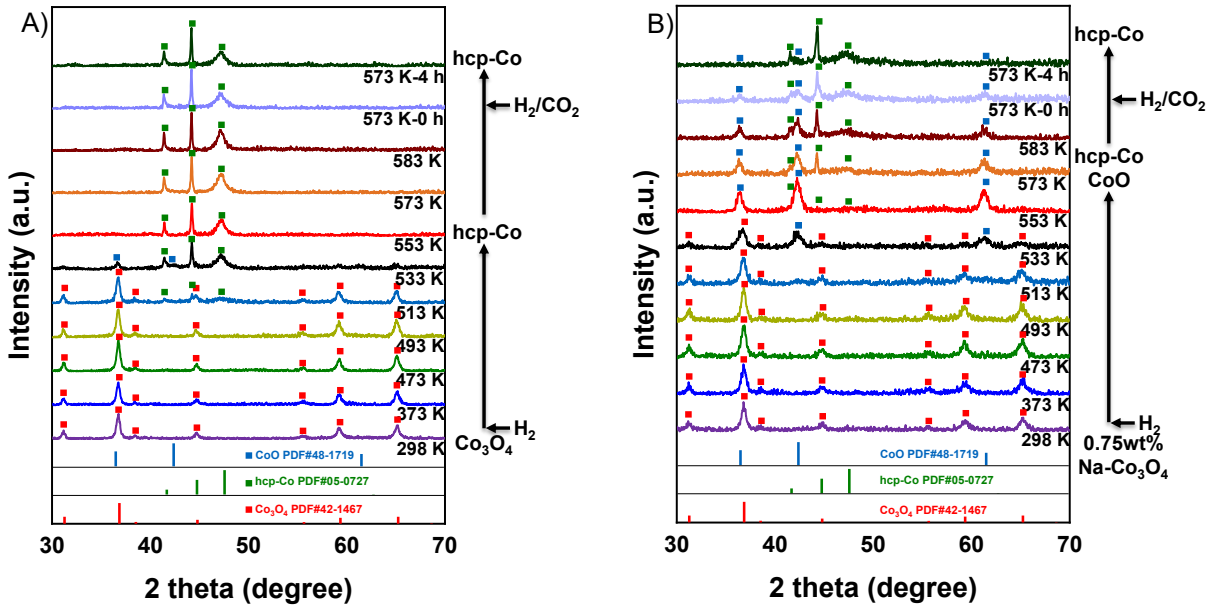

Figure 2-11. In situ XRD patterns of Co_3O_4 (**Left**)and 0.75wt% Na-CoO_x (**Right**) in CO_2 hydrogenation at 1bar.

The absence of sodium composites peaks indicated the formation of a highly dispersed sodium composites phase, devoid of large agglomerates. It was established that the addition of sodium resulted in an augmentation of the complete reduction temperature delay, thereby indicating that it functions as an inhibitor of the reduction of cobalt oxide towards the Co and revealing the function between cobalt oxide and hcp-Co[29]. The TPR result for each catalyst confirmed a reduced temperature shift of approximately 20K from 555 K to 576 K, which was necessary to obtain the metallic cobalt. (**Figure S2-8**).

Metallic Co sites have been shown to facilitate the conversion of the CH_2 to CH_3 intermediates in the context of C_2+ hydrocarbon, thereby contributing to the process of C-C coupling. Importantly, C_2+ hydrocarbons can originate from both the RWGS and formate pathways. The chemical environment of cobalt active sites plays a critical role in governing CO_2 hydrogenation pathways, highlighting the importance of site engineering and catalyst design in optimizing hydrocarbon formation. The TOF of each catalyst is influenced by the addition of a various amount of Na with the dispersion of Co shifts from 8% to 3%[30]. The utilization of novel technologies and a plethora of operando technologies has the potential to facilitate the design of new catalysts and the analysis of active site components in the future[31].

2.5 Conclusion

The present study focuses on Co_3O_4 catalysts, with the aim of identifying the sodium content sensitivity of CO_2 hydrogenation as a case study. A particular focus of the present study

has been paid to the specific reaction products of the catalysts and the correlation of these with the textural and structural characteristics of Na-CoO_x samples.

Based on our analysis, the focus on developing Co_3O_4 catalysts with low specific surface areas alone is inadequate for the effective preparation of a highly active oxidation catalyst since the challenge is to tailor the Na content to favor the development of surface traits that also contribute to the enhancement of the interface activity of metallic cobalt and CoO_x and to hinder the CH_2 to CH_3 intermediates conversion. The incorporation of sodium resulted in an increase in the complete reduction in temperature, with a delay exceeding 20 K observed. The selection of pure oxide as the designated choice in the present study was a deliberate step taken to eliminate the influence of interactions among cations or the structure, which otherwise would have complicated the analysis of catalytic performance metrics. This methodological approach is intended to ensure that the performance evaluation of the catalyst is based solely on its activity and not on any external factors that may interfere. It is noteworthy that the insights gained from this work can serve as a paradigm for other sodium doped Co-based catalysts that are commonly used in the C_2+ products synthesis.

2.6 Acknowledgements

C. L. is grateful to the Chinese Scholarship Council for financial support.

2.7 Appendix

Figure. S2-1.

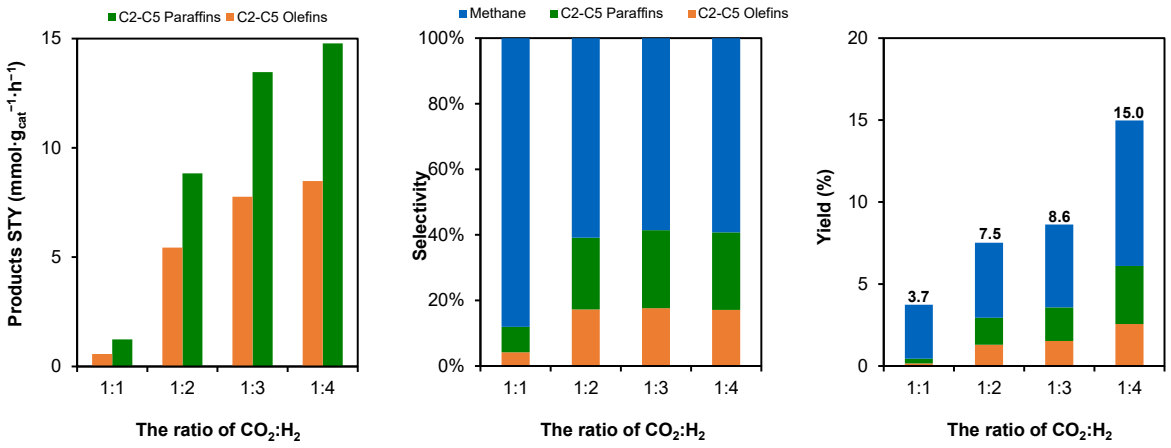

Figure. S2-1. Catalytic performance of 0.75wt% Na-CoO_x catalysts prepared using different CO_2/H_2 ratio from 1/1-1/4. All the experiments are regarded as CO free and analyzed at 300 °C, 3.0 MPa, space velocity = 150 $L \cdot g_{cat}^{-1} \cdot h^{-1}$. Controlling CO_2 as 9 mL/min and changing the ratio of H_2.

Figure. S2-2.

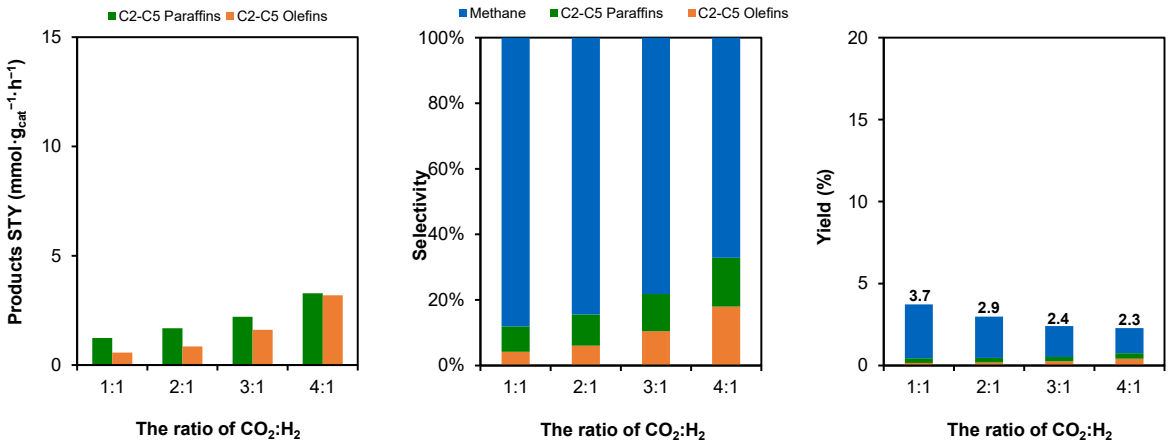

Figure. S2-2. Catalytic performance of 0.75wt% Na-CoO_x catalysts prepared using different CO_2/H_2 ratio from 1/1-4/1. All the experiments are regarded as CO free and analyzed at 300 °C, 3.0 MPa, space velocity = 150 $L \cdot g_{cat}^{-1} \cdot h^{-1}$. Controlling H_2 as 9 mL/min and changing the ratio of CO_2.

Figure. S2-3.

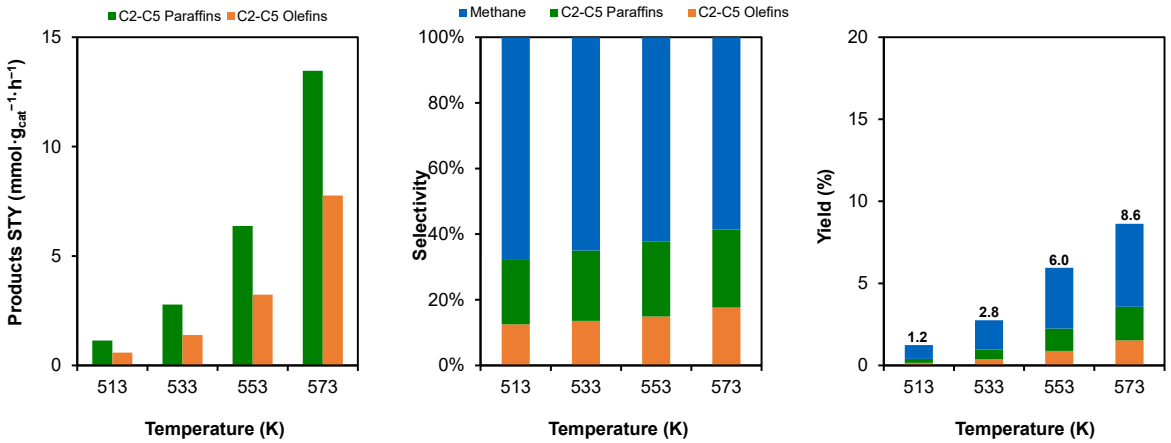

Figure. S2-3. Catalytic performance of 0.75wt% Na-CoO_x catalysts prepared using different temperatures. All the experiments are regarded as CO free and analyzed at 240-300 °C, 3.0 MPa, space velocity = 150 $L \cdot g_{cat}^{-1} \cdot h^{-1}$.

Figure. S2-4.

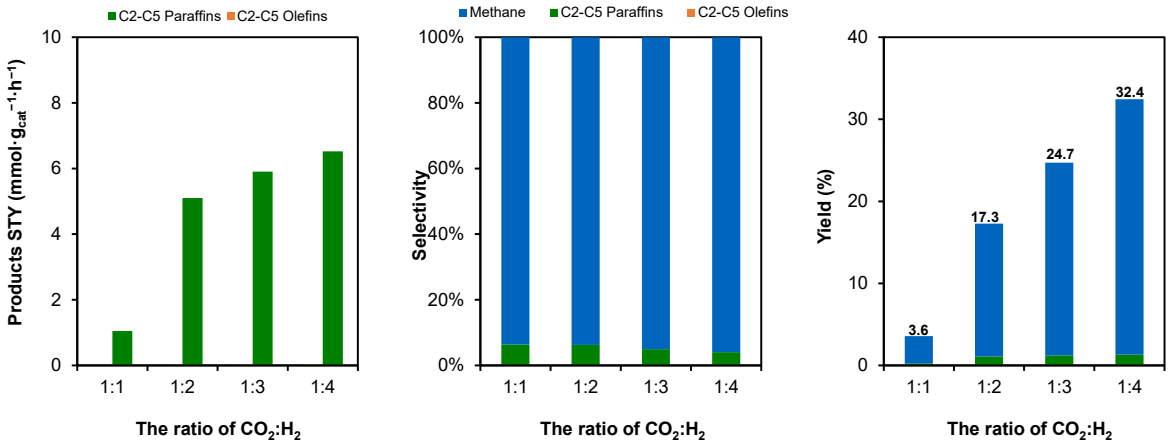

Figure. S2-4. Catalytic performance of Co_3O_4 catalysts prepared using different CO_2/H_2 ratio from 1/1-1/4. All the experiments are regarded as CO free and analyzed at 300 °C, 3.0 MPa, space velocity = 150 $L \cdot g_{cat}^{-1} \cdot h^{-1}$. Controlling CO_2 as 9 mL/min and changing the ratio of H_2.

Figure. S2-5.

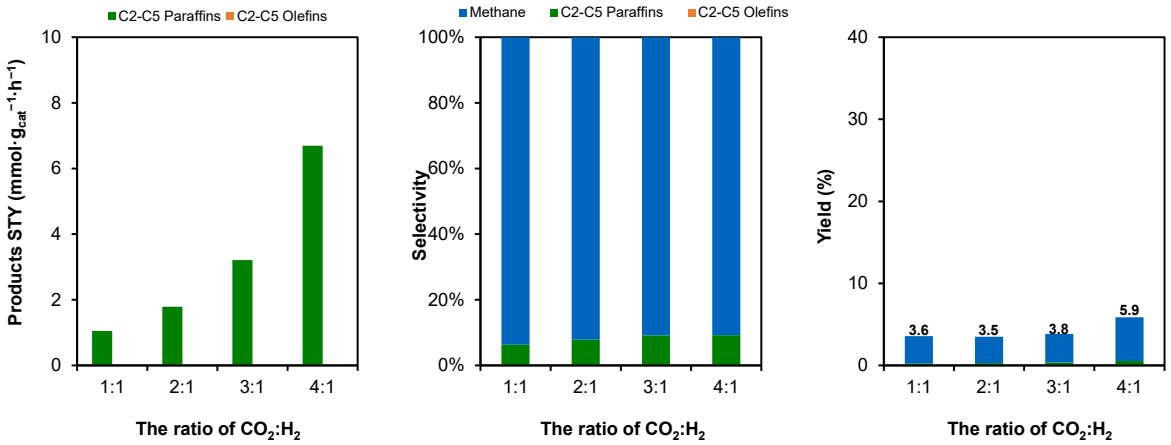

Figure. S2-5. Catalytic performance of Co_3O_4 catalysts prepared using different CO_2/H_2 ratio from 1/1-4/1. All the experiments are regarded as CO free and analyzed at 300 °C, 3.0 MPa, space velocity = 150 $L \cdot g_{cat}^{-1} \cdot h^{-1}$. Controlling H_2 as 9 mL/min and changing the ratio of CO_2.

Figure. S2-6.

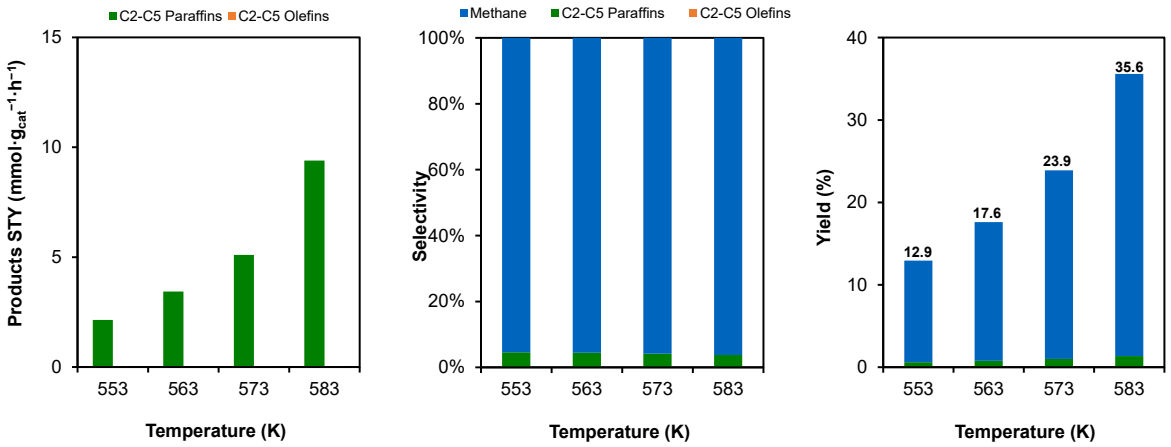

Figure. S2-6. Catalytic performance of Co_3O_4 catalysts prepared using different temperatures. All the experiments are regarded as CO free and analyzed at 280-310 °C, 3.0 MPa, space velocity = 150 $L \cdot g_{cat}^{-1} \cdot h^{-1}$.

Figure. S2-7.

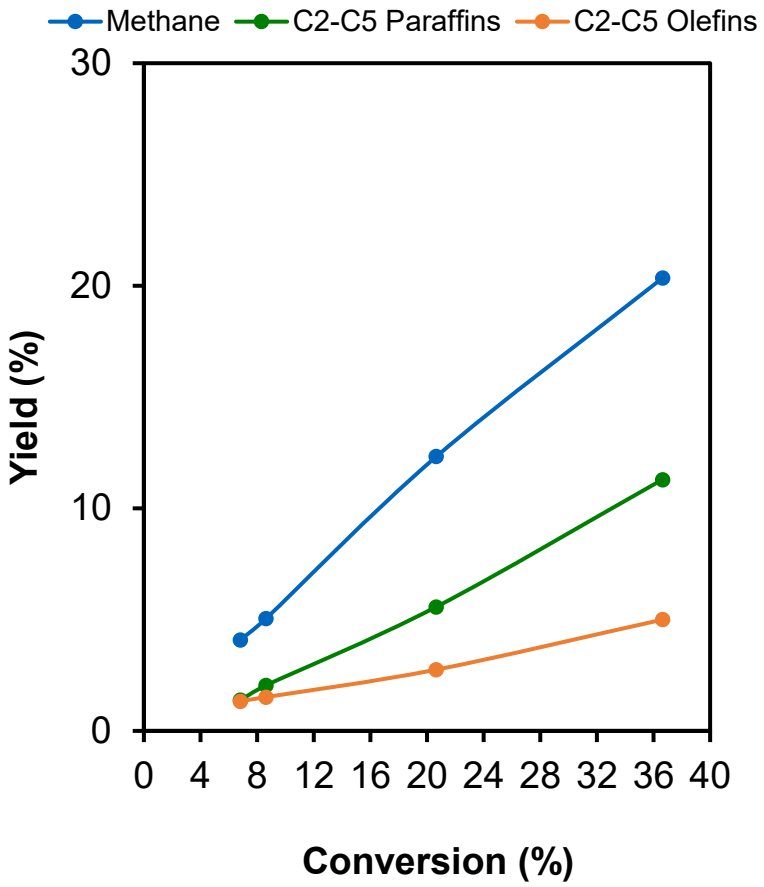

Figure. S2-7 Methane, C_2-C_5 olefins and paraffins HCs catalytic yield for 0.75 wt% Na-CoO_x with CO_2 conversion shift. All the experiments are regarded as CO free and analyzed at 300°C, 3.0 MPa, space time = 0.02-0.25 s, H_2/CO_2 = 3.

Figure. S2-8.

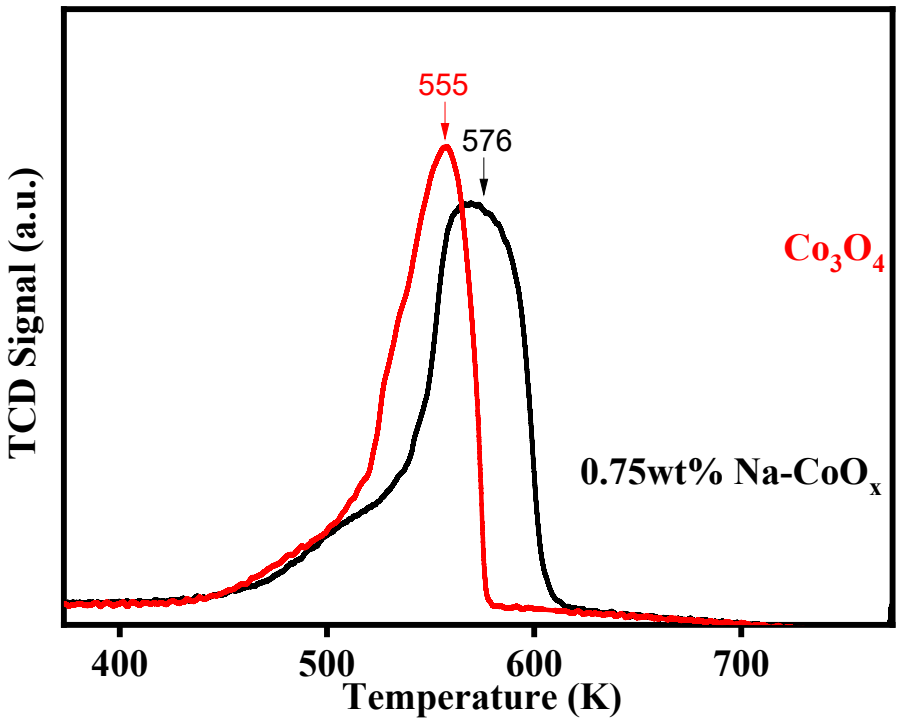

Figure. S2-8. H_2-TPR profiles of Co_3O_4 and 0.75 wt% Na-CoO_x catalysts.

Figure. S2-9.

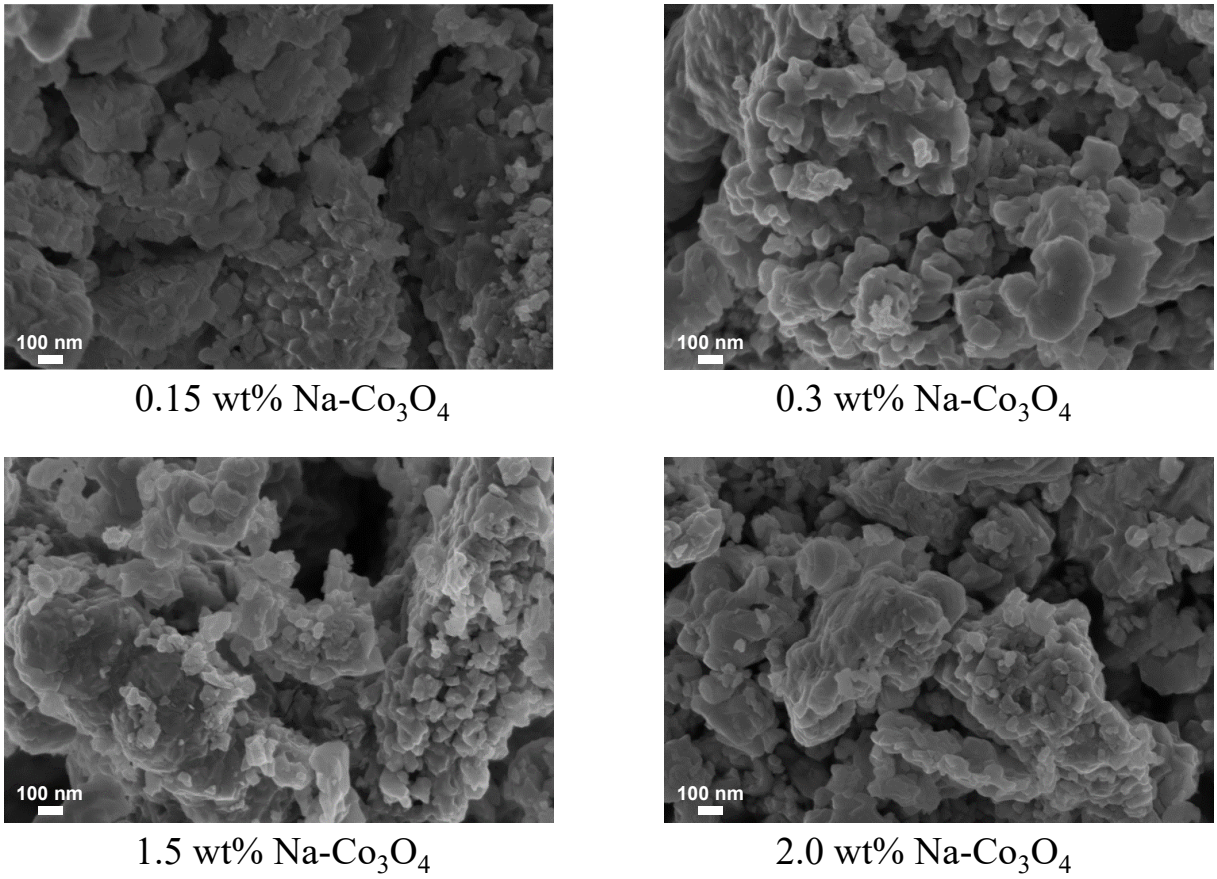

Figure. S2-9. SEM images of 0.15 wt% Na-CoO_x, 0.30 wt% Na-CoO_x, 1.50 wt% Na-CoO_x, 2.00 wt% Na-CoO_x catalysts.

Figure. S2-10.

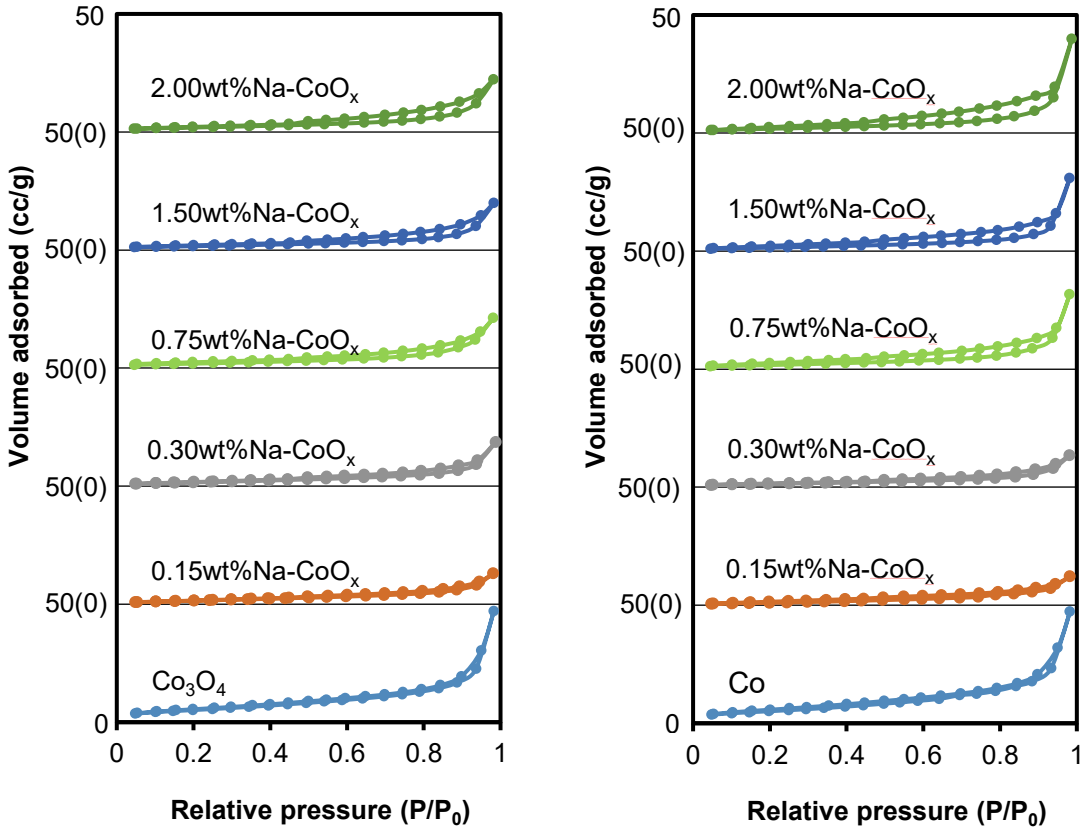

Figure. S2-10. BET surface area analysis results: N_2-adsorption-desorption isotherm plots of Co_3O_4, 0.15 wt% Na-CoO_x, 0.30 wt% Na-CoO_x, 0.75 wt% Na-CoO_x, 1.50 wt% Na-CoO_x, 2.00 wt% Na-CoO_x catalysts and reduced series catalysts.

Figure. S2-11.

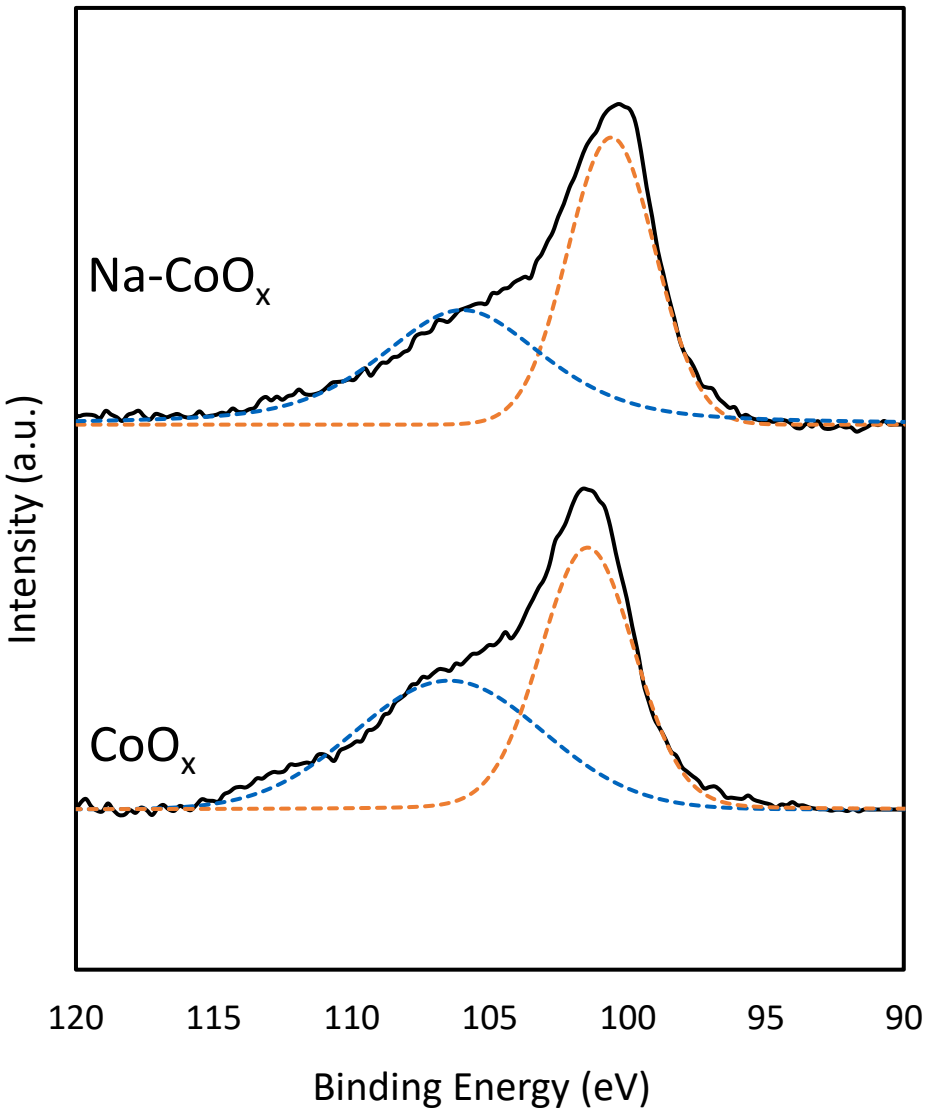

Figure. S2-11. Deconvolution of Co 3s region (in XPS data) of the samples of CoO_x and 0.75wt% Na-CoO_x.

Figure. S2-12.

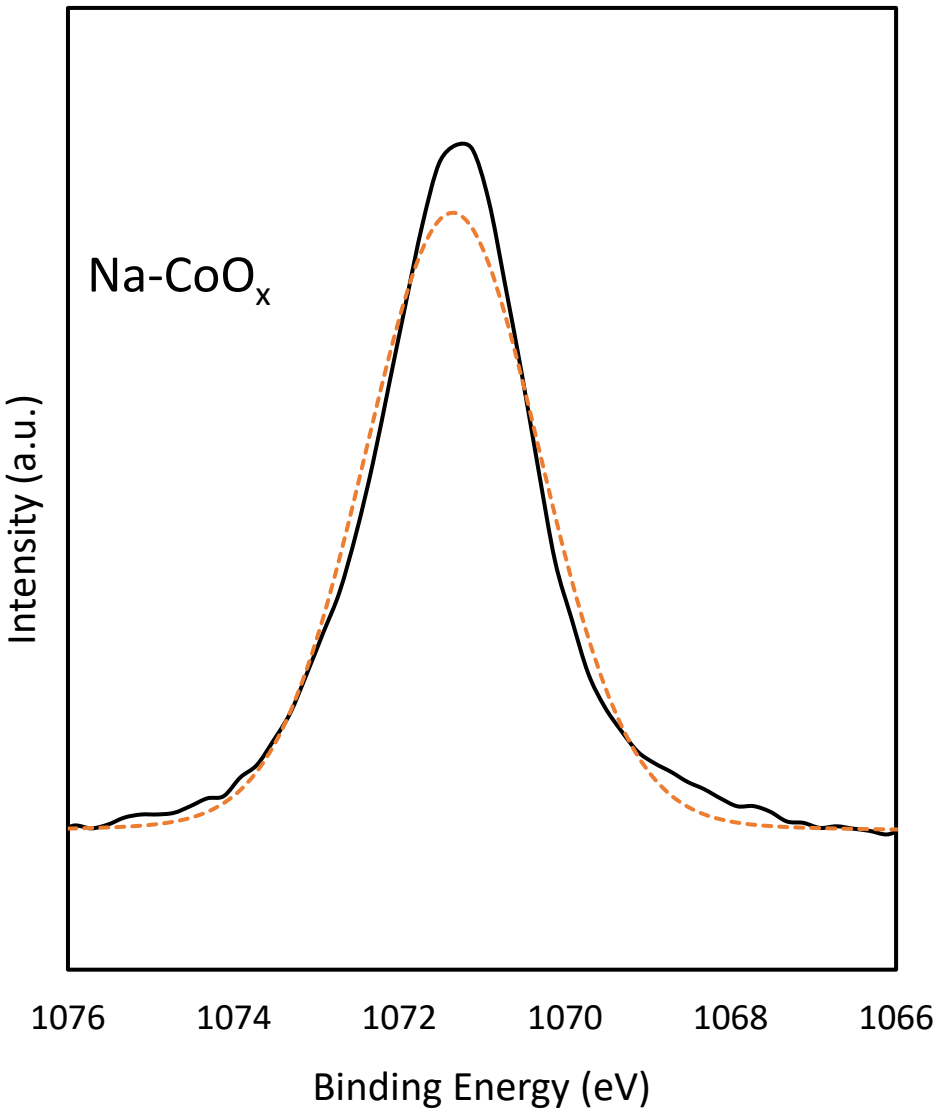

Figure. S2-12. Deconvolution of Na 1s region (in XPS data) of the samples of 0.75wt% Na-CoO_x.

Table. S2-1.

Catalysts	Na content (%)	Co content (%)
0.15 wt% Na-CoO_x	**0.079**	**68.5**
0.30 wt% Na-CoO_x	**0.294**	**72.8**
0.75 wt% Na-CoO_x	**0.684**	**74.1**
1.50 wt% Na-CoO_x	**1.370**	**67.6**
2.00 wt% Na-CoO_x	**1.830**	**70.8**

Table. S2-1. The elements content of Co_3O_4, 0.15 wt% Na-CoO_x, 0.30 wt% Na-CoO_x, 0.75 wt% Na-CoO_x, 1.50 wt% Na-CoO_x, 2.00 wt% Na-CoO_x catalysts analyzed by AAS.

Table. S2-2.

Temperature (K)	TOF of 0.75wt%Na-CoO_x (s^{-1})
513	0.01
533	0.02
553	0.05
573	0.10

Table. S2-2. The turnover frequency of 0.75 wt% Na-CoO_x catalyst from 513 to 573 K.

Table. S2-3.

Catalysts	Surface area (m^2/g)
Metallic cobalt	**18.92**
0.15 wt% Na-CoO_x	**4.66**
0.30 wt% Na-CoO_x	**5.43**
0.75 wt% Na-CoO_x	**6.81**
1.50 wt% Na-CoO_x	**5.76**
2.00 wt% Na-CoO_x	**7.04**

Table. S2-3. The surface area of all the reduced catalyst.

Table. S2-4.

Catalysts	Co dispersion (%)
Metallic cobalt	**8.1**
0.15 wt% Na-CoO_x	**3.8**
0.30 wt% Na-CoO_x	**3.6**
0.75 wt% Na-CoO_x	**2.3**
1.50 wt% Na-CoO_x	**2.5**
2.00 wt% Na-CoO_x	**2.8**

Table. S2-4. The Co dispersion of all the catalysts with the result of H_2 chemisorption and AAS.

Table. S2-5.

Surface species	Wavenumber (cm^{-1})	Ref.
CH_4	3015, 1303	ACS Catal. 2023, 13, 7, 4667–4674 Angew. Chem. Int. Ed. 2020, 59, 19983–19989
$*CH_x$	3017, 2966, 2956, 2928, and 2856	Appl. Catal., B 2021, 298, 120567 J. Phys. Chem. C 2011, 115, 1361–1367
$*CH_xO$	2937-2941 1070-1082 2824-2826 1270, 1034	ACS Catal. 2020, 10, 24, 14516–14526 ACS Catal. 2023, 13, 7, 4667–4674 ACS Catal. 2020, 10, 21, 12828–12840
Gaseous CO	2176, 2110, 2085	ACS Catal. 2020, 10, 9, 5250–5260 ACS Catal. 2023, 13, 7, 4667–4674
Bridged carbonyl species	1900-2060	Nat. Catal., 2018, 127–134
*HCOO	1337-1393 1593-1622	ACS Catal. 2023, 13, 7, 4667–4674 ACS Catal. 2020, 10, 24, 14516–14526
$*CO_3$	1393, 1325 and 1274	ACS Catal. 2023, 13, 7, 4667–4674 Appl. Catal., A 2025, 288, 126-133

Table. S2-5. The assignments of IR bands in the DRIFTS spectra

2.8 Reference

1 C. Hepburn, E. Adlen, J. Beddington *et al.* The technological and economic prospects for CO_2 utilization and removal. *Nature*, 575 (2019) 87-97.

2 D. U. Nielsen, X. M. Hu, K. Daasbjerg & T. Skrydstrup. Chemically and electrochemically catalysed conversion of CO_2 to CO with follow-up utilization to value-added chemicals. *Nat. Catal.*, 1 (2018) 244-254.

3 J. Rogelj, M. den Elzen, N. Hohne *et al.* Paris Agreement climate proposals need a boost to keep warming well below 2ºC. *Nature*, 534 (2016) 631-639.

4 R. Sang, Y. Hu, R. Razzaq *et al.* A practical concept for catalytic carbonylations using carbon dioxide. *Nat. Commun.*, 13 (2022) 4432.

5 S. J. Davis, K. Caldeira & H. D. Matthews. Future CO_2 Emissions and Climate Change from Existing Energy Infrastructure. *Science*, 329 (2010) 1330-1333.

6 J. Chang, P. Ciais, T. Gasser *et al.* Climate warming from managed grasslands cancels the cooling effect of carbon sinks in sparsely grazed and natural grasslands. *Nat. Commun.*, 12 (2021) 118.

7 N. M. Dowell, P. S. Fennell, N. Shah & G. C. Maitland. The role of CO_2 capture and utilization in mitigating climate change. *Nat. Clim. Change*, 7 (2017) 243-249.

8 R. E. Zeebe, J. C. Zachos, K. Caldeira & T. Tyrrell. Carbon Emissions and Acidification. *Science*, 321 (2008) 51-52.

9 Y. Xie, T. T. Wang, X. H. Liu, K. Zou & W. Q. Deng. Capture and conversion of CO_2 at ambient conditions by a conjugated microporous polymer. *Nat. Commun.*, 4 (2013) 1960.

10 S. De, A. Dokania, A. Ramirez & J. Gascon. Advances in the Design of Heterogeneous Catalysts and Thermocatalytic Processes for CO_2 Utilization. *ACS Catal.*, 10 (2020) 14147-14185.

11 H. M. T. Galvis, J. H. Bitter, C. B. Khare *et al.* Supported Iron Nanoparticles as Catalysts for Sustainable Production of Lower Olefins. *Science*, 335 (2012) 835-838.

12 J. Liang, J. Liu, L. Guo *et al.* CO_2 hydrogenation over Fe-Co bimetallic catalysts with tunable selectivity through a graphene fencing approach. *Nat. Commun.*, 15 (2024) 512.

13 W. Fang, C. Wang, Z. Liu *et al.* Physical mixing of a catalyst and a hydrophobic polymer promotes CO hydrogenation through dehydration. *Science*, 377 (2022) 406–410.

14 C. Yang, H. Zhao, Y. Hou & D. Ma. Fe_5C_2 nanoparticles: a facile bromide-induced synthesis and as an active phase for Fischer-Tropsch synthesis. *J. Am. Chem. Soc.*, 134 (2012) 15814-15821.

15 Y. Xu, P. Zhai, Y. Deng *et al.* Highly Selective Olefin Production from CO_2 Hydrogenation on Iron Catalysts: A Subtle Synergy between Manganese and Sodium Additives. *Angew. Chem. Int. Ed*, 59 (2020) 21736-21744.

16 Y. Chen, Y. Zhang, W. Lin *et al.* Catalytically efficient Co-CoO_x-Al_2O_3 interface for mild temperature fatty alcohol production via fatty acid transfer hydrogenation. *Fuel*, 345 (2023) 128136.

17 W. Fu, S. Liu, Y. He *et al.* CO_2 hydrogenation over CoAl based catalysts: Effects of cobalt-metal oxide interaction. *Appl. Catal., A*, 678 (2024) 119720.

18 I. C. T. Have, J. J. G. Kromwijk, M. Monai *et al.* Uncovering the reaction mechanism behind CoO as active phase for CO_2 hydrogenation. *Nat. Commun.*, 13 (2022) 324.

19 S. Kattel, P. J. Ramírez, J. G. Chen, J. A. Rodriguez & P. Liu. Active sites for CO_2 hydrogenation to methanol on Cu/ZnO catalysts. *Science*, 355 (2017) 1296-1299.

20 T. Chen, J. Su, Z. Zhang *et al.* Structure Evolution of Co–CoO_x Interface for Higher Alcohol Synthesis from Syngas over Co/CeO_2 Catalysts. *ACS Catal.*, 8 (2018) 8606-8617.

21 S. Kattel, P. Liu & J. G. Chen. Tuning Selectivity of CO_2 Hydrogenation Reactions at the Metal/Oxide Interface. *J. Am. Chem. Soc.*, 139 (2017) 9739-9754.

22 B. Liu, Y. Zha, L. Xin *et al.* Atomic-scale understanding of the impact of CoO phase in cobalt-catalyzed Fischer-Tropsch synthesis: A combined computational and experimental study. *J. Catal.*, 430 (2024) 115307.

23 G. Melaet, W. T. Ralston, C. S. Li *et al.* Evidence of highly active cobalt oxide catalyst for the Fischer-Tropsch synthesis and CO_2 hydrogenation. *J. Am. Chem. Soc.*, 136 (2014) 2260-2263.

24 A. Parastaev, V. Muravev, E. H. Osta *et al.* Breaking structure sensitivity in CO_2 hydrogenation by tuning metal–oxide interfaces in supported cobalt nanoparticles. *Nat. Catal.*, 5 (2022) 1051-1060.

25 T. Fan, H. Liu, S. Shao *et al.* Cobalt Catalysts Enable Selective Hydrogenation of CO_2 toward Diverse Products: Recent Progress and Perspective. *J. Phys. Chem. Lett.*, 12 (2021) 10486-10496.

26 R. P. Ye, J. Ding, W. Gong *et al.* CO_2 hydrogenation to high-value products via heterogeneous catalysis. *Nat. Commun.*, 10 (2019) 5698.

27 K. Y. Kim, H. Lee, W. Y. Noh *et al.* Cobalt Ferrite Nanoparticles to Form a Catalytic Co-Fe Alloy Carbide Phase for Selective CO_2 Hydrogenation to Light Olefins. *ACS Catal.*, 10 (2020) 8660-8671.

28 Z. Li, W. Wu, M. Wang *et al.* Ambient-pressure hydrogenation of CO_2 into long-chain olefins. *Nat. Commun.*, 13 (2022) 2396.

29 M. Wang, P. Wang, G. Zhang *et al.* Stabilizing Co_2C with H_2O and K promoter for CO_2 hydrogenation to C_2+ hydrocarbons. *Sci. Adv.*, 9 (2023) 0167.

30 S. Lyu, L. Wang, J. Zhang *et al.* Role of Active Phase in Fischer–Tropsch Synthesis: Experimental Evidence of CO Activation over Single-Phase Cobalt Catalysts. *ACS Catal.*, 8 (2018) 7787-7798.

31 Z. Li, S. Wang & H. Xin. Toward artificial intelligence in catalysis. *Nat. Catal.*, 1 (2018) 641-642.

Chapter 3

Optimizing Co-Cu-ZrO_x catalysts for enhanced ethanol production from CO_2 through intermediate modulation

The selective formation of ethanol from CO_2 reduction is of substantial interest for sustainable fuel production. While Cu-Zr based catalysts are highly effective for methanol production due to their C-O bond cleavage capability to produce CH_xO intermediates at the Cu-Zr interface, cobalt-based catalysts are more adept at forming alkane products due to their superior C-O cleavage and C-H bonding ability. Notably, the formation of fcc-Co rather than the hcp-Co plays a critical role in steering selectivity toward oxygenates, as fcc-Co exhibits lower CO desorption energy, thereby promoting C_2+ alcohol synthesis over methane formation. Regulating the chemical environment of active sites is pivotal for enhancing the selectivity towards higher alcohols during CO_2 hydrogenation. In this context, the formation of higher alcohols via CH_x and CH_xO intermediates is a plausible mechanism. This study explores the influence of Co and Cu molar ratios on the reduction behavior and interfacial properties of co-precipitated $CoCuZrO_x$ catalysts. Compared to the separated precipitated $CuZrO_x$ loaded Co_3O_4 catalysts, the co-precipitated structure offers enhanced interfacial stabilization and high active fcc-Co sites, thereby promoting selective hydrogenation toward alcohols. We present a Na loaded $CoCuZrO_x$ catalyst that operates effectively, achieving an ethanol yield of 3.80 $mmol \cdot g_{cat}^{-1} \cdot h^{-1}$ much higher than that of a baseline Co catalyst optimized under the same conditions. Mechanistic insights into how metal oxides modulate the catalytic environment are discussed, providing a new strategy for optimizing catalysts for CO_2 to ethanol conversion.*

3.1 Introduction

The increasing atmospheric concentration of carbon dioxide (CO_2) due to anthropogenic activities is a critical driver of climate change. To address this challenge, the development of sustainable methods for CO_2 utilization has become an urgent priority[1]. Among the various approaches, the catalytic hydrogenation of CO_2 into valuable chemicals and fuels offers a promising pathway for both reducing CO_2 emissions and contributing to renewable energy strategies. In particular, the selective formation of ethanol from CO_2 reduction reactions is of great interest due to ethanol's potential as a versatile fuel and chemical feedstock.

Catalyst design is critical for steering selectivity. Cu-Zn-Al, Cu-Zn, Zn-Zr and Cu-Zr based catalysts exhibit high activity for CO_2 hydrogenation to methanol[2-16]. This selectivity arises from efficient C-O bond cleavage at Cu-Zr interfaces, promoting CH_xO intermediates and methanol formation. Conversely, cobalt-based catalysts favor longer-chain hydrocarbons (C_2+) via enhanced C-C coupling[17-22]. This divergence in catalytic behavior highlights the need for further research into the design of catalysts that can selectively promote ethanol formation by balancing these mechanistic pathways.

Recent work suggests bimetallic Co-Cu systems on ZrO_2 may bridge this gap. Cu-Zr sites efficiently generate CH_xO intermediates[23-27] while Co promotes CH_x formation via C=O bond activation[28-30]. The Co-Cu interface facilitates electron transfer, modifying surface electronic structure and potentially enabling C-C coupling between CH_x and CH_xO species to form ethanol[31,32]. Furthermore, alkali metal doping (e.g., sodium) represents a key strategy to tune catalytic performance by modifying electronic/structural properties and reactant/intermediate interactions[33-37]. While sodium's impact on paraffin/olefin selectivity is established[38], alongside potential effects of alkaline earth or transition metals[39,40] in promoting ethanol formation via CH_2 and CH_3 intermediates regulation in Co-Cu-Zr systems requires systematic investigation to enable rational catalyst design for selective CO_2 to ethanol conversion.

The generation of C_1 products through CO_2 hydrogenation may proceed along two distinct routes upon the parameters (**Figure 3-1**). The first is the RWGS pathway, involving the initial hydrogenation of CO_2 into the *HOCO intermediate, followed by C-O bond cleavage to produce *CO species. These species can either desorb directly as carbon monoxide or undergo further hydrogenation into *CH_xO species. The second route is known as the formate pathway, where CO_2 undergoes initial hydrogenation into *HCOO, followed by C-H bonding and C-O cleavage, resulting in *CH_xO species. Subsequently, *CH_xO can undergo further hydrogenation to form methanol or undergo C-O bond scission to yield *CH_x species, which can then be

hydrogenated to methane. The selectivity between methane and methanol depends on the competition between C-O bond scission and the hydrogenation of *CH$_x$O species[41]. Regarding C$_2$+ products, a crucial step involves the integration of *CH$_x$ species into other intermediates.

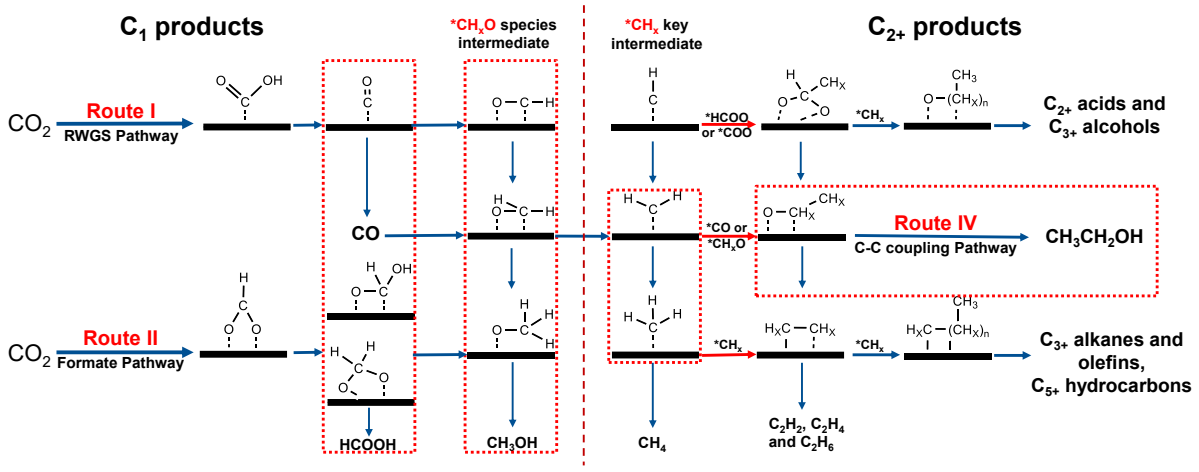

Figure 3-1. Catalytic mechanism of alcohols synthesis

*CH$_x$ can arise from the transformation of *CO, *HCOO or through the de-hydroxylation of methanol. Subsequently, it inserts into another intermediate, facilitating the formation of a C-C bond. This process repeats to elongate the carbon chain. Ultimately, the intermediates undergo further hydrogenation, leading to the production of C$_2$+ alcohols or hydrocarbons. It is noteworthy that the regulation of H$_2$ and CO$_2$ activation is pivotal in controlling the C/H ratio of intermediates, playing a significant role in adjusting product selectivity.

In essence, metallic Co sites excel in H$_2$ dissociation and C-O bond cleavage within the RWGS or RWGS-Fischer-Tropsch Synthesis (FTS) pathway, while Co$^{\delta+}$ sites and oxygen vacancies exhibit a lower capacity for H$_2$ activation but ample ability for active CO$_2$ adsorption, favoring the formate pathway. Additionally, the creation of fcc-Co with lower CO adsorption energy while not hcp-Co facilitates C-C coupling to oxygenates[42], promoting the formation of C$_2$+ oxygenates products. These processes can be enhanced by cobalt interactions with surrounding sites, emphasizing the critical role of controlling the chemical environment of cobalt active sites in governing the product selectivity of CO$_2$ hydrogenation.

The exploration of the development of a Na doping Co-Cu-Zr catalyst is for the high selective hydrogenation of CO$_2$ to ethanol. The objective of this study is to manipulate the reduction and interface properties of the catalyst by adjusting the ratio of Co, Cu and Zr, as well as the Na content. It is anticipated that this approach will regulate the selectivity of CO$_2$ hydrogenation towards ethanol. A series of in-depth mechanistic investigations were conducted

on fcc-Co and hcp-Co using a variety of synthesis methods. These investigations revealed that the structures of these materials are capable of modulating the catalytic environment in a manner that is conducive to the production of ethanol. These findings provide a strategic framework for the design of more efficient catalytic systems, paving the way for advancements in CO_2 to ethanol conversion and broader applications in renewable energy technologies.

3.2 Methods

3.2.1 Chemicals and materials

Cobalt nitrate ($Co(NO_3)_2 \cdot 6H_2O$), copper nitrate ($Cu(NO_3)_2 \cdot 3H_2O$) and zirconium nitrate ($Zr(NO_3)_4 \cdot 5H_2O$), 1,8-Diazabicyclo[5.4.0]undec-7-ene (DBU), NaOH were purchased from Sigma-Aldrich and used without further purification. Megamax 800 ($CuZnAlO_x$) catalyst was purchased from Clariant company. Deionized (DI) water (18.2 $M\Omega \cdot cm^{-1}$) was used to prepare all aqueous solutions.

3.2.2 Sample preparation

3.2.2.1 Precipitation method to synthesis CuO, $CoCuO_x$, $CuZrO_x$, $CoZrO_x$ and ZrO_2

The CuO, $CoCuO_x$, $CuZrO_x$, $CoZrO_x$ and ZrO_2 catalysts were synthesized via a precipitation method, followed by a controlled thermal treatment to achieve optimal dispersion of metal oxides. Initially, aqueous solutions of cobalt nitrate ($Co(NO_3)_2 \cdot 6H_2O$), copper nitrate ($Cu(NO_3)_2 \cdot 3H_2O$) and zirconium nitrate ($Zr(NO_3)_4 \cdot 5H_2O$) were prepared and subsequently mixed in a series of varying combinations (Cu, Co-Cu, Cu-Zr, Co-Zr and Zr). The DBU bio-based solution was added dropwise into a homogenous metal solution under vigorous stirring, with the pH maintained at 10. This precipitation process led to the formation of metal hydroxide precursors, which were then aged at room temperature for 12 hours. The resulting precipitate was filtered, washed with deionized water until almost neutral, and dried at 60°C overnight. The dried samples were subsequently calcined at a temperature of 400°C for a duration of 5 hours in air, with the objective of converting the hydroxides to their respective oxides (CuO, $CoCuO_x$, $CuZrO_x$, $CoZrO_x$ and ZrO_2).

3.2.2.2 Coprecipitation method to synthesis $CoCuZrO_x$ and impregnation method to synthesis Na-$CoCuZrO_x$

The Co-Cu-Zr catalysts were synthesized via a coprecipitation method, followed by a controlled thermal treatment to achieve optimal dispersion of $CoCuZrO_x$. First, aqueous solutions of cobalt nitrate ($Co(NO_3)_2 \cdot 6H_2O$), copper nitrate ($Cu(NO_3)_2 \cdot 3H_2O$) and zirconium

nitrate ($Zr(NO_3)_4 \cdot 5H_2O$) were mixed in varying molar ratios (Co:Cu:Zr= 0.2:1.8:1, 0.6:1.4:1, 1:1:1, 1.4:0.6:1, 1.8:0.2:1). The DBU bio-based solution was added dropwise into a mixed metal solution under vigorous stirring, with the pH maintained at 10. This precipitation process led to the formation of Co, Cu and Zr metal hydroxide precursors, which were then aged at room temperature for 12 hours. The resulting precipitate was filtered, washed with deionized water until almost neutral, and dried at 60°C overnight. The dried samples were subsequently calcined at a temperature of 400°C for a duration of 5 hours in air in order to convert the hydroxides to their respective oxides ($CoCuZrO_x$) with different Co/Cu ratios. Finally, the 0.1 mol/L sodium hydroxide solution and the calcined $Co_1Cu_1ZrO_x$ catalyst were mixed in varying 1wt%, 2wt% and 3wt% mass ratios and dried this sample with rotary evaporator at 60 °C. This precursor was subsequently calcined at a temperature of 400°C for a duration of 5 hours in air to convert the sodium hydroxide to sodium composite to generate the desired Na-$CoCuZrO_x$ catalyst with partially Na composite inside Co, Cu and Zr mixed metals oxide.

3.2.2.3 Precipitation method to synthesis different fractions of x wt% $Cu_2Zr_1O_x$ on Co_3O_4 catalysts ($Co@Cu_2Zr_1O_x$)

The x wt% $Cu_2Zr_1O_x$ on Co_3O_4 catalysts were synthesized via a separated precipitation method. First, aqueous solutions of copper nitrate ($Cu(NO_3)_2 \cdot 3H_2O$) and zirconium nitrate ($Zr(NO_3)_4 \cdot 5H_2O$) were prepared and mixed in Cu-Zr with a constant molar ratio of 2:1. The DBU bio-based solution was droplet added into homogenous metal solution under vigorous stirring, with the pH maintained at 10. This precipitation process led to the formation of metal hydroxide precursors, which were then aged at room temperature for 12 hours. The resulting precipitate was filtered, washed with deionized water until almost neutral, and dried at 60°C overnight. The dried samples were subsequently calcined at a temperature of 400°C for a duration of 5 hours in air to convert the hydroxides to $Cu_2Zr_1O_x$. The next step is that 50 mL aqueous solutions of cobalt nitrate ($Co(NO_3)_2 \cdot 6H_2O$) was mixed with $Cu_2Zr_1O_x$. The resultant mixture was stirred for a period of 6 hours, after which the solution was fully precipitated by the addition of an appropriate quantity of DBU, with the pH maintained in the range of 10. The final catalyst was obtained through calcination at a temperature of 400 °C for a duration of 5 hours in air. The loading amount of the catalyst was controlled by the mass ratio of $Cu_2Zr_1O_x$.

3.2.2.4 Precipitation method to synthesis different fractions of x wt% Co_3O_4 on $Cu_2Zr_1O_x$ catalysts ($Cu_2Zr_1O_x@Co$)

The x wt% Co_3O_4 on $Cu_2Zr_1O_x$ catalysts were synthesized via a separated precipitation method. First, aqueous solutions of cobalt nitrate ($Co(NO_3)_2 \cdot 6H_2O$) was prepared. The DBU

bio-based solution was droplet added into homogenous metal solution under vigorous stirring, maintaining a constant pH of 10. This precipitation process led to the formation of a metal hydroxide precursor, which was then aged at room temperature for 12 hours. The resulting precipitate was filtered, washed with deionized water until almost neutral, and dried at 60°C overnight. The dried samples were subsequently calcined at 400°C for 5 hours in air to convert the hydroxides to Co_3O_4. The next step is that 50 mL aqueous solutions of copper nitrate ($Cu(NO_3)_2 \cdot 3H_2O$) and zirconium nitrate ($Zr(NO_3)_4 \cdot 5H_2O$) were prepared with a constant molar ratio of 2:1 and mixed with Co_3O_4. The resultant mixture was stirred for a period of 6 hours, after which the solution was fully precipitated by the addition of an appropriate quantity of DBU, with the pH maintained in the range of 10. The final catalyst was obtained through calcination at a temperature of 400 °C for a duration of 5 hours in air. The loading amount of the catalyst was controlled by the mass ratio of Co_3O_4.

3.2.2.5 Re-oxidation to synthesis re-oxidized Cu-Zr, $Cu_2Zr_1O_x$ on Co_3O_4 and $Co_1Cu_1Zr_1O_x$ catalysts

The catalysts of Cu-Zr, $Cu_2Zr_1O_x$ on Co_3O_4 and $Co_1Cu_1Zr_1O_x$ catalysts were subjected to treatment in a $2H_2/N_2$ atmosphere at 310 °C in a flow of 50 mL·min^{-1} for 0.5 h. Subsequent to cooling, the catalysts were calcined at a temperature of 400°C for a duration of 5 h in air to effect the conversion of the reduced catalysts into the re-oxidized.

3.2.3 Catalyst testing

The catalytic performance of all catalysts was evaluated within a high-pressure, continuous-flow, fixed-bed reactor. A mixture of 20 mg of x wt% Na-CoCuZrO$_x$ catalysts (250-300цm) and 600 mg of SiC (150-250цm) was prepared and pretreated this mixture in a $2H_2/N_2$ atmosphere at 310 °C in a flow of 50 mL·min^{-1} for 0.5 h. Subsequently, the temperature was reduced to 300 °C, and $CO_2/H_2/N_2$ (18/72/10, 5 MPa) was introduced at a flow rate of 50 mL·min^{-1}. Subsequent to the stabilisation of the pressure and temperature, the gas flow was maintained at 50 mL·min^{-1}. An Agilent chromatograph equipped with a flame ionization detector and a tuning Methanizer. was utilised for the online analysis of products. The catalytic performance of the catalysts was evaluated in terms of CO_2 conversion, product selectivity and space-time yield (STY).

3.2.4 The computational formulas were as follows:

CO_2 conversion, C_{CO2} (%) = $(X_{CO2,\,in} - X_{CO2,\,out})/X_{CO2,\,in} \times 100\%$

Product selectivity, Sel% = $X_{product}/(X_{CO2,\,in} - X_{CO2,\,out}) \times 100\%$

STY of alcohol, $STY_{alcohol}$ ($mmol_{alcohol} \cdot g_{cat}^{-1} \cdot h^{-1}$) = $F_{CO2,\ in} \times C_{CO2} \times Sel_{alcohol} \times 1{,}000/W_{cat}$, where $X_{CO2,\ in}$ and $X_{CO2,\ out}$ are the mole fractions of CO_2 in pristine and exit mixed gas, respectively; $F_{CO2,\ in}$ ($mol \cdot h^{-1}$) is the molar flow rate of CO_2 in pristine mixed gas; W_{cat} (g) is the weight of catalyst.

Space velocity ($L \cdot g_{cat}^{-1} \cdot h^{-1}$) = ($V_{flow}/W_{cat}$) * 0.06

Space time (s) = (V_{cat}/V_{flow}) * 60, where V_{flow} (mL/min) is the total flow rate of the pristine mixed gas; W_{cat} (g) is the weight of catalyst; V_{cat} (mL) is the volume of catalyst

3.3 Characterizations

3.3.1 In-situ XRD

The crystalline structure of the catalyst was determined using powder X-ray diffraction. The X-ray diffraction patterns were collected using a PANalytical Empyrean System diffractometer with Cu Kα radiation (λ = 0.1542 nm), operating at 45 kV/40 mA, using a nickel Kβ filter and a solid-state detector.

3.3.2 H_2 TPR

H_2 temperature-programmed reduction (TPR) was carried out on a Chemstar instrument. Prior to TPR measurement, 100 mg of the catalyst was flushed with Ar (>99.999%) at 150 °C for 1 h, then cooled to 50 °C. Subsequently, the temperature was increased from 50 to 500 °C with a ramp of 2 $°C \cdot min^{-1}$ under H_2/Ar (volume ratio 1/9, flow rate 30 $mL \cdot min^{-1}$). The temperature was then maintained at 500 °C for a period of 30 min. The H_2 concentration was monitored by means of a thermal conductivity detector (TCD). The H_2-TPR profile was recorded as H_2 consumption versus reduction temperature.

3.3.3 H_2 TPD

The process of H_2 chemisorption on reduced catalysts was carried out using the same instrument of H_2-TPR, namely the Chemstar instrument from Quantachrome instruments company, which is utilized for H_2-TPD. A 0.10 g portion of the Co-based sample was subjected to reduction at a temperature of 310 °C for a duration of 1 h in H_2 flow (>99.999%, 30 $mL \cdot min^{-1}$) and then cooled to 100 °C. Subsequently, the same H_2 flow was maintained at 100 °C for a further hour, with the objective of saturating the surface-active sites. Afterward, Ar was introduced instead of H_2 (>99.999%, 10 $mL \cdot min^{-1}$) for a duration of 30 min, with the objective of eradicating physiosorbed H_2. Subsequently, the temperature was elevated from 100 to 450 °C at a rate of 10 $°C \cdot min^{-1}$ and maintained at 450 °C for a duration of 2 h under Ar flow. The desorbed H_2 was monitored by TCD and used for quantification.

3.3.4 BET

N_2 physisorption experiments were conducted on a Quantachrome Sulfur instrument, a device designed specifically for the measurement of surface area and porosity. The sample was degassed at 310 °C for 1 h, followed by N_2 adsorption at −196 °C. The BET surface area was determined by means of the Brunauer−Emmett−Teller (BET) method.

3.3.5 TEM

The morphology of the CuZr and $CoCuZrO_x$ catalysts was measured on a JEM-1400 plus transmission microscope working at 200 kV in order to assess crystallinity and particle size, respectively.

3.3.6 Atomic absorption spectroscopy

The elemental composition of the samples was determined by atomic absorption spectroscopy in a Unicam M Series Flame-AAS apparatus that was equipped with an FS 95 autosampler and a GF 95 graphite furnace.

3.3.7 SEM

The structural properties of the synthesized catalysts, namely CuZr, $CoCuZrO_x$ and Na-$CoCuZrO_x$ catalysts were analyzed using a scanning electron microscopy (SEM) to assess crystallinity and particle size, respectively. Scanning electron microscopy (SEM) images of the Co-Cu-Zr catalyst confirmed the homogeneous distribution of cobalt, copper and zirconia species over the $CoCuZrO_x$ catalyst.

3.3.8 XPS

The X-ray photoelectron spectroscopy was measured using a Shimadzu AXIS Supra$^+$ X-ray photoelectron spectrometer.

3.3.9 In-situ DRIFTS

In situ FTIR spectra were collected on a Thermofisher Scientific 4700 FTIR spectrometer equipped with a DRIFTS accessory and a high temperature cell (Harrick). Each spectrum was recorded at a resolution of 4 cm^{-1}, with an average of 64 scans, and reported as pseudo-absorbance. The $Cu_2Zr_1O_x$ and $Co_1Cu_1Zr_1O_x$ powders were meticulously placed into the sample holder cup of the high-temperature cell with 1:10 SiO_2 dilution. Prior to the acquisition of spectra at 523 Kelvin, the catalyst sample underwent a reduction in hydrogen at 583 Kelvin for a duration of one hour. Thereafter, the sample was subjected to a cooling process in a hydrogen flow, accompanied by a continuous purging of hydrogen at room temperature for a period time. Subsequently, a background infrared spectrum was recorded at the reaction temperature of 523

Kelvin in hydrogen, with a flow rate of 20 $mL \cdot min^{-1}$ and a pressure of 20 bar. A gas feeding manifold, equipped with electronic mass flow controllers manufactured by Brooks, was utilized to introduce gases with controlled flow rates and compositions. In the transient experiments, gases (20% CO_2, 80% H_2) with a flow rate of 25 $mL \cdot min^{-1}$ were introduced into the cell and switched when necessary. The acquisition of DRIFTS spectra occurred at an interval of approximately 180 seconds.

3.4 Results and discussion

3.4.1 Analysis the active components and stability of $Cu_2Zr_1O_x$, $Cu_2Zr_1O_x$ loaded Co_3O_4 ($Co@Cu_2Zr_1O_x$) and $Co_1Cu_1Zr_1O_x$ series catalysts

The active components and structural stability of catalysts are critical factors governing their performance under varying reaction environments. To elucidate these aspects, coprecipitated $Cu_2Zr_1O_x$, $Co_1Cu_1Zr_1O_x$ and separated coprecipitated $Cu_2Zr_1O_x$ loaded Co_3O_4 ($Co@Cu_2Zr_1O_x$) were systematically investigated for alcohol synthesis. The evolution of the active phases and their redox behavior were examined under different conditions using operando X-ray diffraction (XRD). Specifically, the oxidized (**yellow line**), reduced (**purple line**), and re-oxidized (**green line**) states (**Figure. 3-2 A-C**) were compared to assess the reversibility and structural robustness of each catalyst during the reaction process. The $Cu_2Zr_1O_x$ catalyst was found to be unstable in comparison to the Co loaded CuZr and CoCuZr series catalysts from the observation of the XRD results. The $Cu_2Zr_1O_x$ catalyst is fully reduced to a metallic copper phase, accompanied by a ZrO_2 phase transition from tetragonal (t-ZrO_2) to monoclinic (m-ZrO_2) upon re-oxidation. Furthermore, it has been demonstrated that this transition compromises the instability catalytic performance. A comparison of the activity of the $Cu_2Zr_1O_x$ catalyst and the re-oxidation catalyst reveals that the former exhibits a higher methanol space time yield which is consistent with the promotion of t-ZrO_2 while m-ZrO_2 is less prominent[43] **(Figure. 3-2 A)**. Conversely, catalysts prepared via the separated precipitation method, where $Cu_2Zr_1O_x$ is supported on Co_3O_4, exhibit a marked sharpening of Co_3O_4 and ZrO_2 diffraction peaks following re-oxidation, suggesting sintering and particle growth on the catalyst surface **(Figure. 3-2 B)**. As demonstrated in **Figure. 3-2 C**, the incorporation of Cu significantly reduces the hcp to fcc phase transition temperature of cobalt in the $Co_1Cu_1Zr_1O_x$ catalyst. This phenomenon is attributed to the formation of Co-Cu solid, wherein Cu facilitates Co atom migration and structural rearrangement, thereby stabilizing the more symmetrical fcc-Co phase. In the case of fcc-Co(111), CO* is more readily desorbed into CO with a lower CO*

desorption energy, thus, appearing lower C-O bond cleavage and higher oxygenates selectivity [42].

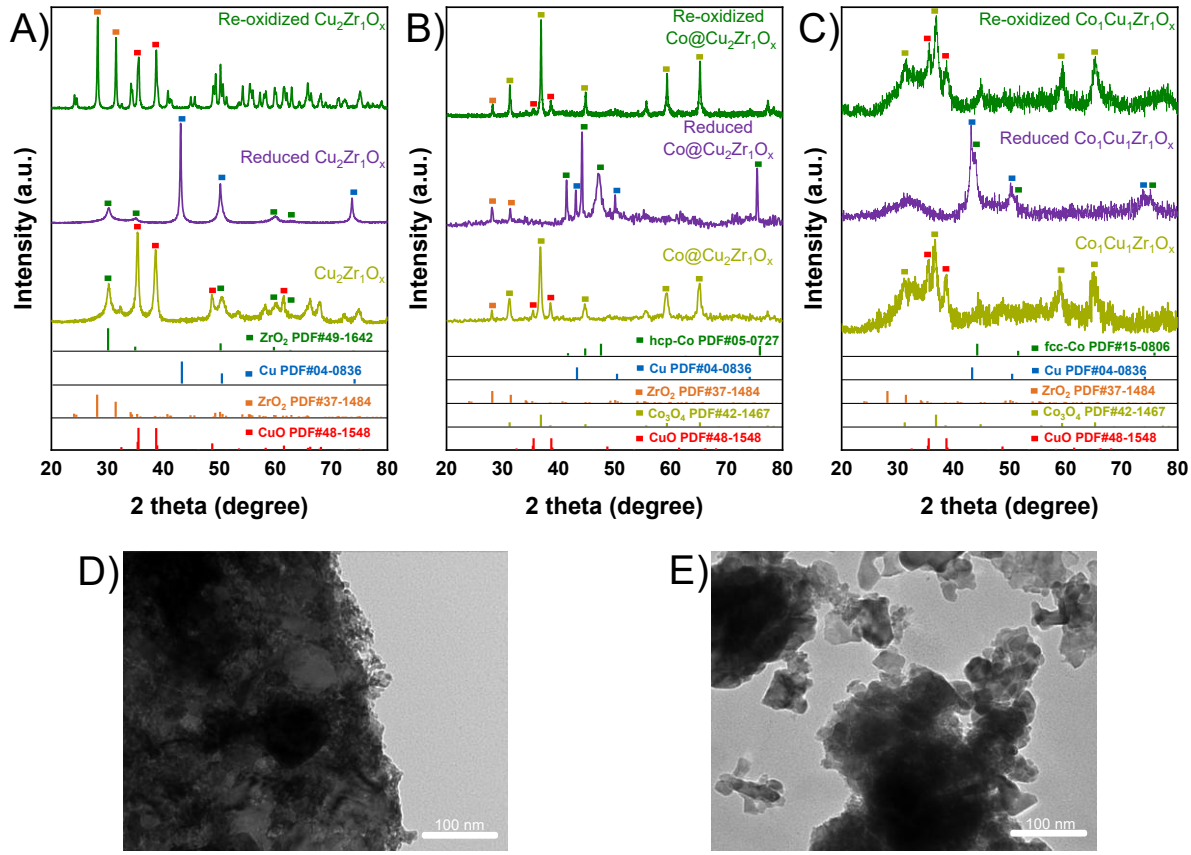

Figure. 3-2. Phase transition analysis of $Cu_2Zr_1O_x$, $Cu_2Zr_1O_x$ loaded Co_3O_4 (Co@$Cu_2Zr_1O_x$) and $Co_1Cu_1Zr_1O_x$ series catalysts.

(**A**-C) The formal, reduced and re-oxidized XRD analysis of $Cu_2Zr_1O_x$, Co@$Cu_2Zr_1O_x$ and $Co_1Cu_1Zr_1O_x$ catalysts.

(D-**E**) The TEM analysis of $Cu_2Zr_1O_x$ and $Co_1Cu_1Zr_1O_x$ catalysts.

The formation of fcc-Co/Cu alloys is particularly advantageous, as these phases exhibit superior hydrogen activation and C-C coupling capabilities compared to pure Co, enhancing catalytic performance for CO_2 hydrogenation towards alcohols and light hydrocarbons. Conversely, the $Cu_2Zr_1O_x$ loaded Co_3O_4 (Co@$Cu_2Zr_1O_x$) system exhibits a predominant retention of hcp-Co, which is less effective for these transformations of the intermediates.

Further corroboration of these structural insights is provided by TEM analysis, which reveals that $Cu_2Zr_1O_x$ forms uniformly small particles, while the $Co_1Cu_1Zr_1O_x$ catalyst exhibits a plate-like, composite morphology where Co, Cu, and ZrO_2 are intimately integrated. This structural configuration is conducive to enhanced interfacial synergy, contributing to the catalyst's improved activity and selectivity in CO_2 hydrogenation (**Figure. 3-2 D-E**). With regard to the SEM results (**Figure S3-7**) of surface structure from $Cu_2Zr_1O_x$, $Co_1Cu_1Zr_1O_x$ to

2wt% Na-$Co_1Cu_1Zr_1O_x$, it is evident that the particle size increases to a greater extent, which may provide a rationale for the observed shift in selectivity from a structural perspective. The precise metals content was analyzed using atomic absorption spectroscopy (AAS), with the precise loading being of paramount importance (**Table S3-1**). Meanwhile, the surface area has the highest value when the ratio of Co:Cu:Zr is 1:1:1, which is approximately 74.15 $m^2 \cdot g^{-1}$, as illustrated in **Figure S3-8** and substantiated in **Table S3-4**.

3.4.2 Comparison of the activity of coprecipitated Cu-Zr, re-oxidized Cu-Zr, Na doped Cu-Zr and reference Cu-Zr series catalysts

The Cu-Zr catalyst series was employed as a platform for methanol production, taking advantage of the well-known synergy between Cu active sites and ZrO_2 supports. However, upon re-oxidation, the Cu-Zr catalyst underwent a noticeable transformation in the ZrO_2 crystal phase, reflecting a structural instability of the support in an oxidative environment. This phase transition has been shown to disrupt the interfacial Cu-Zr synergy that is essential for stabilizing CH_xO intermediates from the change of methanol production (**Figure 3-3 Left**). As shown in **Figure. 3-3**, $Cu_2Zr_1O_x$ catalysts demonstrate outstanding performance in methanol synthesis when DBU is used as the precipitation agent without alkali metals containment. The space time yield of methanol is far beyond the re-oxidized Cu-Zr, Na loaded Cu-Zr and references Cu-Zr catalysts by using precipitation-impregnation method and different precipitation agents under optimized parameters. The superior catalytic performance of $Cu_2Zr_1O_x$ is comparable to that of a well-known reference catalyst for methanol synthesis (ZrO_2/Cu-0.1) [11].

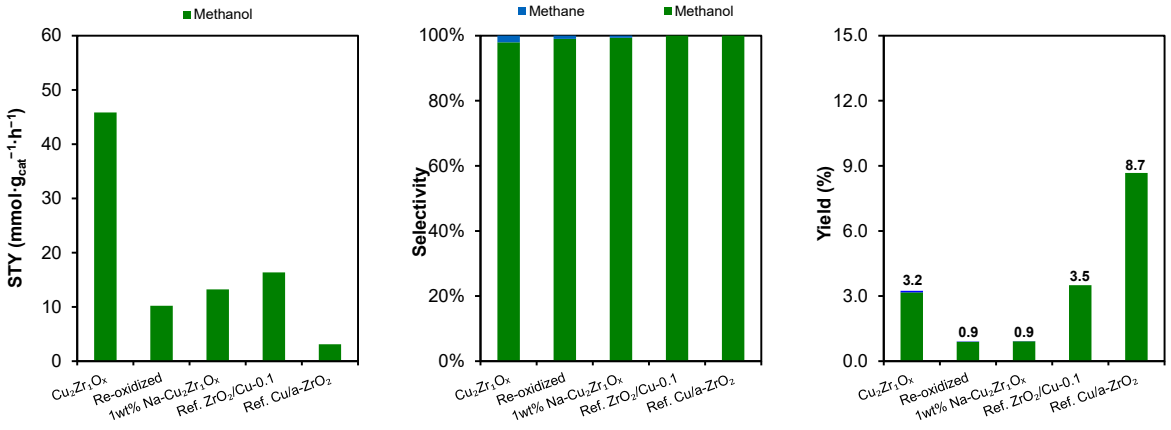

Figure 3-3. (**Left**) Methanol space time yield (STY) for comparing the $Cu_2Zr_1O_x$ catalysts, Na loadings and reference catalysts. (**Center**) Catalytic performance for comparing the $Cu_2Zr_1O_x$ catalysts, Na loadings and reference catalysts. (**Right**) Catalytic yield for comparing the $Cu_2Zr_1O_x$ catalysts, Na loadings and reference catalysts. All the experiments are regarded as CO free and analyzed at 300°C, 5.0 MPa, space velocity = 150 $L \cdot g_{cat}^{-1} \cdot h^{-1}$, $H_2/CO_2 = 4$.

3.4.3 Comparison of the activity of the different composition of $Cu_yZr_1O_x$ series catalysts

To further analyze the Cu-Zr catalyst, the composition of $Cu_yZr_1O_x$ was examined. The interplay between Cu and Zr influences the balance between CO and methanol intermediates, where Cu facilitates CO_2 activation and C-O cleavage, while enhancing hydrogenation toward methanol. ZrO_2 acts as a structural and electronic promoter, improving metal dispersion, providing oxygen vacancies, and tuning the electronic environment of active sites. Therefore, an optimal Cu:Zr ratio is essential for maximizing methanol production, whereas excessive Cu favors methanol selectivity. Additionally, the ZrO_2 content significantly affects catalyst reducibility and stability, thereby influencing alcohol distribution.

Prior to the reaction, the pristine $Cu_yZr_1O_x$ catalysts were reduced using 30% H_2 at 310 °C for 0.5 h. During the catalytic reaction, the CO_2 conversion of the catalysts was kept below 5% to stay away from the equilibrium methanol concentration and approach the intrinsic activity. Of all the catalysts with different Zr/Cu ratio, the $Cu_2Zr_1O_x$ catalyst exhibited the highest space time yield (STY) of methanol at a rate of 45 $mmol \cdot g_{cat}^{-1} \cdot h^{-1}$ higher than that of the $Cu_1Zr_1O_x$ and $Cu_3Zr_1O_x$ catalysts (**Figure 3-4**). For the $Cu_yZr_1O_x$ composition, the increasing of the CuO loading triggered a volcano-like effect in the methanol formation rate. Therefore, it can be concluded that combining ZrO_2 and Cu with a suitable Zr/Cu ratio is crucial for constructing an excellent catalyst for methanol synthesis from CO_2. In the rest of the paper, the term of Cu-Zr catalyst refers to the main component that produces high quantity of CH_xO intermediate necessary for forming the ethanol product.

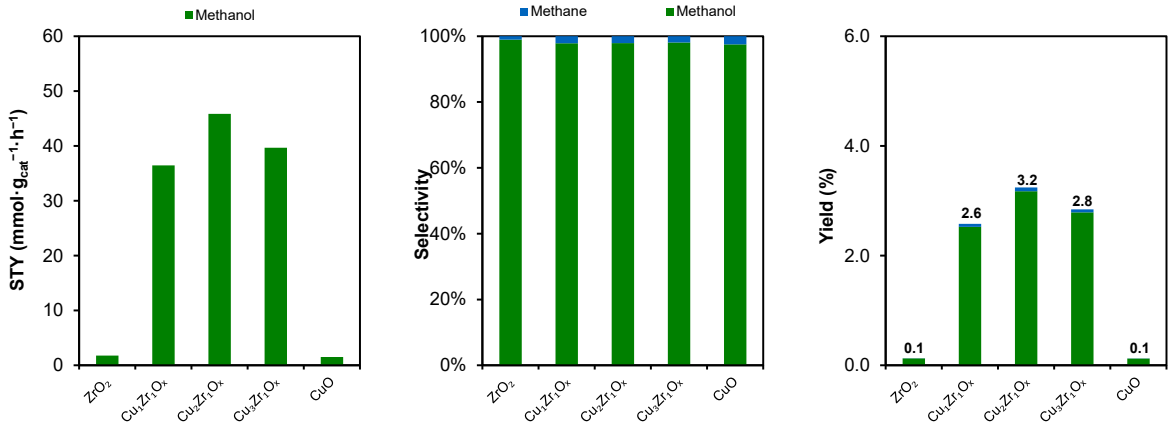

Figure 3-4. (**Left**) Methanol space time yield (STY) for adjusted Cu/Zr ratio on $Cu_yZr_1O_x$ catalysts. (**Center**) Catalytic performance for adjusted Cu/Zr ratio on $Cu_yZr_1O_x$ catalysts. (**Right**) Catalytic yield for adjusted Cu/Zr ratio on $Cu_yZr_1O_x$ catalysts. All the experiments are regarded as CO free and analyzed at 300°C, 5.0 MPa, space velocity = 150 $L \cdot g_{cat}^{-1} \cdot h^{-1}$, $H_2/CO_2 = 4$.

3.4.4 Combining Co catalyst and Cu-Zr catalyst to reach high alcohols

Despite achieving a higher methanol selectivity of approximately 100% with CO free, the Cu-Zr catalyst demonstrated poor ethanol selectivity and predominantly formed methanol. In order to evaluate the role of Co in the $Co_xCu_yZr_1O_z$ system, the performance of a series of different Co-Cu-Zr catalysts was compared (**Figure 3-5**). The Co-Cu, Co-Cu-Zr, Co@$Cu_2Zr_1O_x$ and $Cu_2Zr_1O_x$@Co catalysts exhibited ethanol production, whereas the Co-Cu and $Cu_2Zr_1O_x$@Co catalysts exhibited an extremely low space time yield of ethanol.

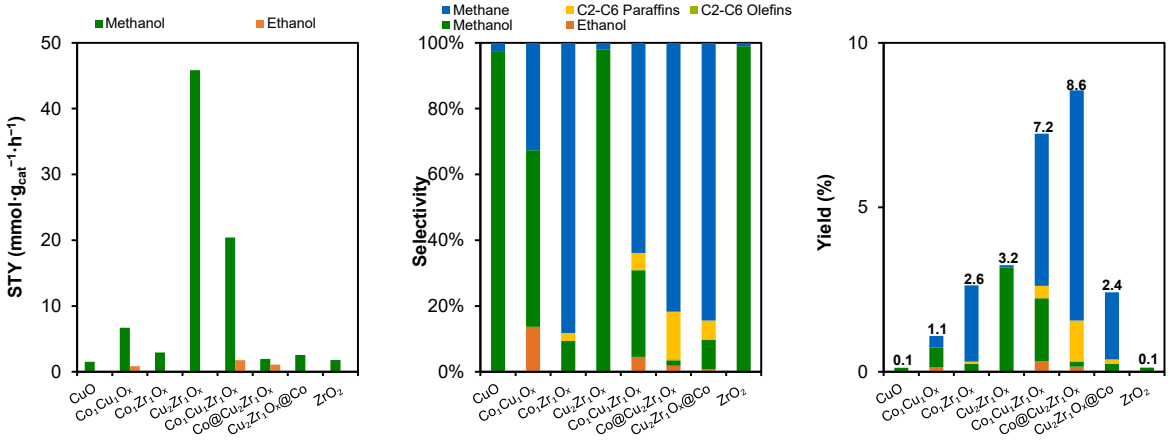

Figure 3-5. (**Left**) Methanol space time yield (STY) for CuO, Co-Cu, Co-Zr, Cu-Zr, Co-Cu-Zr, Co@$Cu_2Zr_1O_x$, $Cu_2Zr_1O_x$@Co and ZrO_2 series catalysts. (**Center**) Catalytic performance CuO, Co-Cu, Co-Zr, Cu-Zr, Co-Cu-Zr, Co@$Cu_2Zr_1O_x$, $Cu_2Zr_1O_x$@Co and ZrO_2 series catalysts. (**Right**) Catalytic yield for CuO, Co-Cu, Co-Zr, Cu-Zr, Co-Cu-Zr, Co@$Cu_2Zr_1O_x$, $Cu_2Zr_1O_x$@Co and ZrO_2 series catalysts. All the experiments are regarded as CO free and analyzed at 300°C, 5.0 MPa, space velocity = 150 $L \cdot g_{cat}^{-1} \cdot h^{-1}$, $H_2/CO_2 = 4$.

In consideration of the CO_2 conversion, products selectivity and ethanol space time yield, the Co@$Cu_2Zr_1O_x$ and Co-Cu-Zr catalysts demonstrate a significantly higher ethanol space time yield. Consequently, these two catalysts were selected for further development and optimization.

3.4.5 Comparison of the activity of different Co-loaded $Cu_2Zr_1O_x$ series catalysts

Catalysts containing $Cu_2Zr_1O_x$ loaded on Co_3O_4 (Co@$Cu_2Zr_1O_x$) were synthesized by using $Cu_2Zr_1O_x$ as the precursor, followed by the precipitation of a cobalt nitrate solution using a DBU agent. The outcomes of modifying the quantity of $Cu_2Zr_1O_x$ loaded on Co_3O_4 demonstrate a volcano-shaped ethanol product curve, with a maximum space time yield of approximately 1.1 $mmol \cdot g_{cat}^{-1} \cdot h^{-1}$ by using 0.84wt% $Cu_2Zr_1O_x$ loaded on Co_3O_4 catalyst (**Figure 3-6**).

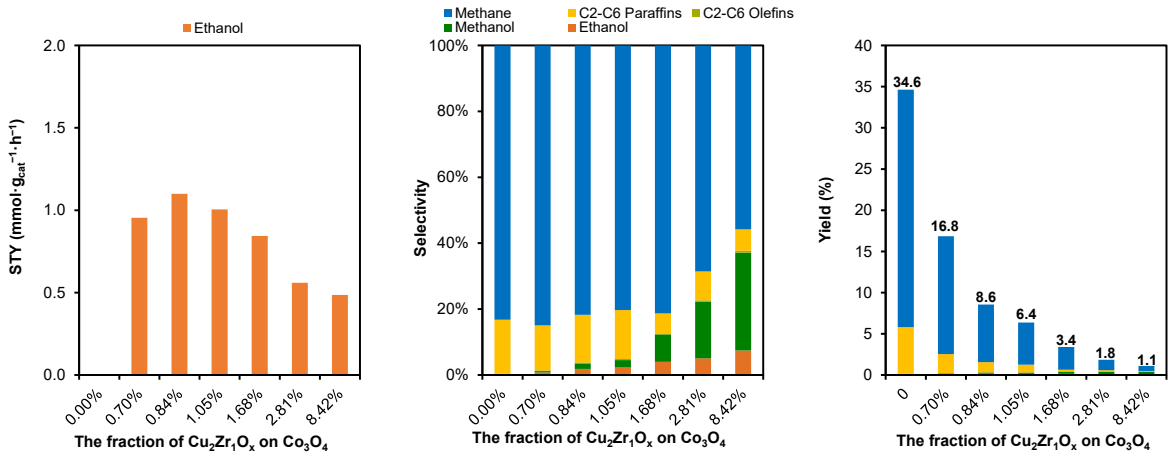

Figure 3-6. (**Left**) Ethanol space time yield (STY) and catalytic performance for adjusted $Cu_2Zr_1O_x$ loadings on Co_3O_4 catalysts. (**Center**) Catalytic performance for adjusted $Cu_2Zr_1O_x$ loadings on Co_3O_4 catalysts. (**Right**) Catalytic yield for adjusted $Cu_2Zr_1O_x$ loadings on Co_3O_4 catalysts. All the experiments are regarded as CO free and analyzed at 300°C, 5.0 MPa, space velocity = 150 $L \cdot g_{cat}^{-1} \cdot h^{-1}$, $H_2/CO_2 = 4$.

3.4.6 Comparison of the activity of different coprecipitated $Co_xCu_yZr_1O_z$ series catalysts

In order to facilitate comparison with the coprecipitation method, the $Co_xCu_yZr_1O_z$ precursor was prepared by means of a coprecipitation method with the constant active sites that x+y=2. It is evident that an increase in the Co molar ratio results in a decline in the space time yield (STY) of methanol, while the space time yield (STY) of ethanol exhibits a volcano like trend. These comparisons suggest that cobalt enhances C-O cracking and C-C coupling, a crucial step in ethanol formation, while Cu-Zr is effective for a comparable weak C-O bond cleavage, which favors methanol formation. The combination of these functionalities in the Co-Cu-Zr system has been shown to result in a significant enhancement of the overall selectivity for ethanol is significantly improved to 4.5% with CO free (**Figure 3-7**).

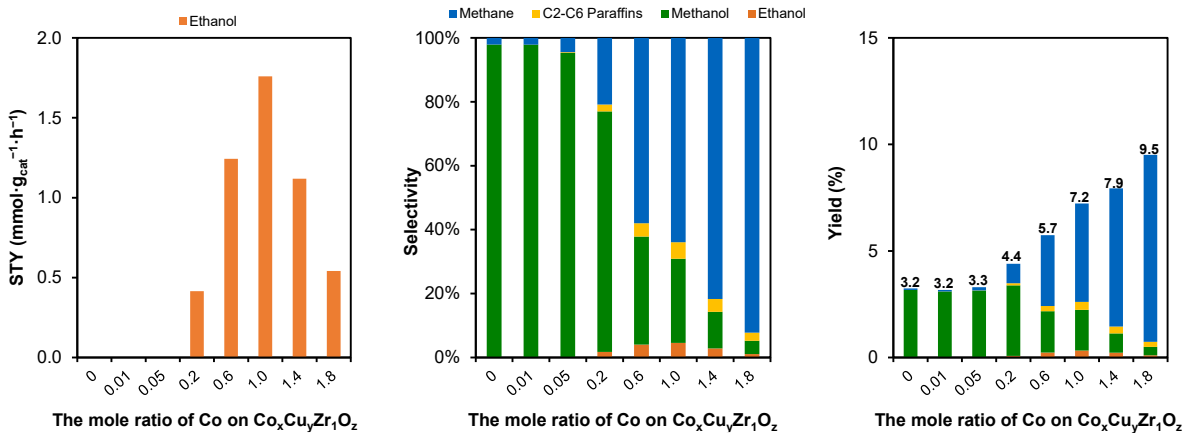

Figure 3-7. (**Left**) Ethanol space time yield (STY) and catalytic performance for adjusted Co and Cu loadings on $Co_xCu_yZr_1O_z$ catalysts. (**Center**) Catalytic performance on $Co_xCu_yZr_1O_z$ catalysts. (**Right**) Catalytic yield for $Co_xCu_yZr_1O_z$ catalysts. All the experiments are regarded as CO free and analyzed at 300°C, 5.0 MPa, space velocity = 150 $L \cdot g_{cat}^{-1} \cdot h^{-1}$, $H_2/CO_2 = 4$. x+y =2.

The Cu-Zr has been shown to facilitate the initial C-O bond cleavage in CO_2, forming CH_xO intermediates that are crucial for C_1 product formation. The presence of cobalt has been shown to promote C-C coupling between CH_x and CH_xO species, thereby increasing the selectivity for C_2+ alcohols such as ethanol. The amalgamation of these functionalities within Co-Cu-Zr system engenders a conducive reaction environment that enhances the production of ethanol production whilst concomitantly suppressing undesired byproducts. As the Co/Cu ratio increases, the selectivity for methanol appears to decline, while the selectivity for methane exhibits an increase. For ethanol, the maximum is attained at a Co/Cu/Zr ratio of 1:1:1. In contrast, the space time yield of ethanol with the $Co_1Cu_1Zr_1O_x$ catalyst is 1.76 $mmol \cdot g_{cat}^{-1} \cdot h^{-1}$, which is evidently greater than the 0.84wt% $Cu_2Zr_1O_x$ loaded on Co_3O_4 catalyst.

3.4.7 Optimizing the promoters and parameters to increase ethanol STY

The present study employed a range of techniques including $Co_1Cu_1Zr_1O_x$ catalyst, alkali metal promoters, pressure change, and space time analysis with a view to enhancing the space time yield and selectivity of ethanol. The incorporation of alkali metal promoters has been shown to have a significant influence on the formation of alcohols in the process of CO_2 hydrogenation, by modifying the electronic properties, adsorption behavior, and reaction pathways of the catalyst. Alkali metals have been demonstrated to influence CO_2 activation by adjusting electron density on active sites, thereby facilitating CO_2 dissociation and stabilizing key intermediates, including *CO and *CH_x species. Moreover, alkali metal has been shown to weaken CO adsorption, thereby reducing CO formation and favoring C-C coupling, which is crucial for higher alcohols synthesis. The basicity introduced by alkali metals has also been demonstrated to alter hydrogenation kinetics, thereby shifting selectivity from methanol to C_2+ alcohols. However, it has been demonstrated that excessive alkali loading can reduce catalyst reducibility and lead to over-poisoning of active sites, thereby diminishing catalytic activity. Therefore, the judicious selection and optimization of alkali metal concentration is imperative to maximizing alcohol yield and selectivity in CO_2 hydrogenation.

The catalytic performance of the synthesized 1-3 wt% Na-$Co_1Cu_1Zr_1O_x$ catalyst was evaluated for the hydrogenation of CO_2 to ethanol. The 2 wt% Na-$Co_1Cu_1Zr_1O_x$ catalyst demonstrated the highest space time yield (STY) of ethanol at a rate of 2.22 $mmol \cdot g_{cat}^{-1} \cdot h^{-1}$,

accompanied by a selectivity of 9.3%, which is notably higher than that of the $Co_1Cu_1Zr_1O_x$ catalyst (1.76 mmol·g_{cat}^{-1}·h^{-1}). With regard to the 3 wt% Na-$Co_1Cu_1Zr_1O_x$ catalyst, it has been demonstrated that it is capable of achieving a selectivity of 14.0% for ethanol, although this is accompanied by a comparatively low space time yield of approximately 1.85 mmol·g_{cat}^{-1}·h^{-1} (**Figure 3-8**).

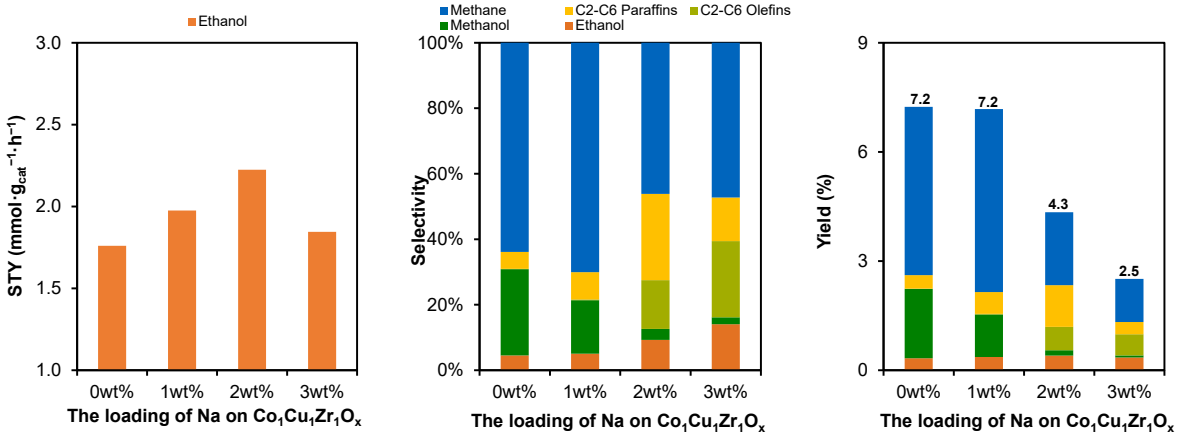

Figure 3-8. (**Left**) Ethanol space time yield (STY) and catalytic performance for adjusted Na loading catalysts. (**Center**) Catalytic performance on x wt% Na-$Co_1Cu_1Zr_1O_x$ catalysts. (**Right**) Catalytic yield for x wt% Na-$Co_1Cu_1Zr_1O_x$ catalysts. All the experiments are regarded as CO free and analyzed at 300°C, 5.0 MPa, space velocity = 150 L·g_{cat}^{-1}·h^{-1}, H_2/CO_2 = 4.

The 2wt% Na-$Co_1Cu_1Zr_1$Ox catalyst demonstrated superior catalytic performance in terms of ethanol selectivity and yield in comparison to the $Co_1Cu_1Zr_1O_x$ catalysts. Conversely, the $Co_1Cu_1Zr_1O_x$ catalyst predominantly produced methane and methanol, accompanied by minimal C_2+ product formation. The results obtained demonstrate the synergistic effect of Na and $Co_1Cu_1Zr_1O_x$ in promoting ethanol formation while suppressing methane and methanol production, with a similar active site dispersion (**Table S3-2**).

The concentration of products or reactants has been shown to influence the forward and reverse reactions. Consequently, pressure is a significant factor in adjusting the distribution of products. As the pressure increases, the total CO_2 conversion rate rises concomitantly with heightened activity in all the FTS and formate pathways in comparison to the RWGS. As the pressure increased, the space time yield (STY) of alcohol increased concomitantly. The highest space time yield (STY), C_2+ selectivity and CO_2 conversion were at 50 bar (**Figure 3-9**). At a pressure of 10 bar, the CO_2 conversion was recorded at 1.7%, with CO free and an ethanol yield of 9.6% being achieved. As the pressure increased to 50 bar, both conversion (4.3%) and ethanol

yield (2.22 mmol·g_{cat}^{-1}·h^{-1}) reached their highest values, indicating an optimal interaction between CO_2, hydrogen, and intermediates on the surface of the catalyst.

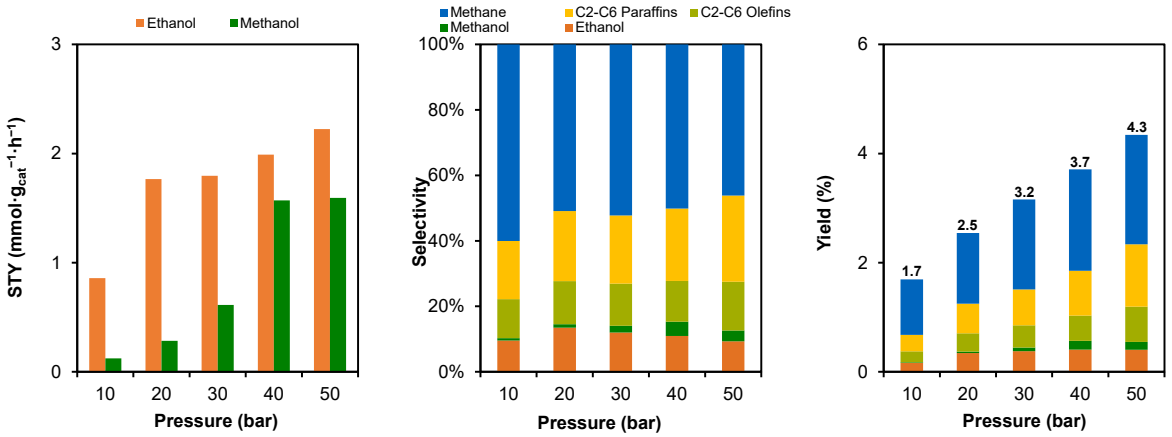

Figure 3-9. (**Left**) Alcohols space time yield (STY) and catalytic performance for different pressure. (**Center**) Catalytic performance on 2 wt% Na-$Co_1Cu_1Zr_1O_x$ with pressure shift. (**Right**) Catalytic yield for 2 wt% Na-$Co_1Cu_1Zr_1O_x$ with pressure shift. All the experiments are regarded as CO free and analyzed at 300°C, 1.0-5.0 MPa, space velocity = 150 L·g_{cat}^{-1}·h^{-1}, $H_2/CO_2 = 4$.

In order to enhance the space time yield of ethanol, it is imperative to manipulate the residence time of the reactant, as this is instrumental in regulating the binding of intermediates. The residence duration of reactants within the catalyst bed is defined as space time, and it is a fundamental parameter that critically influences CO_2 conversion and product distribution in hydrogenation systems. In the case of low space time, the restricted contact between reactants and the catalytic surface serves to limit the extent of reaction, thus favoring kinetically accessible pathways such as the reverse water gas shift (RWGS) and partial hydrogenation. Consequently, the CH_xO intermediate has a greater capacity to combine with the CH_x intermediate, without undergoing additional C-O cleavage to reach the CH_x intermediate. Conversely, an increase in space time provides enhanced opportunities for surface bound intermediates to undergo further transformation of CH_xO to CH_x. The process under discussion has been shown to promote sequential hydrogenation and C-C coupling reactions, thereby enabling the formation of longer-chain hydrocarbons. The extended residence time has been shown to enhance the probability of multistep surface chemistry, a process which is essential for driving product complexity beyond simple C_1 compounds. A reduction in the space time is a pivotal approach for diminishing the functionality of the FTS process and augmenting the formate pathway in Co-based catalyst. As demonstrated in **Figure 3-10**, the graph indicates that the maximum space time yield (STY) of ethanol is approximately 3.8 mmol·g_{cat}^{-1}·h^{-1}, which

significantly exceeds the established benchmark for a Co-based catalyst and the selectivity of ethanol is estimated to be approximately 15.1 % with a space time of 0.01 s. Concurrently, the selectivity of C_2+ products attains approximately 60% with an optimized low space time. The results indicate that the lower space time is associated with the lower CO_2 conversion, thereby demonstrating higher alcohols (methanol and ethanol) space time yield by the inadequate C-H bond hydrogenation and C-O bond cleavage of the CH_xO intermediate. It can be further confirmed from **Figure S3-10**, which shows almost constant olefins, methanol and ethanol yield with the decrease of C_2-C_6 paraffins and olefins yield in the yield vs. conversion changes, which represents a higher selectivity and space time yield when established a lower CO_2 conversion.

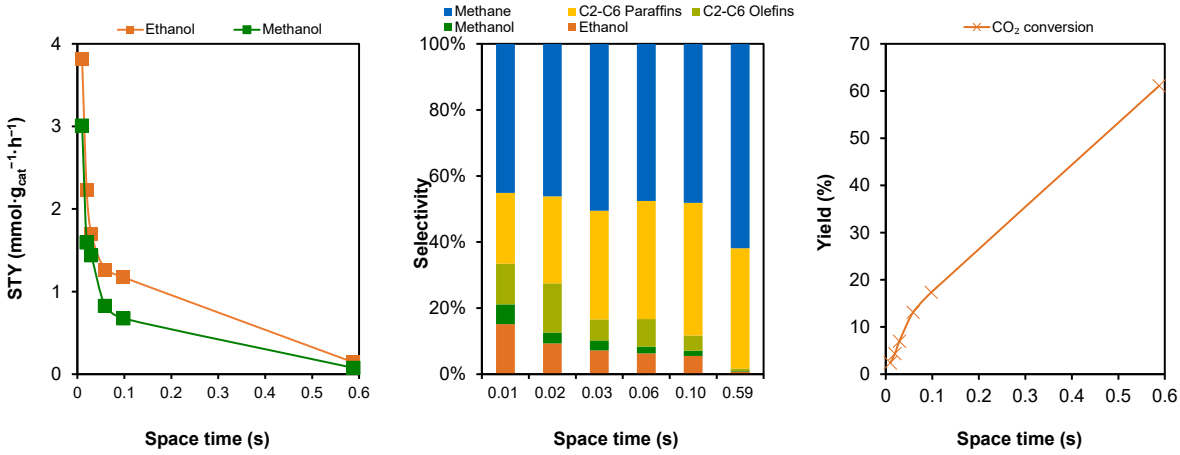

Figure 3-10. (**Left**) Alcohols space time yield (STY) and catalytic performance for adjusted space time. (**Center**) Catalytic performance on 2 wt% Na-$Co_1Cu_1Zr_1O_x$ with space time shift. (**Right**) Catalytic yield for 2 wt% Na-$Co_1Cu_1Zr_1O_x$ with space time shift. All the experiments are regarded as CO free and analyzed at 300°C, 5.0 MPa, space time = 0.01-0.59 s, H_2/CO_2 = 4.

3.4.8 Reaction stability and kinetics analysis for promoting ethanol STY by alkali promoters

The present study investigates the stability of the activated 2 wt% Na-$Co_1Cu_1Zr_1O_x$ catalyst was evaluated under industrially relevant conditions of 50 bar with an H_2/CO_2 ratio of 4:1, a space velocity of 300 $L\cdot g_{cat}^{-1}\cdot h^{-1}$ at 300 °C (**Figure 3-11**). Following a period of over 100 h of operation, the catalyst exhibited a consistent product distribution, with a constant selectivity toward alcohols and paraffins. Furthermore, the space time yield (STY) of ethanol sustained at approximately 4 $mmol\cdot g_{cat}^{-1}\cdot h^{-1}$. In the context of lower space velocity conditions for 150 $L\cdot g_{cat}^{-1}\cdot h^{-1}$, it was observed that all product distributions remained consistent over a duration of 92 h (**Figure S3-11**). The results obtained demonstrate that the 2 wt% Na-

$Co_1Cu_1Zr_1O_x$ catalyst is effective in ensuring both long-term durability and consistent ethanol productivity under elevated pressure CO_2 hydrogenation.

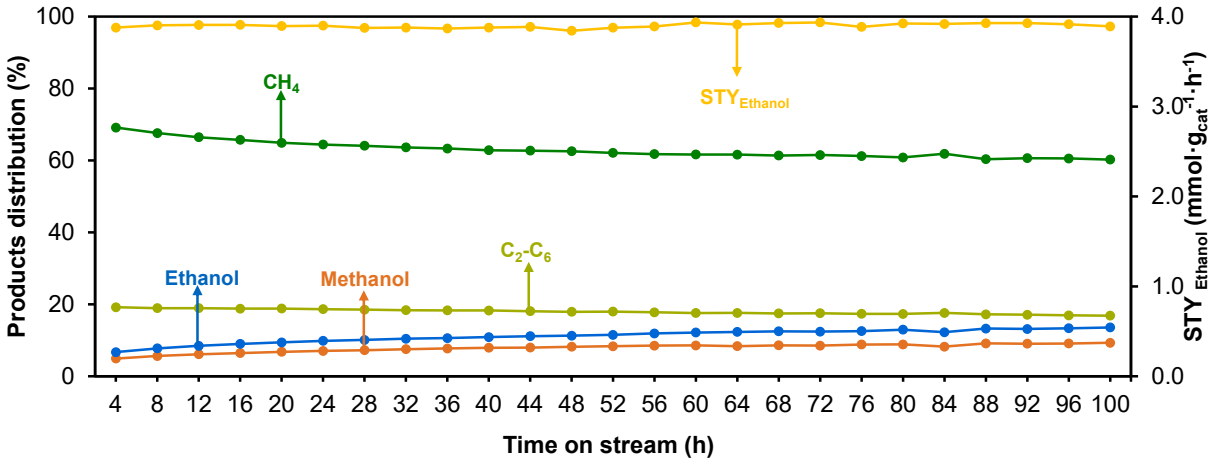

Figure 3-11. The stability of ethanol STY and selectivity of the products (methane, methanol, ethanol and C_2-C_6 paraffins HCs) of 2 wt% Na-$Co_1Cu_1Zr_1O_x$. All the experiments are regarded as CO free and analyzed at 300°C, 5.0 MPa, space velocity = 300 $L \cdot g_{cat}^{-1} \cdot h^{-1}$, $H_2/CO_2 = 4$.

It is evident that the apparent reaction orders on $Co_1Cu_1Zr_1O_x$ (H_2 $\alpha = 0.51$ and H_2 $\beta = 0.17$) and 2wt% Na-$Co_1Cu_1Zr_1O_x$ (H_2 $\alpha = 0.37$ and CO_2 $\beta = 0.11$) provide further evidence that the impede of hydrogenation of alkali metal on 2wt% Na-$Co_1Cu_1Zr_1O_x$ is indeed valid (**Figure 3-12**).

The H_2 to CO_2 feed ratio has a direct influence on the hydrogenation steps and the product distribution in CO_2 reduction. Experiments were conducted with varying H_2/CO_2 ratios (4:1~1:4) of $Co_1Cu_1Zr_1O_x$ and 2wt% Na-$Co_1Cu_1Zr_1O_x$ catalysts at 300°C and 50 bar. A comparison of the two catalysts reveals a decline in CO_2 conversion from 4.0% to 2.1%, accompanied by an increase in the ethanol yield from 0.50 to 1.72 $mmol \cdot g_{cat}^{-1} \cdot h^{-1}$ at the H_2/CO_2 ratio of 1:1. The limited availability of hydrogen has been demonstrated to reduce the efficiency of hydrogenation steps, leading to incomplete reduction of CO_2 and favoring CO formation. The increase in the H_2/CO_2 ratio to 4:1 resulted in the highest ethanol yield (1.76 to 2.22 $mmol \cdot g_{cat}^{-1} \cdot h^{-1}$) and a CO_2 conversion of 7.2% to 4.3%, indicating that an excess of hydrogen promotes the full hydrogenation of CH_xO intermediates to ethanol without excessive over-hydrogenation (**Figure S3-1, S3-2 and S3-4, S3-5**). The Na-doped $Co_1Cu_1Zr_1O_x$ catalyst has been shown to exhibit an enhanced ability to adsorb and activate both CO_2 and H_2, thereby reducing the dependence of the reaction rate on reactant concentration and lowering the apparent reaction order. This shift indicates a fundamental alteration in the reaction mechanism, where the activation of CO_2 and H_2 ceases to be the primary kinetic constraint. Rather, the

apparent rate determining step is mitigated or energetically facilitated, giving rise to a more efficient and selective catalytic pathway.

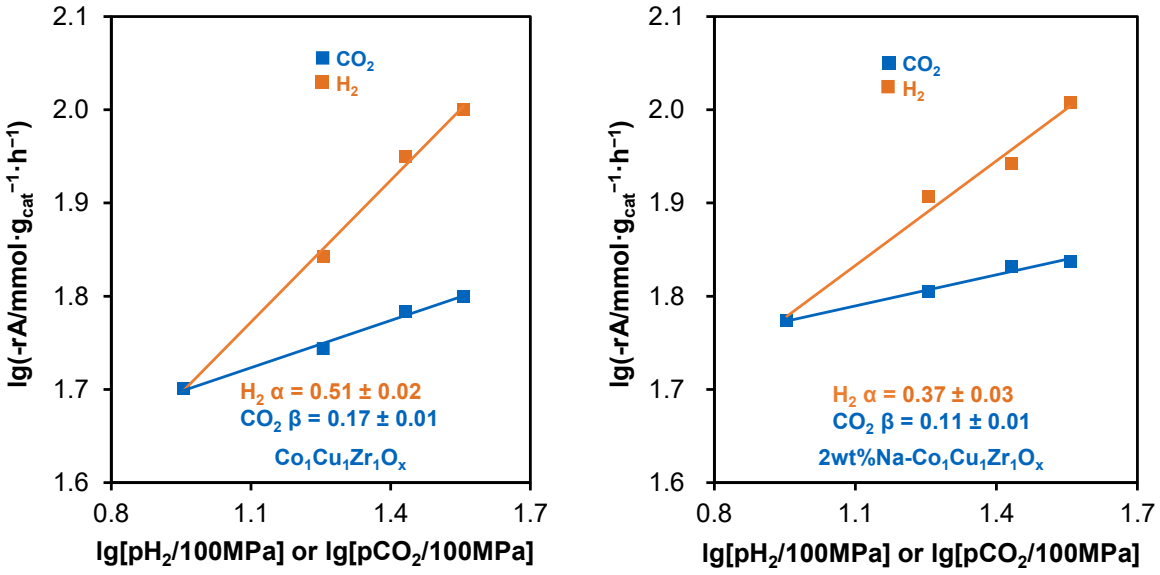

Figure 3-12. (**Left**) CO_2 and H_2 overall reaction orders for $Co_1Cu_1Zr_1O_x$ catalyst. (**Right**) CO_2 and H_2 overall reaction orders for 2 wt% Na-$Co_1Cu_1Zr_1O_x$ catalyst. All the experiments are analyzed at 300°C, 5.0 MPa, space velocity = 150 $L \cdot g_{cat}^{-1} \cdot h^{-1}$, H_2/CO_2 = 1/4-4/1. A: the total conversion of CO_2.

Temperature is a pivotal factor in regulating the kinetic rates of both intermediate formation and subsequent hydrogenation steps, which can be quantitatively assessed through the apparent activation energy (Ea). The calculated Ea values (**Figure 3-13**) demonstrate that the formation of CH_4 and C_2H_5OH on $Co_1Cu_1Zr_1O_x$ requires 81 $kJ \cdot mol^{-1}$ and 59 $kJ \cdot mol^{-1}$, respectively. Conversely, in the 2 wt% Na-$Co_1Cu_1Zr_1O_x$ sample, the Ea increases to 96 kJ mol^{-1} for CH_4 but decreases to 45 $kJ \cdot mol^{-1}$ for ethanol. This shift unequivocally signifies that Na incorporation exerts a suppressive effect on the energetics of over-hydrogenation towards CH_4, whilst concomitantly reducing the kinetic barrier for ethanol synthesis. Consequently, the C-C coupling and alcohol pathway are thermodynamically favored, whereas methane formation is selectively disfavored, accounting for the improved C_2+ oxygenate selectivity observed on the Na-modified catalyst.

For the $Co_1Cu_1Zr_1O_x$ catalyst, methanol is the predominant alcohol product, with a CO_2 conversion of 0.9% at 210°C. The yield towards ethanol was found to be 0.14 $mmol \cdot g_{cat}^{-1} \cdot h^{-1}$, likely due to the insufficient apparent activation energy for effective C-C coupling between CH_x and CH_xO intermediates. As the temperature increased to 300°C, ethanol yield reached its peak at 1.76 $mmol \cdot g_{cat}^{-1} \cdot h^{-1}$, with a CO_2 conversion of 7.2% (**Figure S3-3 and S3-6**). The TOF

results (**Table S3-3**) demonstrate an optimal temperature range within which catalytic performance is optimized. In the presence of a Na doped catalyst, a substantially elevated ethanol space-time yield is observed, reaching approximately 2.22 mmol$\cdot g_{cat}^{-1} \cdot h^{-1}$, accompanied by a CO_2 conversion of 4.3% at a temperature of 300°C. It was determined that the balance between C-O bond cleavage on Cu-Zr and C-C coupling on Co sites and Na promoted was more favorable for ethanol production at this optimal temperature.

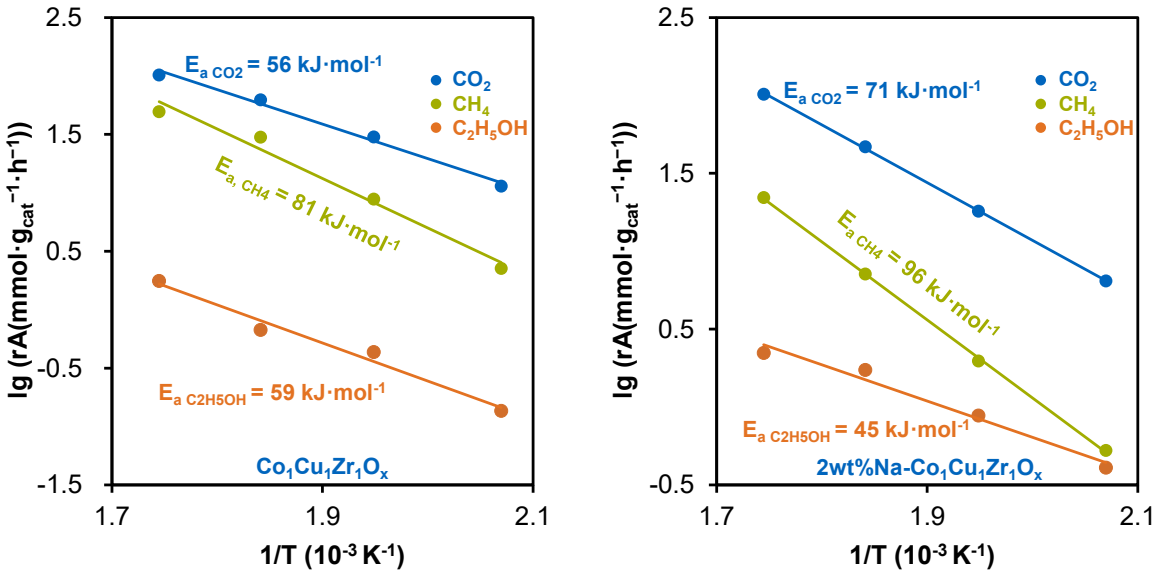

Figure 3-13. (**Left**) Apparent activation energies for overall CO_2, CH_4 and C_2H_5OH formation on $Co_1Cu_1Zr_1O_x$. (**Right**) Apparent activation energies for overall CO_2, CH_4 and C_2H_5OH formation on 2 wt% Na-$Co_1Cu_1Zr_1O_x$. All the experiments are analyzed at 210-300°C, 5.0 MPa, space velocity = 150 L$\cdot g_{cat}^{-1} \cdot h^{-1}$, H_2/CO_2 = 4:1.

3.4.9 The intermediate analysis of the alkali promoted and blank catalysts

It is evident that the intermediates ratio of CH_x/CH_xO is the primary factor that exerts influence on the quantity of ethanol produced, in accordance with the mechanism of CO_2 hydrogenation. In order to analyze the differences of intermediates, the catalysts subsequently conducted in situ diffuse reflectance infrared Fourier transform spectroscopy (DRIFTS) experiments to probe the formation and evolution of surface intermediates involved in the hydrogen-assisted synthesis (HAS) reaction. The role of cobalt in modulating intermediate species was systematically examined, as demonstrated in **Figures 3-14 Left** and **3-14 Right**.

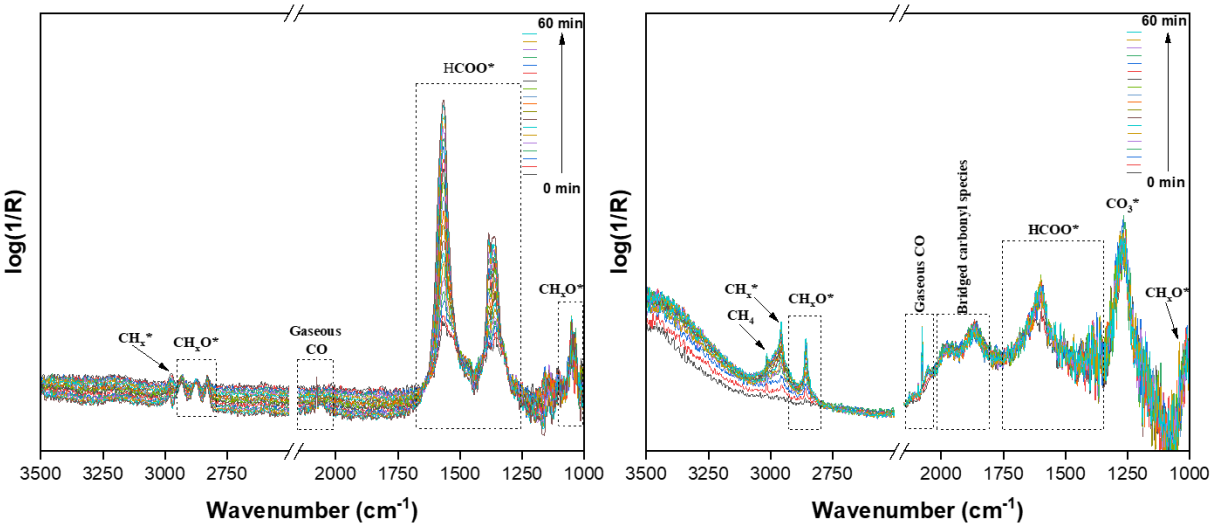

Figure 3-14. In situ DRIFTS spectra of the $CO_2 + H_2$ reaction over the $Cu_2Zr_1O_x$ and $Co_1Cu_1Zr_1O_x$ samples. (**Left**) dynamic spectra at the region of 1000-3500 cm^{-1} of $Cu_2Zr_1O_x$ and (**Right**) dynamic spectra at the region of 1000-3500 cm^{-1} of $Co_1Cu_1Zr_1O_x$ under the reaction conditions of 2 MPa, $H_2/CO_2 = 4$ and 523 K.

Distinct vibrational bands corresponding to CH_4, *CH_x, *CH_xO and *HCOO, gaseous CO, adsorbed CO and *CO_3 species were observed, indicating their participation in C-C coupling pathways leading to ethanol formation. As illustrated in **Table S3-5**, time-resolved DRIFTS spectra recorded at 250 °C revealed the progressive intensification of bands attributed to CH_4, *CH_x, *CH_xO and *HCOO, gaseous CO, adsorbed CO and *CO_3 with increasing reaction time, thereby supporting a CO mediated mechanism. The peaks at 1800-1900 and 1900-2000 cm^{-1} for bridged carbonyl species CO* and the 2176, 2110, and 2085 cm^{-1} of gaseous CO represent the surface adsorption of CO and different forms of existence. Concurrently, the formation of gaseous CH_4 (3015, 1303 cm^{-1}) was detected in the presence of metallic cobalt, suggesting its role in facilitating the hydrogenation of intermediates. It is proposed that cobalt enhances the probability of *CH_x species (2966 cm^{-1}) coupling with *CH_xO (1070-1082, 2824-2826, 2937-2941, 1270 and 1034 cm^{-1}) or *HCOO (1337-1393, 1593-1622 cm^{-1}) intermediates, which are subsequently hydrogenated to ethanol, highlighting the critical function of cobalt in steering the reaction selectivity toward C_2+ oxygenates. The observation of surface carbonate *CO_3 species (1274 cm^{-1}) species in DRIFTS indicates that CO_2 is initially adsorbed and activated through interaction with surface oxygen sites, forming carbonate intermediates. These species can subsequently evolve into bicarbonate or formate intermediates under hydrogenation conditions, suggesting that CO_2 reduction proceeds via surface oxygen-assisted activation rather than direct dissociative adsorption and representing the precursor of *HCOO species. The decline of *HCOO species and the emergence of *CO_3 species suggest that the methanol pathway is hindered and the *CH_x and *CH_xO are promoted to form C_2+ oxygenates.

3.4.10 The valence analysis of the alkali promoted and blank catalysts

The valence influence is the fundamental theory for detecting the change of CH_x/CH_xO, thus necessitating the use of XPS to elucidate the discrepancy between the two catalysts. The XPS results (**Figure 3-15**) indicate that the Na^+ replacement of Co^{3+}, Cu^{2+} and Zr^{4+} species, which in turn influences the valence, adsorption/activation of reactants and intermediates at the Co-Cu-Zr interfaces. The Co 2p XPS spectra demonstrates that the reduced temperature of cobalt oxides increases after doping Na, resulting in an increased Co^{3+}/Co^{2+} ratio from 1.21 to 1.30 (**Figure 3-15 Left**). The increasement of Co^{3+} can be attributed to the role of Na^+ in replacing Co^{3+}, thereby reaching a new equilibrium within the system and thus favoring the transformation of Cu^{2+} to Co^{3+}. The peak shift of the Co 3s XPS spectra is indicative of the influence of Na-Co interface electron transfer (**Figure S3-12**).

The analysis of copper oxides using X-ray photoelectron spectroscopy (XPS) has revealed the presence of lower-valence copper species in the Cu 2p spectra following sodium doping, demonstrating the partial reduction of Cu^{2+} into Cu^+ and Cu^0 (**Figure 3-15 Center**). The reduction can be attributed to the role of Na^+ in replacing Cu^{2+}, thereby reaching a new equilibrium within the system and thus favoring the transformation of Cu^{2+} to Cu^+ and Cu^0. Beyond this electronic effect, sodium also contributes to the stabilization of Cu^+ active sites and promotes copper dispersion across the support. The preservation of the structural integrity of catalytically relevant species is achieved by these dual roles, and the redox flexibility and adsorption characteristics of the material are profoundly enhanced as a consequence. The catalytic performance of the material in CO_2 hydrogenation is ultimately reshaped by these dual roles (**Figure 3-15 Right**). The electron-rich Zr surface is conducive to CO dissociation, which is critical to the formation of CH_xO intermediate. The peak of the binding energy of 182.3 and 184.5 eV could be assigned to ZrO_2. A further examination of Zr $3d_{5/2}$ of the catalyst revealed a $Zr^{(4-x)+}$ binding energy (180.5 eV) that exceeded that of metallic Zr (180.0 eV) and fell short of that of ZrO_2 (182.3 eV). Sodium substitutes Zr^{4+} sites predominantly in the form of Na^+, and in order to maintain electroneutrality the crystal lattice spontaneously generates positively charged oxygen vacancies as a charge-compensation mechanism. The incorporation of sodium thus results in the introduction of abundant oxygen vacancy defects, which stabilize the high-temperature amorphous phases of ZrO_2 and significantly enhance its oxygen-ion conductivity. Concurrently, the presence of oxygen vacancies instigates alterations to the surface electronic environment, thereby effecting a shift in the character of ZrO_2 from a state of weak acidity to one of greater basicity. Such a transformation is of catalytic importance, as the increased

basicity of the material promotes CO_2 adsorption and activation, while the stabilized lattice ensures the durability of the active phase under reaction conditions.

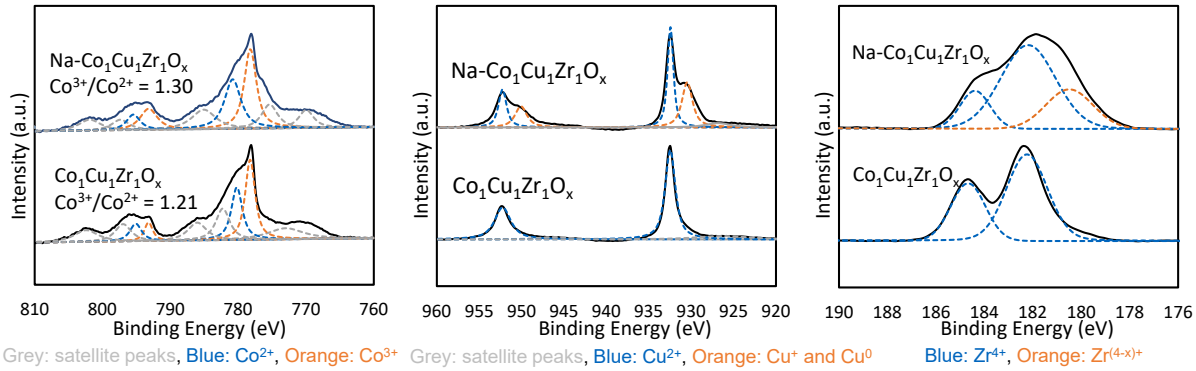

Figure 3-15. Identification the interfaces valence of the Na-$Co_1Cu_1Zr_1O_x$ and $Co_1Cu_1Zr_1O_x$. **(Left)** Deconvolution of Co 2p XPS spectra (Grey: satellite peaks, Blue: Co^{2+}, Orange: Co^{3+}); (**Center**) Deconvolution of Cu 2p XPS spectra (Grey: satellite peaks, Blue: Cu^{2+}, Orange: Cu^{+}); (**Right**) Deconvolution of Zr 3d XPS spectra (Blue: Zr^{4+}, Orange: $Zr^{\&+}$) of reduced samples of $Co_1Cu_1Zr_1O_x$ and 2wt% Na-$Co_1Cu_1Zr_1O_x$.

In parallel, Na doping exerts a suppressive effect on hydrogenation activity, thereby promoting the stabilization of CH_2 intermediates. Furthermore, the O 1s spectra indicate an augmented concentration of oxygen vacancies upon Na incorporation, thereby enhancing the exposure of coordinatively unsaturated Zr cations. These sites are of pivotal importance in the promotion of CH_xO intermediate formation (**Figure S3-13**). The Na 1s spectrum unequivocally validates the effective integration of Na into the catalyst structure (**Figure S3-14**), thereby reinforcing its electronic and structural function in modulating the reaction pathway. The presence of Na^+ within the structure has been demonstrated to increase CO_2 adsorption, adjust the valence of metals, and promote the yield of oxygenates.

In-situ XRD has been demonstrated to reveal the state of metal oxide, thus facilitating the confirmation of valence influence with the support of TPR. The X-ray diffraction (XRD) patterns of the synthesized catalysts exhibited distinct peaks that corresponded to the phase of amorphous ZrO_2, CuO and Co_3O_4 catalyst (**Figure 3-16**).

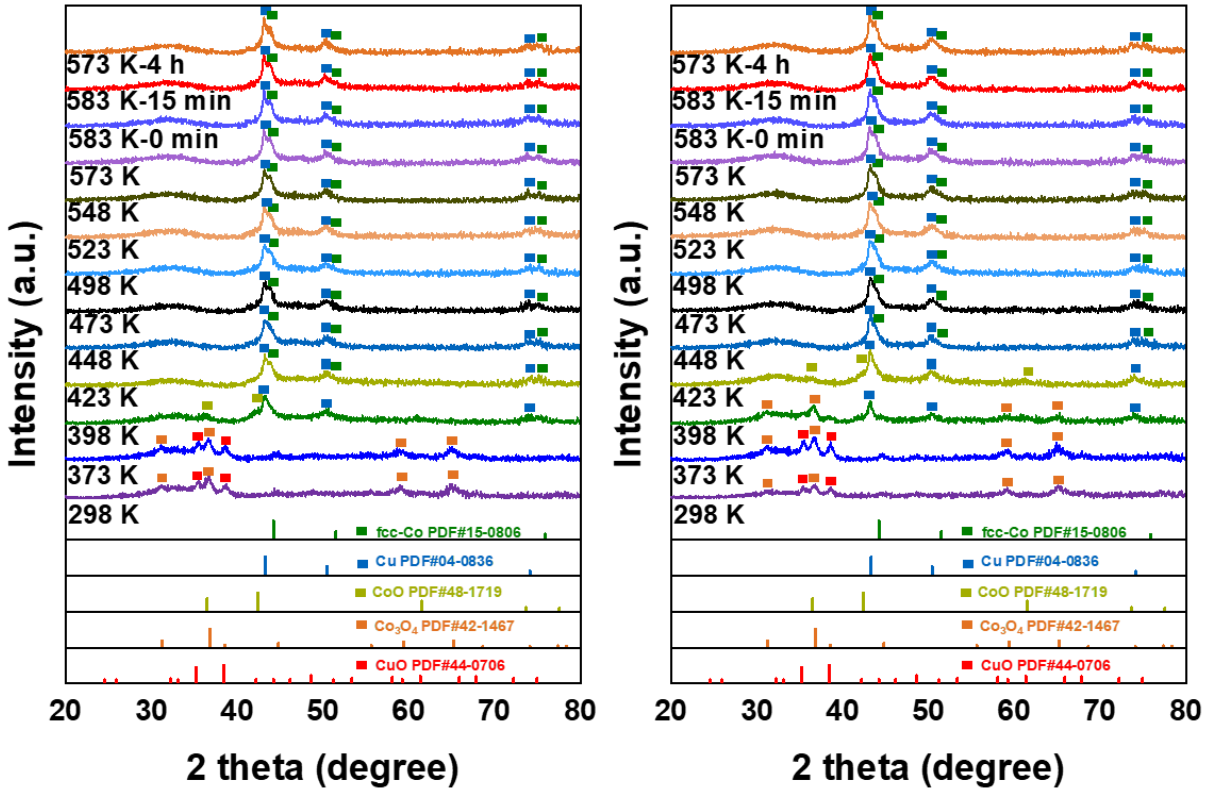

Figure 3-16. In situ XRD patterns of $Co_1Cu_1Zr_1O_x$ (**Left**) and 2wt% Na-$Co_1Cu_1Zr_1O_x$ (**Right**) in CO_2 hydrogenation at 1bar.

As the temperature of the $Co_1Cu_1Zr_1O_x$ sample increased in the presence of hydrogen, a slight shift from CuO and Co_3O_4 to metallic Cu and CoO to metallic Cu and hcp-Co diffraction peaks was observed, suggesting the total reduction of $Co_1Cu_1Zr_1O_x$ into fcc-Co, Cu and amorphous ZrO_2 at approximately 423 K. For amorphous ZrO_2, a broad peak between 30° and 40° was observed, which remained constant as the temperature was varied. As evidenced by the presence of the CuO and Co_3O_4, the 2wt% Na-$Co_1Cu_1Zr_1O_x$ sample exhibited an average dispersion of Na within the 2wt% Na-$Co_1Cu_1Zr_1O_x$ lattice. As the temperature increased in the 2wt% Na-$Co_1Cu_1Zr_1O_x$ sample under hydrogen flow conditions, a slight shift was observed from CuO and Co_3O_4 to metallic Cu and Co_3O_4 to metallic Cu and CoO to metallic Cu and hcp-Co diffraction peaks. It is suggested that the reduction of 2wt% Na-$Co_1Cu_1Zr_1O_x$ is impeded by the presence of Na in the catalyst. Furthermore, the total reduction of 2wt% Na-$Co_1Cu_1Zr_1O_x$ into fcc-Co, Cu and amorphous ZrO_2 at approximately 448 K is also proposed. As illustrated in **Figure 3-16 Left**, the initial formation of metallic Cu was followed by the emergence of fcc-Co adjacent to the Cu diffraction peak, indicating that the presence of Cu facilitates the formation of a Co-Cu alloy and stabilizes the fcc-Co phase over the thermodynamically favored hcp-Co phase. Furthermore, the formation of fcc-Co, stabilized by the Co-Cu interaction,

enhances catalytic performance due to its higher structural stability and superior intrinsic activity when compared to hcp-Co of the separated synthesis method illustrated in **Figure 3-16 Right**. In the case of amorphous ZrO_2, a broad peak is observed between 30° and 40°, which remains constant and unaltered across the range of temperatures. The absence of sodium composites peaks indicated the formation of a highly dispersed sodium composites phase, devoid of large agglomerates.

It was established that the addition of sodium resulted in a significant reduction in the overall temperature delay, thereby indicating its role as an inhibitor of the reduction of cobalt oxide in 2wt% Na-$Co_1Cu_1Zr_1O_x$ towards the fcc-Co phase, thus unveiling the underlying function between Cu-Co. The TPR results for each catalyst confirmed a reduced temperature shift of approximately 20 K from 419 K to 441 K, which was necessary to obtain the fcc-Co, Cu and amorphous ZrO_2 (**Figure S3-9**).

3.4.11 Comparison with other catalytic systems

The Cu-Zr and Co-Cu-Zr series catalysts have been demonstrated to establish higher methanol and ethanol STY in comparison to the reference catalysts. A comparison of $Cu_2Zr_1O_x$ and Cu-Zn-Al with the other benchmark catalysts revealed that the space time yield (STY) of the former was considerably higher than that of the latter and even exceeded the highest methanol STY in reference (**Figure 3-17 Left**). For 2wt% Na-$Co_1Cu_1Zr_1O_x$, the space time yield (STY) of ethanol was found to be approximately 3.8 $mmol \cdot g_{cat}^{-1} \cdot h^{-1}$ and beyond almost all the other reference catalysts (**Figure 3-17 Right**). It is evident that Co-Cu-Zr catalysts demonstrate a high level of foresight in the synthesis of alcohols[27,35,37,44-54].

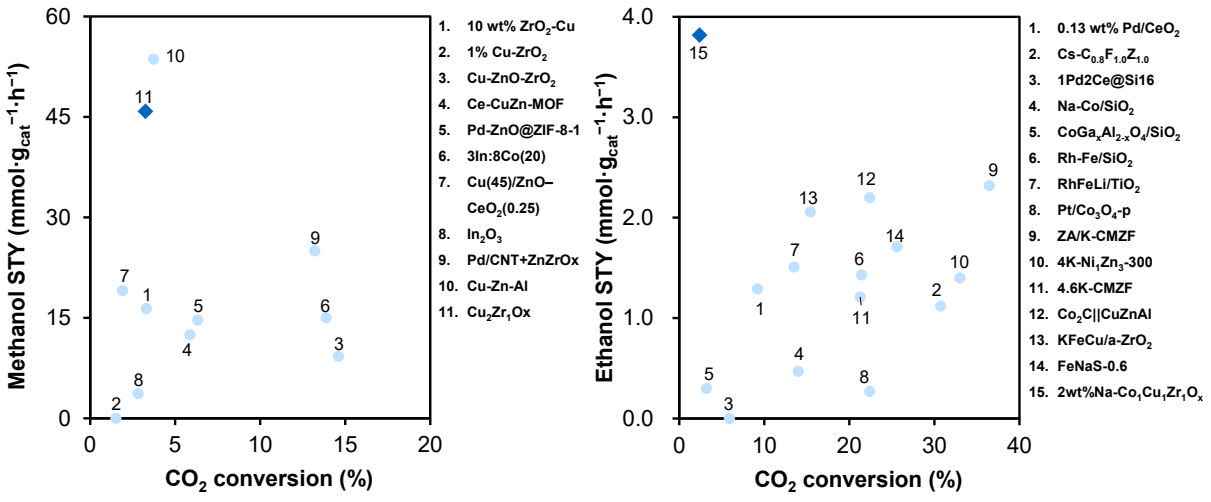

Figure 3-17. Comparison of the $Cu_2Zr_1O_x$ and 2wt% Na-$Co_1Cu_1Zr_1O_x$ sample with the reported catalysts.

(**Left**) methanol synthesis catalysts and (**Right**) ethanol synthesis catalysts. All the experiments are regarded as CO free and analyzed at 2-5 MPa, 1.5-150 $L \cdot g_{cat}^{-1} \cdot h^{-1}$, and 200-350 °C.

For the synthesis of methanol, the Cu-Zn-Al catalyst, which is extensively utilized and serves as a baseline for comparison, was employed. While $Cu_2Zr_1O_x$ catalyst exhibited a CO_2 conversion of 3.7%, the product distribution was heavily skewed towards methanol, thereby demonstrating a comparable STY with the Cu-Zn-Al catalyst, without the presence of ethanol being detected. The predominant methanol production can be attributed to the strong methanol-forming ability of the Cu-Zr interface, which facilitates the hydrogenation of CH_xO intermediates but lacks sufficient C-C coupling activity for C_2+ product formation[6,9,11,14,21,55-58].

Extensive studies have been conducted on the 2wt% Na-$Co_1Cu_1Zr_1O_x$ catalyst, with a focus on its utilization in the production of higher alcohols and hydrocarbons from CO_2 hydrogenation. The catalyst exhibits a CO_2 conversion of 2.4%, accompanied by an ethanol selectivity of 15.1%, making it a promising candidate for further research in this field. The over-hydrogenation of intermediates on Co sites is likely to have contributed to the formation of undesired hydrocarbons. The superior ethanol selectivity exhibited by the 2wt% Na-$Co_1Cu_1Zr_1O_x$ catalyst can be attributed to the synergistic interaction between its components. In comparison with other catalytic systems, the 2wt% Na-$Co_1Cu_1Zr_1O_x$ catalyst achieves an optimal balance between CO_2 activation and C_2+ alcohol formation. The catalyst's distinctive capacity to amalgamate the advantages inherent in Co-based, Cu-based and Cu-based systems enables it to surpass conventional catalysts with regard to ethanol selectivity.

3.5 Conclusion

The present work focuses on the Co-Cu-Zr series catalyst, with the aim of identifying the cobalt and copper and zirconia contents ratio and sodium content of CO_2 hydrogenation to ethanol as a case study. A particular focus has been placed on the specific reaction products of the catalysts, and their correlation with the in-situ textural and structural characteristics of the 2wt% Na-$Co_1Cu_1Zr_1O_x$ sample.

It is generally accepted that the Co-Cu-Zr surface is conducive to the formation of active surface sites for C-C coupling, a process facilitated by the presence of $*CH_x$ and $*CH_xO$ intermediates. It can thus be concluded that an increase in the amount of Co result in a change in the ratio of $*CH_x$ and $*CH_xO$ intermediates, as a result, to a transfer in specific product ethanol yield. Furthermore, the analysis of this work revealed that the specific activity of the catalysts exhibited a definitive trend with variations in the specific Co-Cu surface. It is evident

from the analysis that the true challenge lies in tailoring the Co-Cu content to favor the development of surface traits that also contribute to the enhancement of the intrinsic activity of the Co-Cu-Zr catalyst, as well as the influence of the high-activity crystal structure of fcc-Co and amorphous ZrO_2. The designated choice of a Na doped in the current work was a deliberate step taken to the influence of the valence interactions of Co, Cu and Zr and hydrogenation among CH_2 and CH_3 intermediates, which would adjust the analysis of catalytic performance metrics. It is noteworthy that the insights gained from this work can serve as a paradigm for alkali doped Co-Cu-Zr based catalysts that are commonly used in the synthesis of high alcohols.

3.6 Acknowledgements

C. L. is grateful to the Chinese Scholarship Council for financial support.

3.7 Appendix

Figure. S3-1.

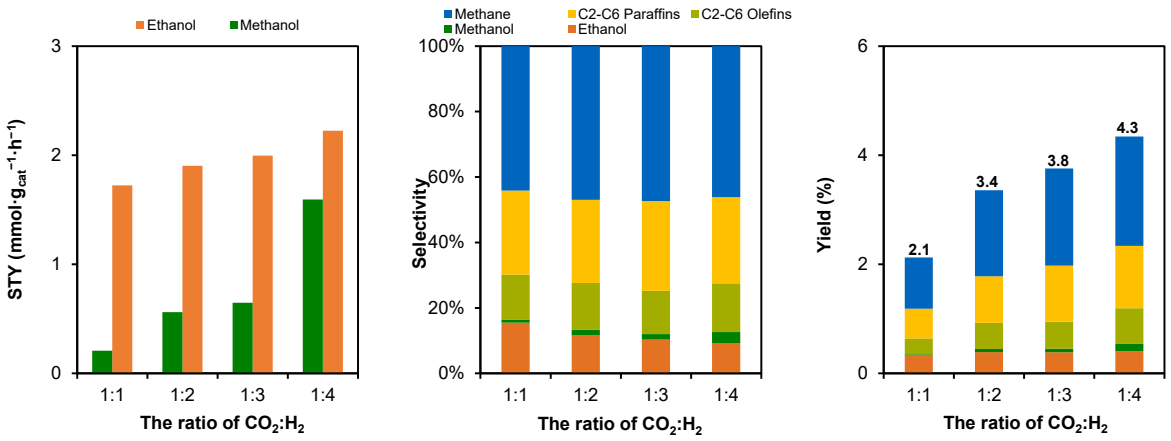

Figure. S3-1. Catalytic performance of 2wt% Na-$Co_1Cu_1Zr_1O_x$ catalysts prepared using different CO_2/H_2 ratio from 1/1-1/4. All the experiments are regarded as CO free and analyzed at 300 °C, 5.0 MPa, space velocity = 150 $L \cdot g_{cat}^{-1} \cdot h^{-1}$. Controlling CO_2 as 9 mL/min and changing the ratio of H_2.

Figure. S3-2.

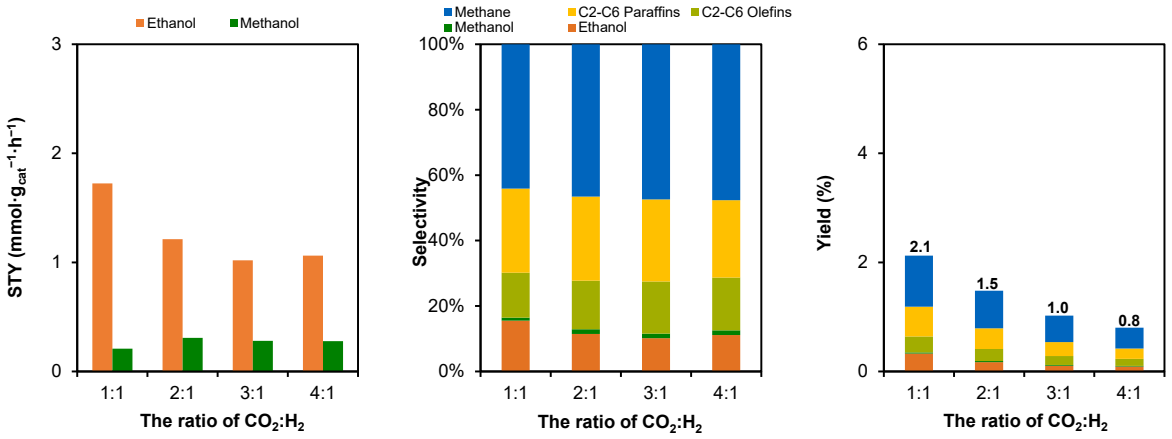

Figure. S3-2. Catalytic performance of 2wt% Na-$Co_1Cu_1Zr_1O_x$ catalysts prepared using different CO_2/H_2 ratio from 1/1-4/1. All the experiments are regarded as CO free and analyzed at 300 °C, 5.0 MPa, space velocity = 150 $L \cdot g_{cat}^{-1} \cdot h^{-1}$. Controlling H_2 as 9 mL/min and changing the ratio of CO_2.

Figure. S3-3.

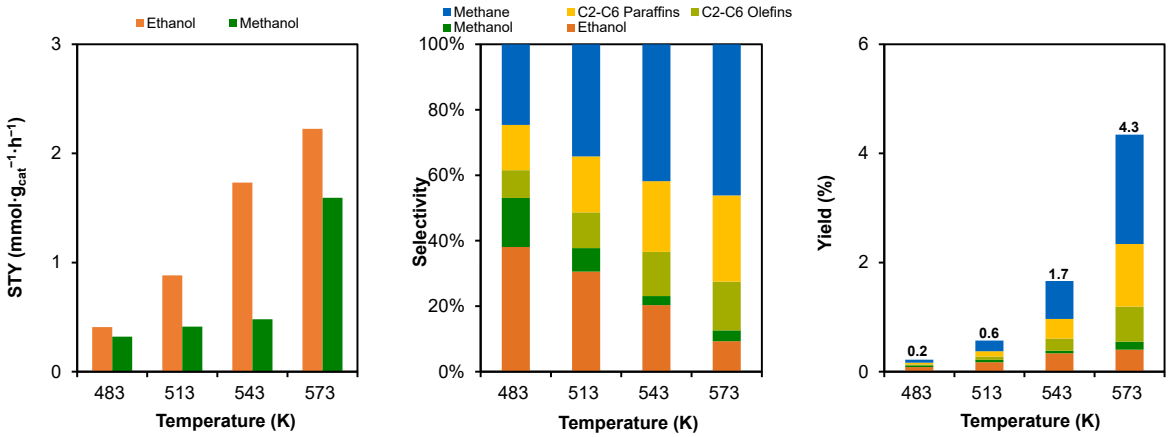

Figure. S3-3. Catalytic performance of 2wt% Na-$Co_1Cu_1Zr_1O_x$ catalysts prepared using different temperatures. All the experiments are regarded as CO free and analyzed at 483-573 K, 5.0 MPa, space velocity = 150 $L \cdot g_{cat}^{-1} \cdot h^{-1}$.

Figure. S3-4.

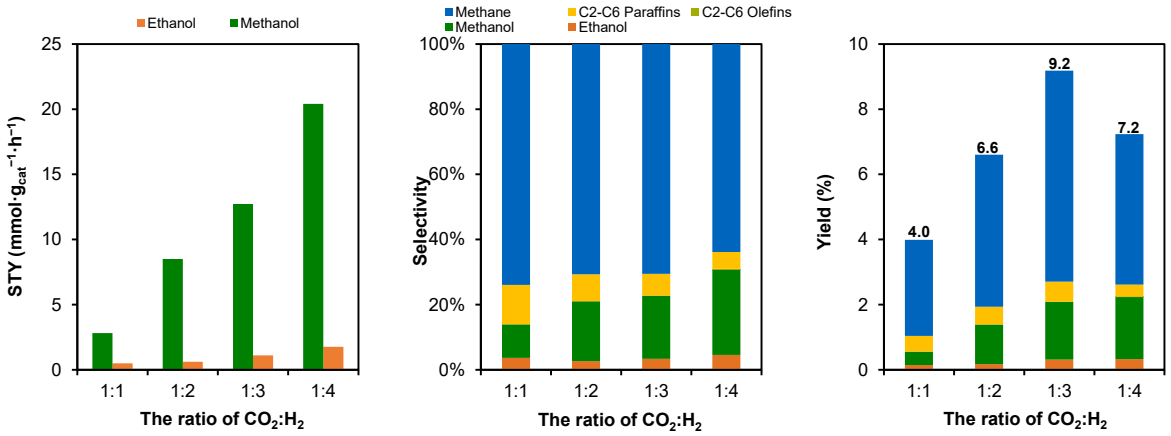

Figure. S3-4. Catalytic performance of $Co_1Cu_1Zr_1O_x$ catalysts prepared using different CO_2/H_2 ratio from 1/1-1/4. All the experiments are regarded as CO free and analyzed at 300 °C, 5.0 MPa, space velocity = 150 $L \cdot g_{cat}^{-1} \cdot h^{-1}$. Controlling CO_2 as 9 mL/min and changing the ratio of H_2.

Figure. S3-5.

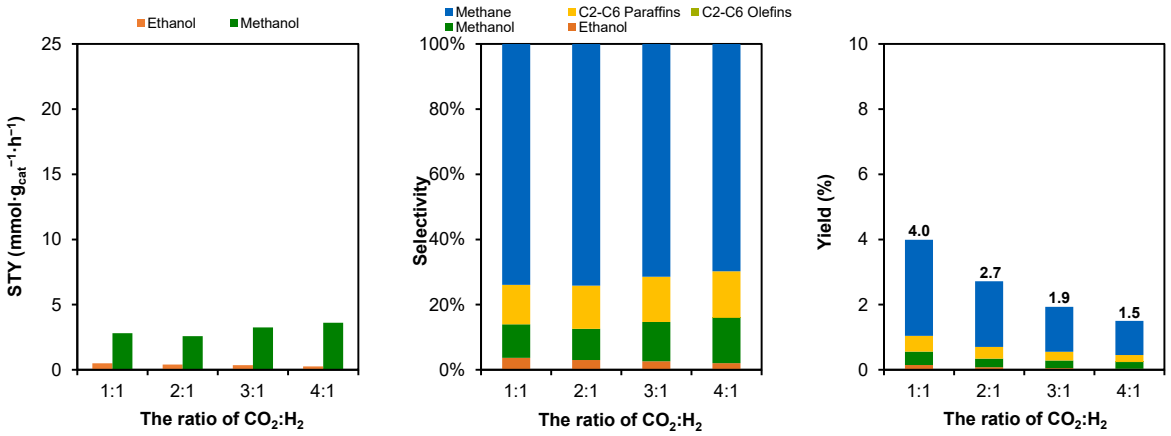

Figure. S3-5. Catalytic performance of $Co_1Cu_1Zr_1O_x$ catalysts prepared using different CO_2/H_2 ratio from 1/1-4/1. All the experiments are regarded as CO free and analyzed at 300 °C, 5.0 MPa, space velocity = 150 $L \cdot g_{cat}^{-1} \cdot h^{-1}$. Controlling H_2 as 9 mL/min and changing the ratio of CO_2.

Figure. S3-6.

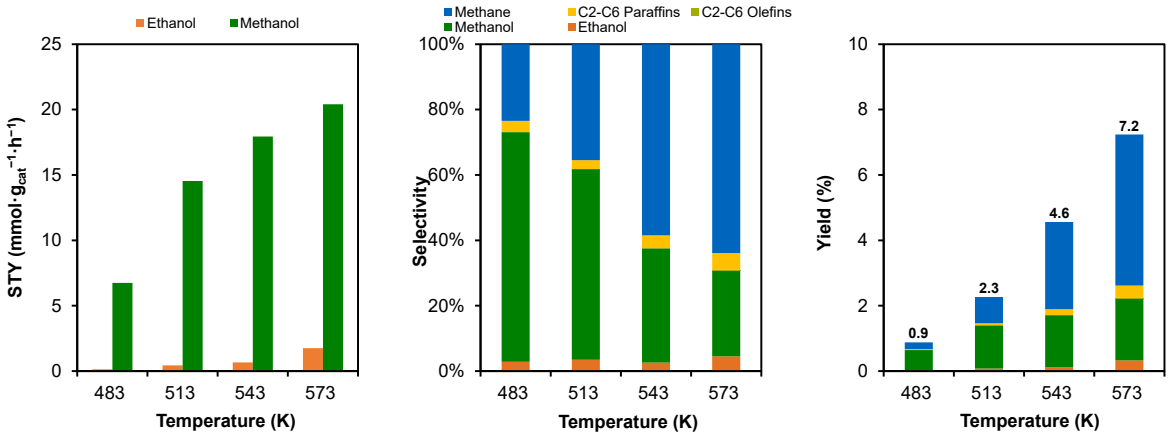

Figure. S3-6. Catalytic performance of $Co_1Cu_1Zr_1O_x$ catalysts prepared using different temperatures. All the experiments are regarded as CO free and analyzed at 483-573 K, 5.0 MPa, space velocity = 150 $L \cdot g_{cat}^{-1} \cdot h^{-1}$.

Figure. S3-7.

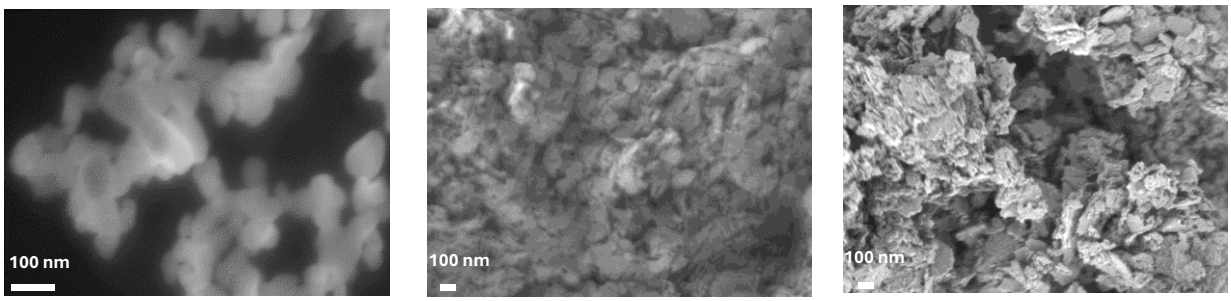

$Cu_2Zr_1O_x$ **$Co_1Cu_1Zr_1O_x$** **2wt% Na-$Co_1Cu_1Zr_1O_x$**

Figure. S3-7. SEM images of $Cu_2Zr_1O_x$, $Co_1Cu_1Zr_1O_x$, 2 wt% Na-$Co_1Cu_1Zr_1O_x$ catalysts.

Figure. S3-8.

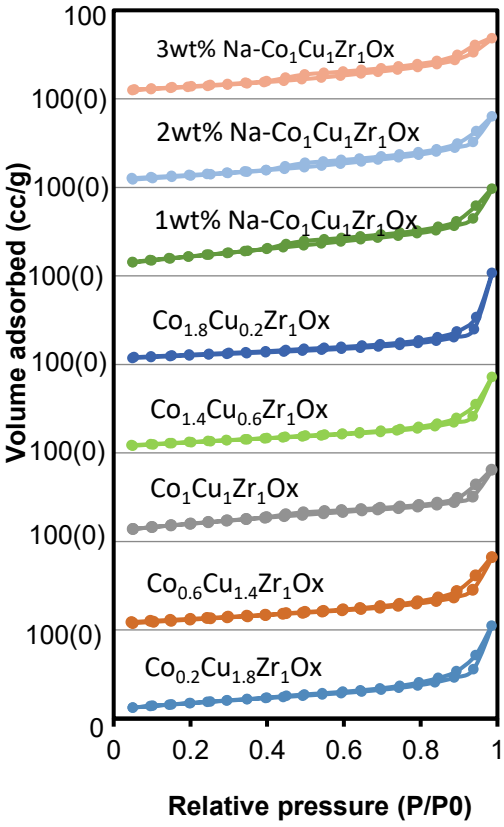

Figure. S3-8. N_2 adsorption-desorption isotherm of 3 wt% Na-$Co_1Cu_1Zr_1O_x$, 2 wt% Na-$Co_1Cu_1Zr_1O_x$, 1 wt% Na-$Co_1Cu_1Zr_1O_x$, $Co_{1.8}Cu_{0.2}Zr_1O_x$, $Co_{1.4}Cu_{0.6}Zr_1O_x$, $Co_1Cu_1Zr_1O_x$, $Co_{0.6}Cu_{1.4}Zr_1O_x$ and $Co_{0.2}Cu_{1.8}Zr_1O_x$ catalysts.

Figure. S3-9.

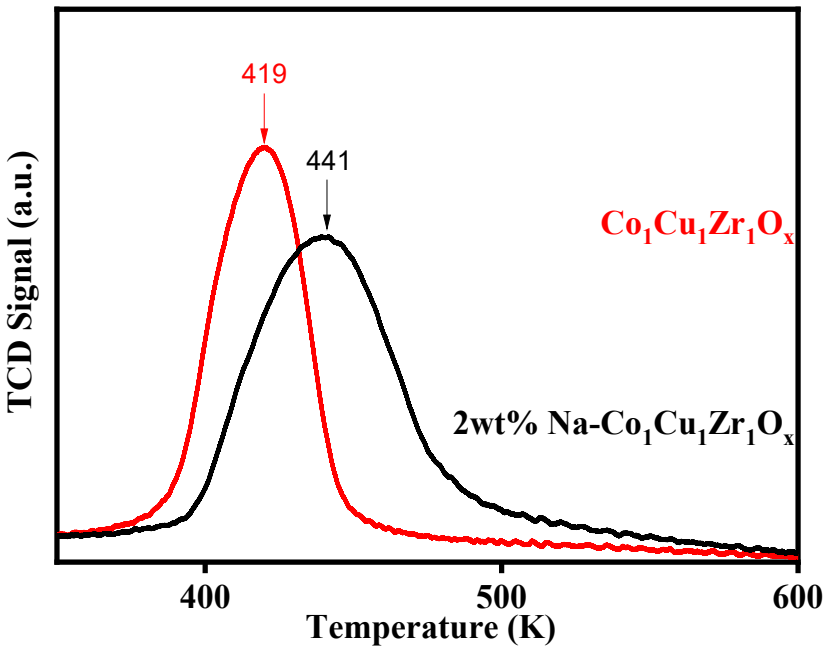

Figure. S3-9. H_2-TPR profiles of $Co_1Cu_1Zr_1O_x$ and 2 wt% Na-$Co_1Cu_1Zr_1O_x$ catalysts.

Figure. S3-10.

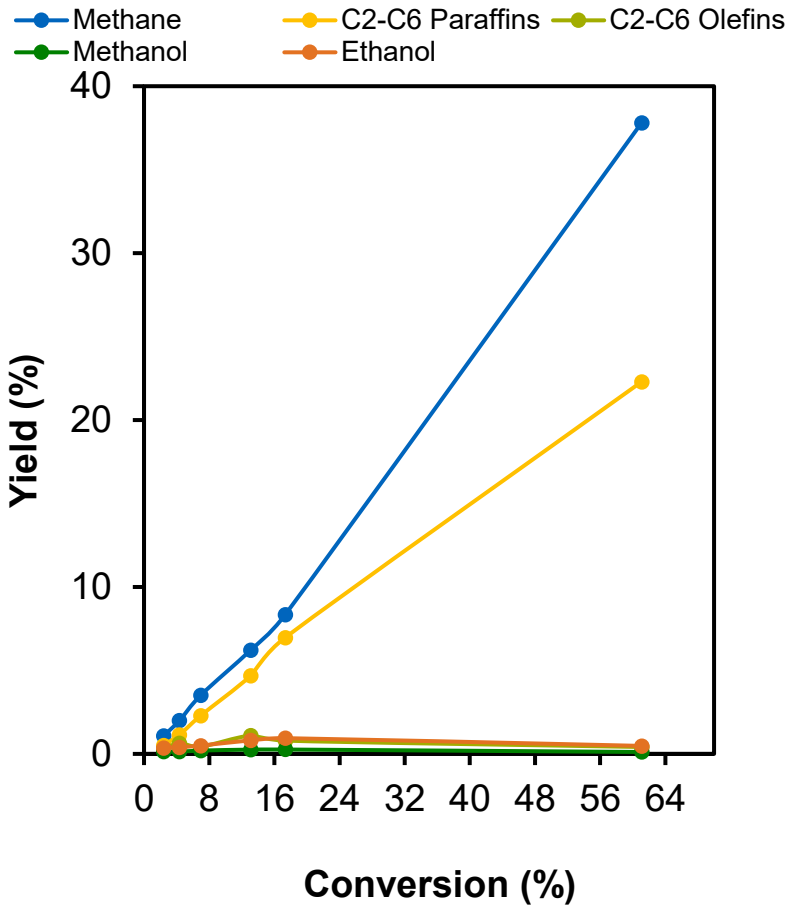

Figure S3-10. Methane, C_2-C_6 paraffins, C_2-C_6 olefins, methanol and ethanol catalytic yield for 2 wt% Na-$Co_1Cu_1Zr_1O_x$ with CO_2 conversion shift. All the experiments are regarded as CO free and analyzed at 300°C, 5.0 MPa, space time = 0.01-0.59 s, H_2/CO_2 = 4.

Figure. S3-11.

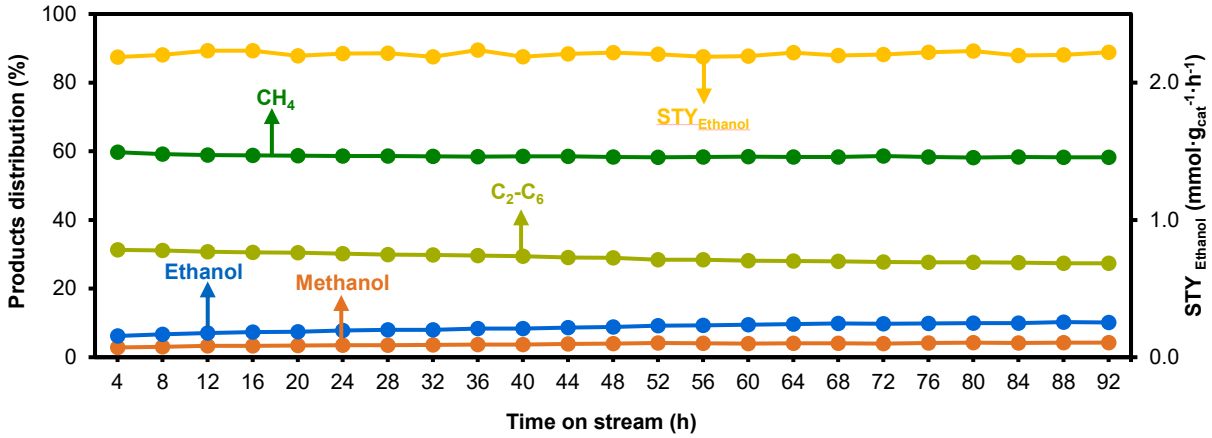

Figure. S3-11. Catalytic stability test of 2 wt% Na-$Co_1Cu_1Zr_1O_x$ within 92 hours. Reaction conditions: 300°C, 5.0 MPa, space velocity = 150 $L \cdot g_{cat}^{-1} \cdot h^{-1}$, $H_2/CO_2 = 4$. All the experiments are regarded as CO free.

Figure. S3-12.

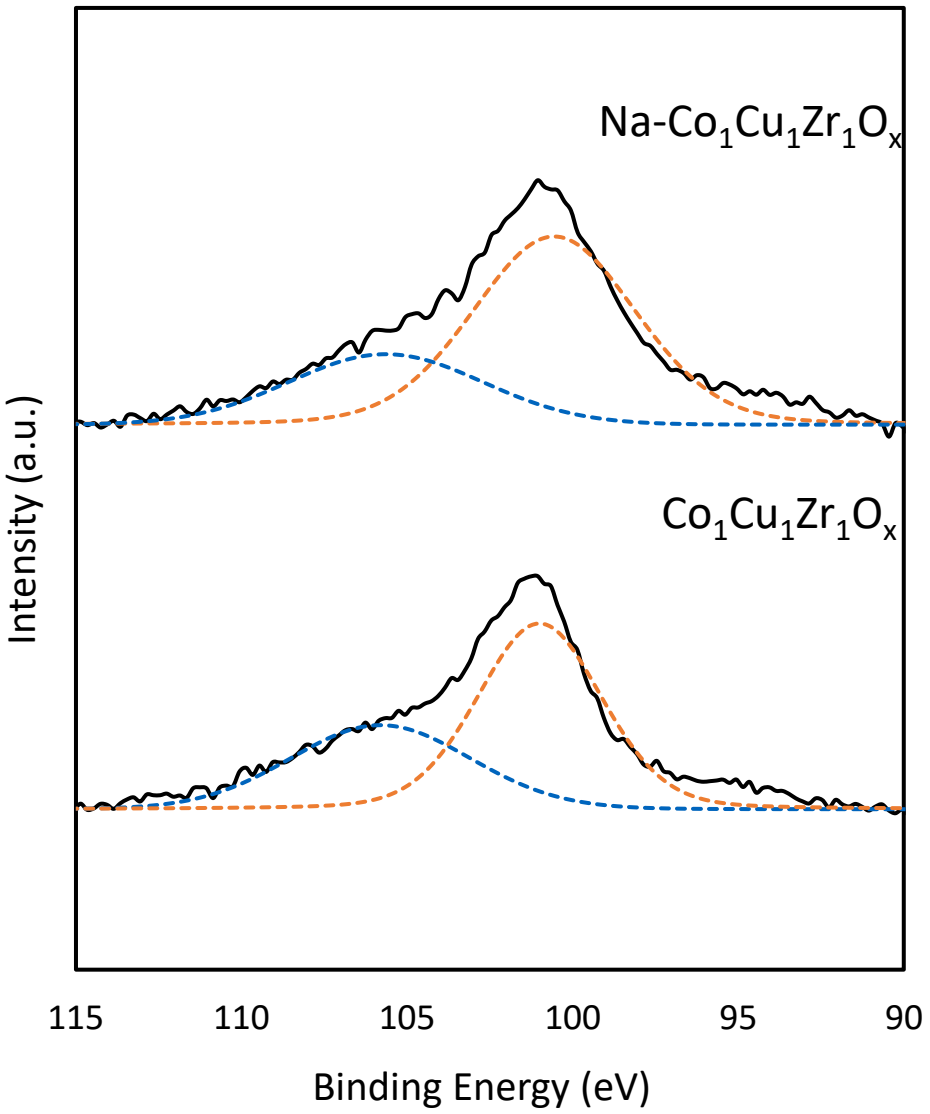

Figure. S3-12. Deconvolution of Co 3s region (in XPS data) of the samples of $Co_1Cu_1Zr_1O_x$ and 2wt% Na-$Co_1Cu_1Zr_1O_x$.

Figure. S3-13.

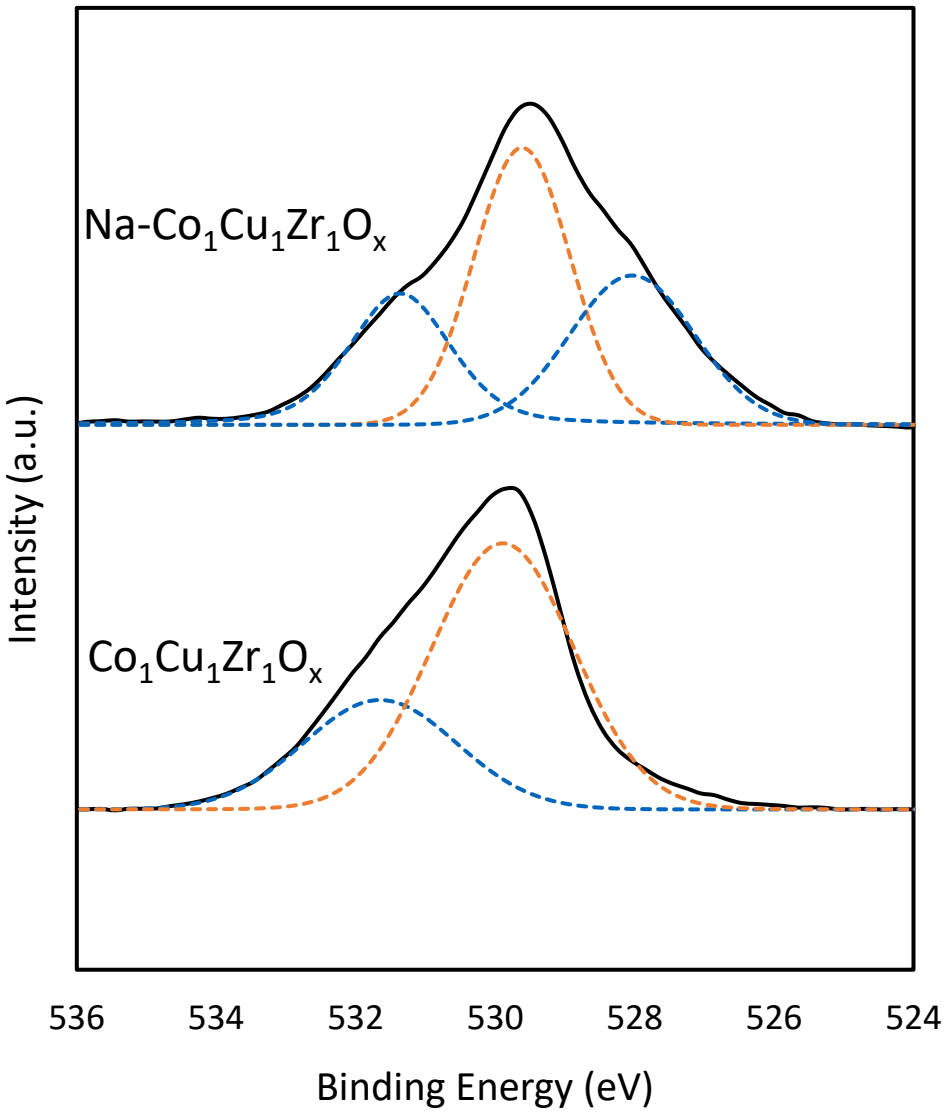

Figure. S3-13. Deconvolution of O 1s region (in XPS data) of the samples of $Co_1Cu_1Zr_1O_x$ and 2wt% Na-$Co_1Cu_1Zr_1O_x$.

Figure. S3-14.

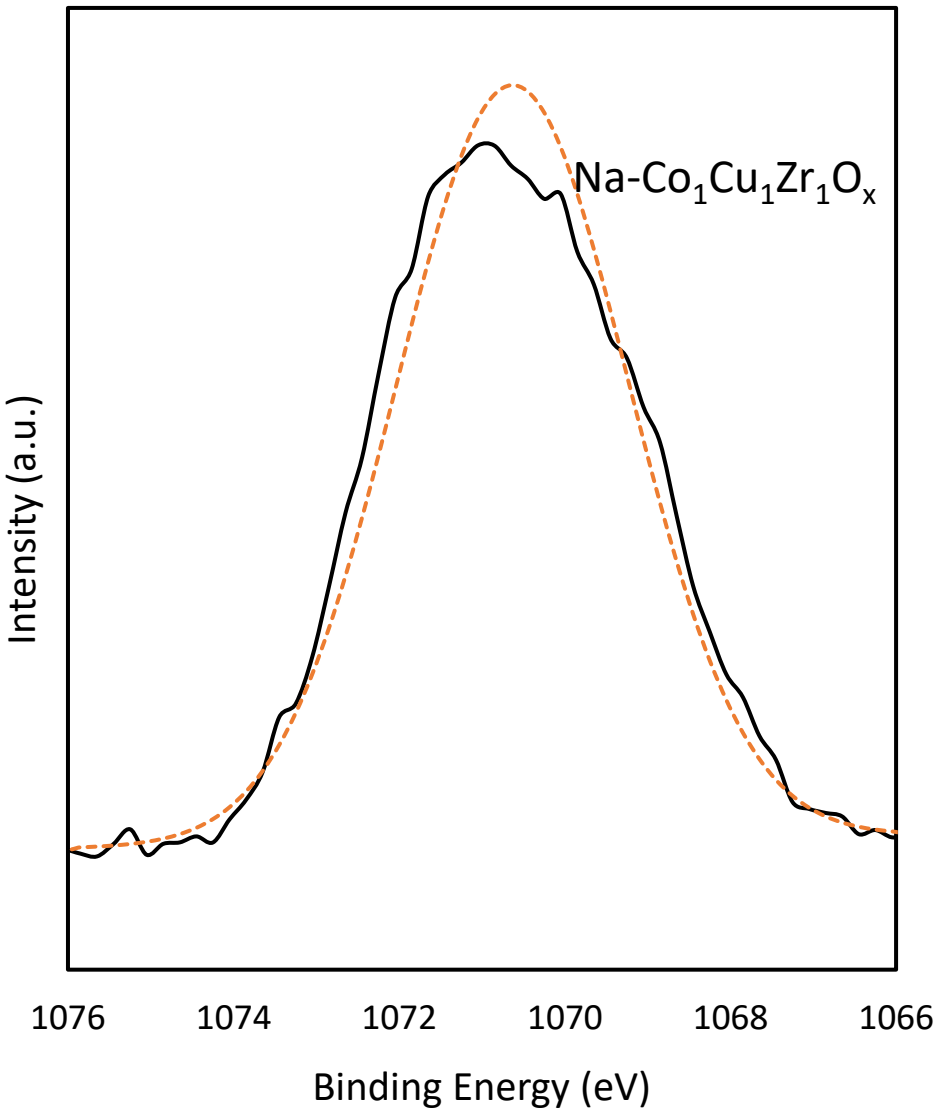

Figure. S3-14. Deconvolution of Na 1s region (in XPS data) of the samples of 2wt% Na-$Co_1Cu_1Zr_1O_x$.

Table. S3-1.

Catalysts	Na content (%)	Co content (%)	Cu content (%)	Zr content (%)
$Co_1Cu_1Zr_1O_x$	0	18.3	23.5	32.7
1 wt% Na-$Co_1Cu_1Zr_1O_x$	0.875	17.2	23.5	34.1
2 wt% Na-$Co_1Cu_1Zr_1O_x$	1.96	17.2	21.9	35.9
3 wt% Na-$Co_1Cu_1Zr_1O_x$	3.15	16.4	21.0	36.3

Table. S3-1. The elements content of $Co_1Cu_1Zr_1O_x$, 1 wt% Na-$Co_1Cu_1Zr_1O_x$, 2 wt% Na-$Co_1Cu_1Zr_1O_x$, 3 wt% Na-$Co_1Cu_1Zr_1O_x$ catalysts analyzed by AAS.

Table. S3-2.

Catalysts	Active sites dispersion (%)
$Co_1Cu_1Zr_1O_x$	**5.5**
2 wt% Na-$Co_1Cu_1Zr_1O_x$	**5.3**

Table. S3-2. The active sites (Co, Cu) dispersion of all the catalysts with the result of H_2 chemisorption and AAS.

Table. S3-3.

Temperature (K)	TOF of 2 wt% Na-$Co_1Cu_1Zr_1O_x$ (s^{-1})
483	0.002
513	0.005
543	0.014
573	0.040

Table. S3-3. The turnover frequency of 2 wt% Na-$Co_1Cu_1Zr_1O_x$ catalyst from 483 to 573 K.

Table. S3-4.

Catalysts	Surface area (m^2/g)
3 wt% Na-$Co_1Cu_1Zr_1O_x$	**50.76**
2 wt% Na-$Co_1Cu_1Zr_1O_x$	**52.25**
1 wt% Na-$Co_1Cu_1Zr_1O_x$	**82.44**
$Co_{1.8}Cu_{0.2}Zr_1O_x$	**37.43**
$Co_{1.4}Cu_{0.6}Zr_1O_x$	**45.71**
$Co_1Cu_1Zr_1O_x$	**74.15**
$Co_{0.6}Cu_{1.4}Zr_1O_x$	**46.81**
$Co_{0.2}Cu_{1.8}Zr_1O_x$	**63.63**

Table. S3-4. The surface area of all the reduced catalyst.

Table. S3-5.

Surface species	Wavenumber (cm^{-1})	Ref.
CH_4	3015, 1303	ACS Catal. 2023, 13, 7, 4667–4674 Angew. Chem. Int. Ed. 2020, 59, 19983–19989
*CH_x	3017, 2966, 2956, 2928, and 2856	Appl. Catal., B 2021, 298, 120567 J. Phys. Chem. C 2011, 115, 1361–1367
*CH_xO	2937-2941 1070-1082 2824-2826 1270, 1034	ACS Catal. 2020, 10, 24, 14516–14526 ACS Catal. 2023, 13, 7, 4667–4674 ACS Catal. 2020, 10, 21, 12828–12840
Gaseous CO	2176, 2110, 2085	ACS Catal. 2020, 10, 9, 5250–5260 ACS Catal. 2023, 13, 7, 4667–4674
Bridged carbonyl species	1900-2060	Nat. Catal., 2018, 127–134
*HCOO	1337-1393 1593-1622	ACS Catal. 2023, 13, 7, 4667–4674 ACS Catal. 2020, 10, 24, 14516–14526
*CO_3	1393, 1325 and 1274	ACS Catal. 2023, 13, 7, 4667–4674 Appl. Catal., A 2025, 288, 126-133

Table. S3-5. The assignments of IR bands in the DRIFTS spectra.

3.8 Reference

1 R. E. Zeebe, J. C. Zachos, K. Caldeira & T. Tyrrell. Carbon Emissions and Acidification. *Science*, 321 (2008) 51-52.

2 J. Graciani, K. Mudiyanselage, F. Xu *et al.* Highly active copper-ceria and copper-ceria-titania catalysts for methanol synthesis from CO_2. *Science*, 345 (2014) 546-549.

3 J. J. Wang, G. N. Li, Z. L. Li *et al.* A highly selective and stable ZnO-ZrO_2 solid solution catalyst for CO_2 hydrogenation to methanol. *Sci. Adv.*, 3 (2017) e1701290.

4 G. Bonura, M. Cordaro, C. Cannilla, F. Arena & F. Frusteri. The changing nature of the active site of Cu-Zn-Zr catalysts for the CO_2 hydrogenation reaction to methanol. *Appl. Catal., B*, 152 (2014) 152-161.

5 X. W. Song, C. S. Yang, X. H. Li *et al.* On the Role of Hydroxyl Groups on Cu/Al_2O_3 in CO_2 Hydrogenation. *ACS Catal.*, 12 (2022) 14162-14172.

6 R. Ye, L. Ma, J. Mao *et al.* A Ce-CuZn catalyst with abundant Cu/Zn-O_V-Ce active sites for CO_2 hydrogenation to methanol. *Nat. Commun.*, 15 (2024) 2159.

7 M. Behrens, F. Studt, I. Kasatkin *et al.* The Active Site of Methanol Synthesis over Cu/ZnO/Al_2O_3 Industrial Catalysts. *Science*, 336 (2012) 893-897.

8 Y. Zhu, J. Zheng, J. Ye *et al.* Copper-zirconia interfaces in UiO-66 enable selective catalytic hydrogenation of CO_2 to methanol. *Nat. Commun.*, 11 (2020) 5849.

9 Y. Wang, S. Kattel, W. Gao *et al.* Exploring the ternary interactions in Cu-ZnO-ZrO_2 catalysts for efficient CO_2 hydrogenation to methanol. *Nat. Commun.*, 10 (2019) 1166.

10 P. Gao, S. Li, X. Bu *et al.* Direct conversion of CO_2 into liquid fuels with high selectivity over a bifunctional catalyst. *Nat. Chem.*, 9 (2017) 1019-1024.

11 C. Wu, L. Lin, J. Liu *et al.* Inverse ZrO_2/Cu as a highly efficient methanol synthesis catalyst from CO_2 hydrogenation. *Nat. Commun.*, 11 (2020) 5767.

12 S. Kattel, P. J. Ramírez, J. G. Chen, J. A. Rodriguez & P. Liu. Active sites for CO_2 hydrogenation to methanol on Cu/ZnO catalysts. *Science*, 355 (2017) 1296-1299.

13 Y. Xu, Z. Gao, Y. Xu *et al.* Cu-supported nano-$ZrZnO_x$ as a highly active inverse catalyst for low temperature methanol synthesis from CO_2 hydrogenation. *Appl. Catal., B*, 344 (2024) 123656.

14 K. Lee, P. C. D. Mendes, H. Jeon *et al.* Engineering nanoscale H supply chain to accelerate methanol synthesis on $ZnZrO_x$. *Nat. Commun.*, 14 (2023) 819.

15 M. T. Xu, M. J. L. Gines, A. M. Hilmen, B. L. Stephens & E. Iglesia. Isobutanol and Methanol Synthesis on Copper Catalysts Supported on Modified Magnesium Oxide. *J. Catal.*, 171 (1997) 130-147.

16 H. Zhou, Z. X. Chen, A. V. López *et al.* Engineering the Cu/Mo_2CT_x (MXene) interface to drive CO_2 hydrogenation to methanol. *Nat. Catal.*, 4 (2021) 860-871.

17 C. Hu, Z. Jiang, Q. Wu *et al.* Selective CO_2 reduction to CH_3OH over atomic dual-metal sites embedded in a metal-organic framework with high-energy radiation. *Nat. Commun.*, 14 (2023) 4767.

18 G. Liu, P. Liu, D. Meng *et al.* CO_x hydrogenation to methanol and other hydrocarbons under mild conditions with Mo_3S_4@ZSM-5. *Nat. Commun.*, 14 (2023) 513.

19 X. Chen, H. Abdullah & D. H. Kuo. CuMnOS Nanoflowers with Different Cu^+/Cu^{2+} Ratios for the CO_2-to-CH_3OH and the CH_3OH-to-H_2 Redox Reactions. *Sci. Rep.*, 7 (2017) 41194.

20 B. An, J. Zhang, K. Cheng *et al.* Confinement of Ultrasmall Cu/ZnO_x Nanoparticles in Metal-Organic Frameworks for Selective Methanol Synthesis from Catalytic Hydrogenation of CO_2. *J. Am. Chem. Soc.*, 139 (2017) 3834-3840.

21 H. B. Zhao, R. F. Yu, S. C. Ma *et al.* The role of Cu_1–O_3 species in single-atom Cu/ZrO_2 catalyst for CO_2 hydrogenation. *Nat. Catal.*, 5 (2022) 818-831.

22 M. Zabilskiy, V. L. Sushkevich, D. Palagin *et al.* The unique interplay between copper and zinc during catalytic carbon dioxide hydrogenation to methanol. *Nat. Commun.*, 11 (2020) 2409.

23 J. Gu, W. Gong, Q. Zhang *et al.* Enabling direct-growth route for highly efficient ethanol upgrading to long-chain alcohols in aqueous phase. *Nat. Commun.*, 14 (2023) 7935.

24 F. Li, Y. C. Li, Z. Wang *et al.* Cooperative CO_2-to-ethanol conversion via enriched intermediates at molecule–metal catalyst interfaces. *Nat. Catal.*, 3 (2019) 75-82.

25 Q. Qian, J. Zhang, M. Cui & B. Han. Synthesis of acetic acid via methanol hydrocarboxylation with CO_2 and H_2. *Nat. Commun.*, 7 (2016) 11481.

26 X. San, Y. Zhang, W. Shen & N. Tsubaki. New Synthesis Method of Ethanol from Dimethyl Ether with a Synergic Effect between the Zeolite Catalyst and Metallic Catalyst. *Energy Fuels*, 23 (2019) 2843-2844.

27 J. Chen, Y. Zha, B. Liu *et al.* Rationally Designed Water Enriched Nano Reactor for Stable CO_2 Hydrogenation with Near 100% Ethanol Selectivity over Diatomic Palladium Active Sites. *ACS Catal.*, 13 (2023) 7110-7121.

28 L. Wang, L. Wang, J. Zhang *et al.* Selective Hydrogenation of CO_2 to Ethanol over Cobalt Catalysts. *Angew. Chem. Int. Ed*, 57 (2018) 6104-6108.

29 J. Kang, S. He, W. Zhou *et al.* Single-pass transformation of syngas into ethanol with high selectivity by triple tandem catalysis. *Nat. Commun.*, 11 (2020) 827.

30 V. D. Lage, A. Le Valant, N. Bion & F. S. Toniolo. Tuning Co-Cu-Al catalysts and their reaction conditions on the CO_2 hydrogenation reaction to higher alcohols under mild conditions. *Chem. Eng. Sci.*, 281 (2023) 119208.

31 M. Suvarna, T. Zou, S. H. Chong *et al.* Active learning streamlines development of high performance catalysts for higher alcohol synthesis. *Nat. Commun.*, 15 (2024) 5844.

32 B. An, Z. Li, Y. Song *et al.* Cooperative copper centres in a metal-organic framework for selective conversion of CO_2 to ethanol. *Nat. Catal.*, 2 (2019) 709-717.

33 Y. Zhou, Y. Q. Wang, H. J. Lu *et al.* Highly Dispersed K- and Pd-Comodified Fe Catalyst for CO_2 Hydrogenation to Higher Alcohols. *Acs Sustain. Chem. Eng.*, 12 (2024) 3322-3330.

34 C. Y. Dai, X. Zhao, B. R. Hu *et al.* Hydrogenation of CO_2 to Aromatics over Fe−K/Alkaline Al_2O_3 and P/ZSM-5 Tandem Catalysts. *Ind. Eng. Chem. Res.*, 59 (2020) 19194-19202.

35 T. K. Liu, D. Xu, M. Y. Song, X. L. Hong & G. L. Liu. K-ZrO_2 Interfaces Boost CO_2 Hydrogenation to Higher Alcohols. *ACS Catal.*, 13 (2023) 4667-4674.

36 H. Z. Li, C. L. Qiu, S. J. Ren *et al.* Na^+-gated water-conducting nanochannels for boosting CO_2 conversion to liquid fuels. *Science*, 367 (2020) 667-671.

37 D. Xu, M. Y. Ding, X. L. Hong, G. L. Liu & S. C. E. Tsang. Selective C_2+ Alcohol Synthesis from Direct CO_2 Hydrogenation over a Cs-Promoted Cu-Fe-Zn Catalyst. *ACS Catal.*, 10 (2020) 5250-5260.

38 D. Deng, K. S. Novoselov, Q. Fu *et al.* Catalysis with two-dimensional materials and their heterostructures. *Nat. Nanotechnol.*, 11 (2016) 218-230.

39 Q. Zhang, S. Wang, R. Geng *et al.* Hydrogenation of CO_2 to higher alcohols on an efficient Cr-modified CuFe catalyst. *Appl. Catal., B*, 337 (2023) 123013.

40 A. N. Xu, S. F. Hung, A. Cao *et al.* Copper/alkaline earth metal oxide interfaces for electrochemical CO_2-to-alcohol conversion by selective hydrogenation. *Nat. Catal.*, 5 (2022) 1081-1088.

41 T. Fan, H. Liu, S. Shao *et al.* Cobalt Catalysts Enable Selective Hydrogenation of CO_2 toward Diverse Products: Recent Progress and Perspective. *J. Phys. Chem. Lett.*, 12 (2021) 10486-10496.

42 W. H. Li, X. W. Nie, H. Yang *et al.* Crystallographic dependence of CO_2 hydrogenation pathways over HCP-Co and FCC-Co catalysts. *Appl. Catal., B*, 315 (2022) 121529.

43 T. Witoon, J. Chalorngtham, P. Dumrongbunditkul, M. Chareonpanich & J. Limtrakul. CO_2 hydrogenation to methanol over Cu/ZrO_2 catalysts: Effects of zirconia phases. *Chem. Eng. J.*, 293 (2016) 327-336.

44 B. Ouyang, S. Xiong, Y. Zhang, B. Liu & J. Li. The study of morphology effect of Pt/Co_3O_4 catalysts for higher alcohol synthesis from CO_2 hydrogenation. *Appl. Catal., A*, 543 (2017) 189-195.

45 H. Kusama, K. Okabe, K. Sayama & H. Arakawa. Ethanol Synthesis by Catalytic Hydrogenation of CO_2 over $Rh-Fe/SiO_2$ Catalysts. *Energy*, 22 (1997) 343-348.

46 Y. Lou, F. Jiang, W. Zhu *et al.* CeO_2 supported Pd dimers boosting CO_2 hydrogenation to ethanol. *Appl. Catal., B*, 291 (2021) 120122.

47 S. N. Zhang, Z. X. Wu, X. F. Liu *et al.* Tuning the interaction between Na and Co_2C to promote selective CO_2 hydrogenation to ethanol. *Appl. Catal., B*, 293 (2021) 120207.

48 R. W. Yao, J. Wei, Q. J. Ge *et al.* Monometallic iron catalysts with synergistic Na and S for higher alcohols synthesis via CO_2 hydrogenation. *Appl. Catal., B*, 298 (2021) 120556.

49 K. An, S. R. Zhang, H. Wang *et al.* $Co^0 - Co^{\delta+}$ active pairs tailored by Ga-Al-O spinel for CO_2-to-ethanol synthesis. *Chem. Eng. J.*, 433 (2022) 134606.

50 J. Wang, T. Wang, Y. Xi *et al.* In-Situ-Formed Potassium-Modified Nickel-Zinc Carbide Boosts Production of Higher Alcohols beyond CH_4 in CO_2 Hydrogenation. *Angew. Chem. Int. Ed*, 62 (2023) e202311335.

51 C. Yang, R. Mu, G. Wang *et al.* Hydroxyl-mediated ethanol selectivity of CO_2 hydrogenation. *Chem. Sci.*, 10 (2019) 3161-3167.

52 D. Xu, M. Ding, X. Hong & G. Liu. Mechanistic Aspects of the Role of K Promotion on Cu–Fe-Based Catalysts for Higher Alcohol Synthesis from CO_2 Hydrogenation. *ACS Catal.*, 10 (2020) 14516-14526.

53 D. Xu, H. Yang, X. Hong, G. Liu & S. C. E. Tsang. Tandem Catalysis of Direct CO_2 Hydrogenation to Higher Alcohols. *ACS Catal.*, 11 (2021) 8978-8984.

54 S. A. Zhang, C. J. Huang, Z. L. Shao *et al.* Revealing and Regulating the Complex Reaction Mechanism of CO_2 Hydrogenation to Higher Alcohols on Multifunctional Tandem Catalysts. *ACS Catal.*, 13 (2023) 3055-3065.

55 J. Zhu, D. Ciolca, L. Liu *et al.* Flame Synthesis of $Cu/ZnO-CeO_2$ Catalysts: Synergistic Metal-Support Interactions Promote CH_3OH Selectivity in CO_2 Hydrogenation. *ACS Catal.*, 11 (2021) 4880-4892.

56 X. L. Li, G. L. Liu, D. Xu, X. L. Hong & S. C. E. Tsang. Confinement of subnanometric PdZn at a defect enriched ZnO/ZIF-8 interface for efficient and selective CO_2 hydrogenation to methanol. *J. Mater. Chem. A*, 7 (2019) 23878-23885.

57 A. Pustovarenko, A. Dikhtiarenko, A. Bavykina *et al.* Metal-Organic Framework-Derived Synthesis of Cobalt Indium Catalysts for the Hydrogenation of CO_2 to Methanol. *Acs Catal.*, 10 (2020) 5064-5076.

58 K. H. Sun, Z. G. Fan, J. Y. Ye *et al.* Hydrogenation of CO_2 to methanol over In_2O_3 catalyst. *J. CO_2 Util.*, 12 (2015) 1-6.

Chapter 4

Multifunctionality of Cu_2Zr_1-H-MCM-22 catalysts for the one-step CO_2 hydrogenation to DME

Dimethyl ether (DME) can be directly synthesized from CO_2 hydrogenation using bifunctional catalysts composed of methanol synthesis and dehydration sites. However, the performance is often limited by poor selectivity due to the incompatible integration of metal catalysts and solid acid zeolites, arising from mismatched proximity and interface interactions. In this work, a structured Cu_2Zr_1-H-MCM-22 catalyst system, comprising highly dispersed metallic Cu-Zr and H-MCM-22 zeolite, was designed to enable efficient CO_2 to DME conversion. The undesired interfacial effects, such as metal sintering and surface blockage of acidic zeolite sites were effectively mitigated by promoting spatial separation and high dispersion, thereby enhancing DME selectivity and catalyst stability, achieving a maximum space-time yield of 17.4 mmol·g_{cat}^{-1}·h^{-1}. $Si_xAl_yO_z$ performance correlations indicate that acid to base ratio, and appropriate Bronsted acid sites govern catalytic activity and selectivity. The findings presented herein offer valuable insights into the design of catalysts for the optimization of multifunctional systems in the context of CO_2 hydrogenation to DME.

4.1 Introduction

Catalytic CO_2 hydrogenation to value-added chemicals and fuels offers a route for CO_2 mitigation and the sustainable production of chemicals, with dimethyl ether (DME) being of particular interest as a versatile fuel, chemical feedstock, and efficient H_2 carrier[1,2] direct one-step CO_2 to DME hydrogenation promises enhanced efficiency and reduced process complexity. Conventional DME production employs a two-step process (methanol synthesis followed by dehydration)[3]. In order to achieve high DME selectivity, it is necessary to use catalysts that can facilitate the simultaneous synthesis of methanol from CO_2, the dehydration of methanol intermediates to DME, and the suppression of CO formation via the reverse water-gas shift (RWGS) reaction[4-6].

Cu-ZrO_x catalysts demonstrate elevated activity for the synthesis of methanol, a property attributable to the superior water tolerance of ZrO_2 in comparison to conventional supports like Al_2O_3[7-9]. Whilst the mechanical or precipitated mixing of MeOH synthesis and acid catalysts has demonstrated a promising level of productivity, the optimization of the interfacial contact between the catalytic components remains a pivotal challenge.

As demonstrated in **Figure 4-1**, the generation of C_1 products through CO_2 hydrogenation may proceed along two distinct routes upon the parameters. The initial step in this process is the RWGS pathway, which involves the initial hydrogenation of CO_2 into the *HOCO intermediate, followed by C-O bond cleavage to produce *CO species. These species have the capacity to either desorb directly as carbon monoxide or undergo further hydrogenation into *CH_xO species. The second route is known as the formate pathway, where CO_2 undergoes initial hydrogenation into *HCOO, followed by C-H bonding and C-O cleavage, resulting in *CH_xO species. Subsequent to this, *CH_xO can undergo further hydrogenation to form methanol.

In the formate pathway, CO_2 is adsorbed onto the catalyst surface, where it undergoes stepwise hydrogenation to form formate intermediates, which are subsequently reduced to methanol. This mechanism is dominant over catalysts such as the Cu-Zr system due to their ability to stabilize formate species and facilitate hydrogenation steps. Alternatively, the RWGS pathway involves the initial reduction of CO_2 to CO, followed by further hydrogenation to methanol. The selectivity observed between DME and methanol is determined by the interplay of the dehydration of methanol species.

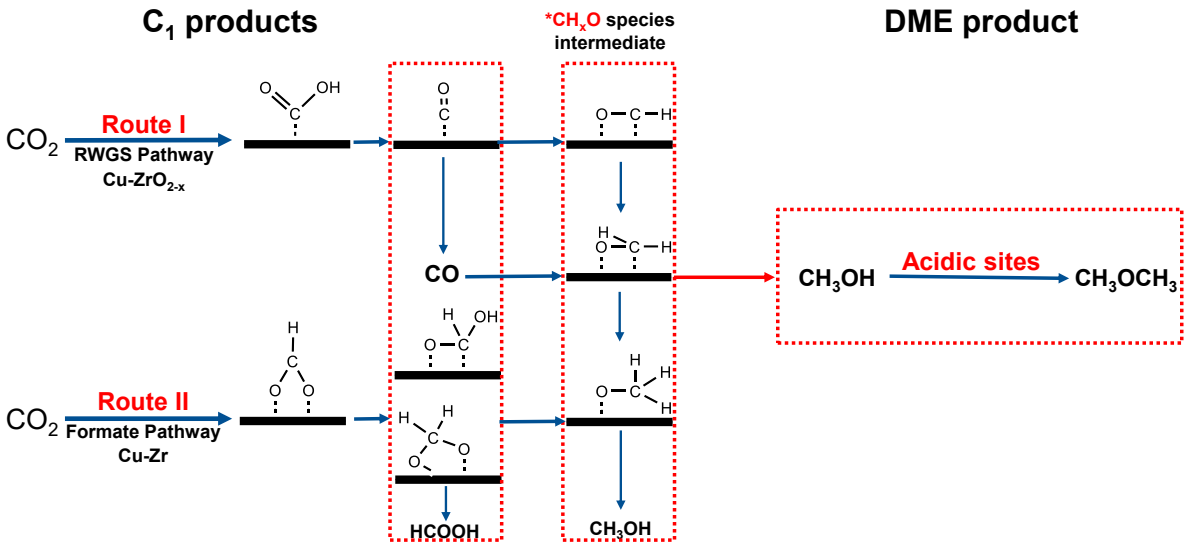

Figure 4-1. Catalytic mechanism of dimethyl ether (DME) synthesis

This pathway is frequently associated with catalysts that exhibit strong CO activation capability, such as Cu-Fe or Co-based systems. While RWGS contributes to CO formation as a byproduct, its suppression is imperative to enhance methanol selectivity and improve overall DME yield. Following the formation of methanol intermediate, a process of dehydration occurs on the acidic component of the catalyst. The dehydration process is understood to follow a bimolecular mechanism, whereby methanol intermediate molecules interact on Brønsted acid sites to form DME and water. The efficiency of this step is contingent on the structure and density of acid sites, which can be modified by adjusting the zeolite and the Si/Al ratio. It has been demonstrated that comparable higher acidity promotes faster dehydration but may also lead to undesired side reactions, such as the formation of hydrocarbons via methanol to hydrocarbon (MTH) pathways.

In order to address this issue, the present study investigates a chemically integrated Cu_2Zr_1-H-MCM-22 catalyst, in which methanol synthesis and dehydration functionalities form a homogeneous system[10-14]. The present study proposes a methodology for the systematic variation of metal loading and support properties[15-18], with the objective of modulating catalyst reduction behavior and interface characteristics to steer CO_2 hydrogenation selectivity toward DME. Through in-depth mechanistic investigations, it concluded that the intermediate methanol was transferred to the zeolite and that this process favored DME production. The investigation of the influence of different supports on the physicochemical properties and catalytic performance of these materials was undertaken with the aim of enhancing CO_2 hydrogenation efficiency toward DME. The findings presented herein offer valuable insights into catalyst design strategies for the optimization of multifunctional systems in sustainable CO_2 conversion

and offer a strategic framework for the design of more efficient catalytic systems, paving the way for advancements in CO_2 to DME conversion and broader applications in renewable energy technologies.

4.2 Methods

4.2.1 Chemicals and materials

Copper nitrate ($Cu(NO_3)_2 \cdot 3H_2O$) and zirconium nitrate ($Zr(NO_3)_4 \cdot 5H_2O$), aluminum nitrate ($Al(NO_3)_3 \cdot 9H_2O$), 1,8-Diazabicyclo[5.4.0]undec-7-ene (DBU) and tetraethoxysilane (TEOS) were purchased from Sigma-Aldrich and used without further purification. H-ZSM-5 (11.5:1), MCM-22 (11:1), MOR (20:1), SiO_2, Al_2O_3 were purchased from the same "Zeolyst" company. Deionized (DI) water (18.2 $M\Omega \cdot cm^{-1}$) was used to prepare all aqueous solutions.

4.2.2 Sample preparation

4.2.2.1 Coprecipitation method to synthesis Cu_2Zr_1Ox, $Si_{20}Al_1O_x$, $Si_{10}Al_1O_x$, $Si_1Al_1O_x$

The process of coprecipitation of the methanol catalyst precursors is achieved by utilizing a DBU precipitation agent. A pure DBU solution was added in droplets to an aqueous solution (50 mL) of copper and zirconium nitrate solution (Cu/Zr = 2:1) in a slow and constant mode under vigorous stirring. The pH of the solution was kept around 10 with continuous additions of DBU to ensure the formation of hydroxyl precipitation. During the precipitation step, the solution got an intense blue color. Following the precipitation process, the sky-blue solid was maintained at 298 K and then aged at room temperature for 12 hours. The resultant precipitation was subjected to a process of washing with distilled water, followed by drying at 333 K overnight and then calcined at 673 K for 5 h. $Si_{20}Al_1O_x$, $Si_{10}Al_1O_x$, $Si_1Al_1O_x$ was accomplished through the utilization of the aforementioned precipitation method with different ratio of TEOS and $Al(NO_3)_3$ mixture solution exhibiting a variable ratio (Si:Al = 20:1, 10:1, 1:1).

4.2.2.2 Coprecipitation method to synthesis 30wt% Cu_2Zr_1-SiO_2, 30wt% Cu_2Zr_1-H-MOR, 30wt% Cu_2Zr_1-H-ZSM-5, 30wt% Cu_2Zr_1-Al_2O_3, 30wt% Cu_2Zr_1-$Si_1Al_1O_x$, 30wt% Cu_2Zr_1-H-MCM-22

The process of coprecipitation of the methanol catalyst precursors by DBU and deposition on the zeolite particles in an aqueous medium is the subject of this study. A pure DBU solution was added in the form of droplets to an aqueous solution (50 mL) of copper and zirconium nitrate precursors solutions with different zeolite supports that had been finely dispersed under vigorous stirring. The pH of the solution was maintained at approximately 10, with continuous additions of DBU to ensure the formation of hydroxyl precipitation on the support. Following

the precipitation process, the sky-blue solid was maintained at 298 K and subsequently aged at room temperature for 12 h. The resulting precipitation was then subjected to a washing process with distilled water, followed by a drying step at 333 K overnight and then calcined at a temperature of 673 K for a duration of 5 h.

4.2.2.3 Coprecipitation method to synthesis different loading amount of $Cu_2Zr_1O_x$ on H-MCM-22

The process of coprecipitation of the methanol catalyst precursors by DBU and deposition on the zeolite particles in an aqueous medium is the same as the previous work. By changing the different amounts of copper and zirconium nitrate precursors solutions with different zeolite supports, the different 5wt%, 10wt%, 20wt%, 30wt% $Cu_2Zr_1O_x$ loading on H-MCM-22 catalysts were synthesized.

4.2.2.4 Physical mixed method to synthesis 30w% $Cu_2Zr_1O_x$ and H-MCM-22 physical mixed catalyst

The process of synthesizing 30w% $Cu_2Zr_1O_x$ and H-MCM-22 physical mixed catalyst involved grinding the $Cu_2Zr_1O_x$ and H-MCM-22 powders together, after which the mixture was sieved to the desired size for further analysis.

4.2.3 Catalyst testing

The catalytic performance of all catalysts was evaluated within a high-pressure, continuous-flow, fixed-bed reactor. The mixture comprised 20 mg of Cu_2Zr_1-H-MCM-22 catalysts (250-300цm) and 600 mg of SiC (150-250цm). The mixture was pretreated in a $2H_2/N_2$ atmosphere at 310 °C in a flow of 50 mL·min^{-1} for a duration of 0.5 h. The temperature was then cooled to 300 °C, and $CO_2/H_2/N_2$ (18/72/10, 5MPa) was introduced with a flow of 50 mL·min^{-1}. Subsequent to the stabilization of pressure and temperature, the gas flow was maintained at 50 mL·min^{-1} and an Agilent chromatograph equipped with a flame ionization detector and a tuning Methanizer was used to analyze products online every 4 h. The catalytic performance of the catalysts was evaluated in terms of CO_2 conversion, product selectivity and space-time yield (STY).

4.2.4 The computational formulas were as follows:

CO_2 conversion, C_{CO2} (%) = $(X_{CO2,\,in} - X_{CO2,\,out})/X_{CO2,\,in} \times 100\%$

Product selectivity, Sel% = $X_{product}/(X_{CO2,\,in} - X_{CO2,\,out}) \times 100\%$

STY of DME, STY_{DME} (mmol·g_{cat}^{-1}·h^{-1}) = $F_{CO2,\,in} \times C_{CO2} \times Sel_{DME} \times 1{,}000/W_{cat}$, where $X_{CO2,\,in}$ and $X_{CO2,\,out}$ are the mole fractions of CO_2 in pristine and exit mixed gas, respectively; $F_{CO2,\,in}$ (mol·h^{-1}) is the molar flow rate of CO_2 in pristine mixed gas; W_{cat} (g) is the weight of catalyst.

Space velocity ($L \cdot g_{cat}^{-1} \cdot h^{-1}$) = ($V_{flow}/W_{cat}$) * 0.06

Space time (s) = (V_{cat}/V_{flow}) * 60, where V_{flow} (mL/min) is the total flow rate of the pristine mixed gas; W_{cat} (g) is the weight of catalyst; V_{cat} (mL) is the volume of catalyst

4.3 Characterizations

4.3.1 In-situ XRD

The crystalline structure of the catalyst was determined using powder X-ray diffraction. The X-ray diffraction patterns were collected using a PANalytical Empyrean System diffractometer with Cu Kα radiation (λ = 0.1542 nm), operating at 45 kV/40 mA, using a nickel Kβ filter and a solid-state detector.

4.3.2 H_2 TPR

H_2 temperature-programmed reduction (TPR) was carried out on a Chemstar instrument. Prior to TPR measurement, 100 mg of the catalyst was flushed with Ar (>99.999%) at 150 °C for 1 h then cooled to 50 °C. Subsequently, the temperature was increased from 50 to 500 °C at a rate of 2 °C·min^{-1} under H_2/Ar (volume ratio 1/9, flow rate 30 mL·min^{-1}). The temperature was then maintained at 500 °C for a period of 30 min. The H_2 concentration was monitored by means of a thermal conductivity detector (TCD). The H_2-TPR profile was recorded as H_2 consumption versus reduction temperature.

4.3.3 BET

N_2 physisorption experiments were conducted on a Quantachrome Sulfur instrument, a device designed specifically for the measurement of surface area and porosity. The sample was degassed at 310 °C for 1 h, followed by N_2 adsorption at −196 °C. The BET surface area was determined by means of the Brunauer-Emmett-Teller (BET) method.

4.3.4 SEM

The structural properties of the synthesized Cu_2Zr_1-H-MCM-22 catalysts were analyzed using a scanning electron microscopy (SEM) to assess crystallinity and particle size, respectively. Scanning electron microscopy (SEM) images of the Cu_2Zr_1-H-MCM-22catalyst confirmed the homogeneous distribution of cobalt, copper and zirconia species over the Cu_2Zr_1-H-MCM-22 catalyst. The analysis of the particle size distribution indicated an average particle size of approximately 100 nm for the metal oxide particles, which is consistent with the results obtained by SEM.

4.4 Results and discussion

4.4.1 Compare the influence of different supports and loadings amount of the $Cu_2Zr_1O_x$

The varying quantities of Bronsted acid and methanol intermediates have been demonstrated to exert a significant influence on the CO_2 conversion, products selectivity, dehydrogenation and further C-O bond cleavage, which lead to the different space time yield (STY) of DME. The composition of Cu_2Zr_1-zeolite exerts a pivotal influence on the DME formation process during CO_2 hydrogenation, through the modulation of catalytic activity, selectivity, and reaction pathways. The interplay between $Cu_2Zr_1O_x$ and different supports has been shown to influence the balance between methanol, DME, and other products where reaction passes through methanol intermediate formation and dehydrated steps. $Cu_2Zr_1O_x$ has been shown to act as methanol intermediates producer, with the capacity to transfer methanol intermediates to zeolite support. The loading of $Cu_2Zr_1O_x$ on zeolite is of pivotal importance in order to maximize DME production, whereas excessive $Cu_2Zr_1O_x$ favors DME selectivity. It is imperative to optimize the composition of the Cu_2Zr_1-zeolite to ensure the effective production of DME and the selective hydrogenation of CO_2.

The preparation of the analyzed catalysts involved a coprecipitation method, followed by an overnight drying process and 400 °C calcination for a duration of 5 h. Prior to the reaction, the pristine catalysts were reduced by 30% H_2 at 310 °C for a duration of 0.5 h. During the catalytic reaction, the CO_2 conversion of the catalysts was maintained below 5%, far away from the equilibrium concentration of methanol and DME in order to approximate the intrinsic activity. In the presence of a range of catalysts with varying support, the 30wt% $Cu_2Zr_1O_x$ with H-MCM-22 catalyst demonstrated the highest space time yield (STY) of DME at a rate of 14 $\mathrm{mmol}\cdot g_{cat}^{-1}\cdot h^{-1}$, surpassing the levels exhibited by the SiO_2, H-MOR, H-ZSM-5, Al_2O_3, $Si_1Al_1O_x$ catalysts and the physical mixed 30wt% $Cu_2Zr_1O_x$ and H-MCM-22 catalyst (**Figure 4-2**).

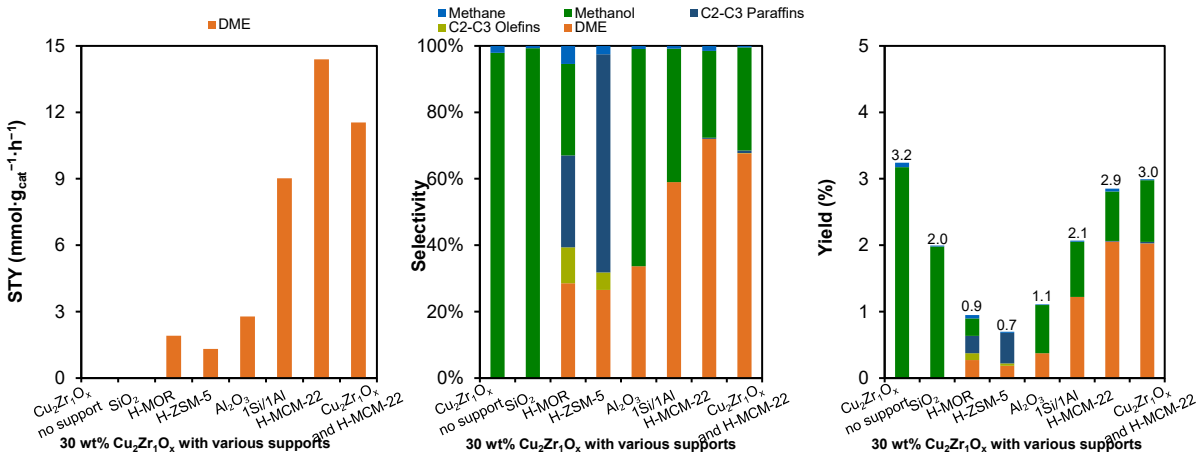

Figure. 4-2. (**Left**) DME space time yield (STY) for $Cu_2Zr_1O_x$, 30 wt% $Cu_2Zr_1O_x$ on different supports, 30 wt% $Cu_2Zr_1O_x$ and H-MCM-22 physical mixed catalyst. (**Center**) Catalytic performance of $Cu_2Zr_1O_x$, 30 wt% $Cu_2Zr_1O_x$ on different supports, 30 wt% $Cu_2Zr_1O_x$ and H-MCM-22 physical mixed catalyst. (**Right**) Catalytic yield for $Cu_2Zr_1O_x$, 30 wt% $Cu_2Zr_1O_x$ on different supports, 30 wt% $Cu_2Zr_1O_x$ and H-MCM-22 physical mixed catalyst. All the experiments are regarded as CO free and analyzed at 300°C, 5.0 MPa, space velocity = 150 $L \cdot g_{cat}^{-1} \cdot h^{-1}$, $H_2/CO_2 = 4$.

A comparison of the 30wt% Cu_2Zr_1-H-MCM-22 catalyst with other supports has been undertaken, resulting in a significant improvement of the overall selectivity for DME to 72% with CO free. It can thus be concluded that the combination of the H-MCM-22 with a suitable Bronsted acid site and a methanol formation catalyst $Cu_2Zr_1O_x$ is of crucial importance in the construction of an excellent catalyst for the synthesis of DME from CO_2.

To evaluate the role of $Cu_2Zr_1O_x$ in the Cu_2Zr_1-H-MCM-22 system, the performance of a different loading ratio of $Cu_2Zr_1O_x$ catalyst was compared (**Figure 4-3**).

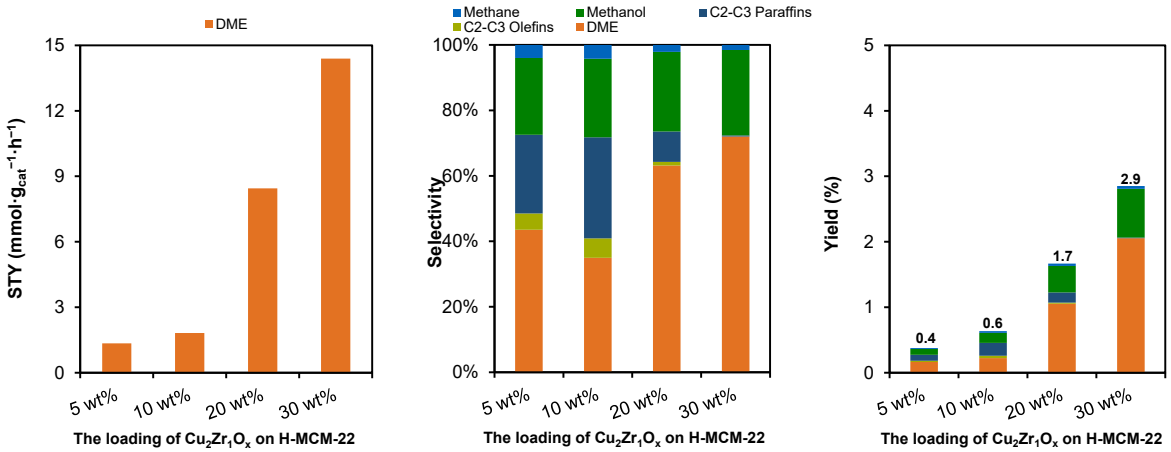

Figure. 4-3. (**Left**) DME space time yield (STY) for different loading amount of $Cu_2Zr_1O_x$ on H-MCM-22. (**Center**) Catalytic performance on x wt% Cu_2Zr_1-H-MCM-22. (**Right**) Catalytic yield for x wt% Cu_2Zr_1-H-MCM-

22. All the experiments are regarded as CO free and analyzed at 300°C, 5.0 MPa, space velocity = 150 $L \cdot g_{cat}^{-1} \cdot h^{-1}$, $H_2/CO_2 = 4$.

It is evident that an increase in the $Cu_2Zr_1O_x$ loading ratio results in an increase in the space time yield (STY) of DME with the highest 72% selectivity and the yield of DME and methanol reach 2.9%. The Cu-Zr interface has been shown to facilitate the initial C-O bond cleavage in CO_2, forming methanol intermediate that is crucial for C_1 product formation. The presence of Bronsted acid sites in H-MCM-22 has been demonstrated to promote C-C coupling between methanol and methanol species, thereby increasing the selectivity for product DME. The combination of these functionalities in the Cu_2Zr_1-H-MCM-22 system engenders a favorable reaction environment that is conducive to enhanced DME production, whilst concomitantly suppressing undesired by-products.

With regard to the SEM results (**Figure S4-10**) of the surface structure of $Si_1Al_1O_x$ and 30wt% Cu_2Zr_1-$Si_1Al_1O_x$, these establish the porous stacked-plate structure of Cu-Zr loading on the zeolite. Meanwhile, the surface areas of H-MCM-22, 30wt% Cu_2Zr_1-H-MCM-22, $Si_1Al_1O_x$ and 30wt% Cu_2Zr_1-$Si_1Al_1O_x$ were found to be 281.52 $m^2 \cdot g^{-1}$ and 299.38 $m^2 \cdot g^{-1}$, 350.45 $m^{2.g-1}$ and 354.46 $m^2 \cdot g^{-1}$, respectively (**Figure S4-11 and Table S4-1**). The amorphous Si-Al support exhibits partial meso-porosity, in contrast to the purely microporous structure of H-MCM-22. This structural distinction indicates that mesopore presence, and consequently pore size, does not appear to be the primary factor influencing catalytic performance in the direct CO_2 to DME synthesis reaction.

4.4.2 Optimizing the parameters to increase DME formation

It is imperative to acknowledge the pivotal role that both the reactant concentration and retention time play in facilitating the progression of the reaction by adjusting the intermediates concentation. It has been demonstrated that elevated pressures enhance the adsorption and activation of CO_2 and H_2 on the catalyst surface, leading to increased reaction rates and higher CO_2 conversion. From a thermodynamic perspective, an increase in pressure results in a shift towards the formation of DME, owing to the enhanced propensity for both methanol synthesis and its subsequent dehydration. Furthermore, an increase in pressure has been shown to promote C-C coupling reactions and suppress the desorption of CO, thereby directing surface-bound metahnol intermediates towards further hydrogenation rather than side reactions such as methanation.

An experimental investigation was conducted to ascertain the impact of pressure on the performance of a catalyst. To this end, the total pressure was systematically varied from 10 to 50 bar, while maintaining constant reaction at a temperature of 300 °C and a H_2/CO_2 ratio of 4:1 (**Figure 4-4**).

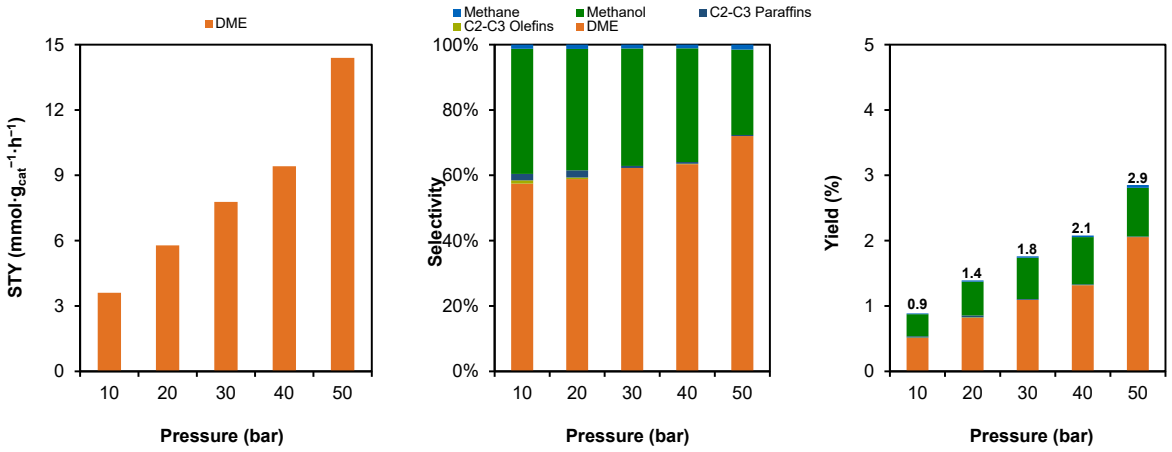

Figure. 4-4. (**Left**) DME space-time yield (STY) for different pressure. (**Center**) Catalytic performance on 30 wt% Cu_2Zr_1-H-MCM-22 with pressure shift. (**Right**) Catalytic yield for 30 wt% Cu_2Zr_1-H-MCM-22 with pressure shift. All the experiments are regarded as CO free and analyzed at 300°C, 1.0-5.0 MPa, space velocity = 150 $L \cdot g_{cat}^{-1} \cdot h^{-1}$, $H_2/CO_2 = 4$.

As the pressure increased, both CO_2 conversion and DME selectivity exhibited significant improvement. It is noteworthy that the formate pathway became more prominent, correlating with enhanced methanol intermediate formation. The space time yield (STY) of DME also increased progressively with pressure, reaching an optimum at approximately 50 bar, where the highest DME selectivity and CO_2 conversion were observed. At a pressure of 10 bar, the CO_2 conversion was recorded at 0.9%, while the DME selectivity attained 57.5%. The low pressure is likely to limit the absorption and activation of CO_2 molecules on the catalyst surface. As the pressure increased to 50 bar, both conversion (2.9%) and DME yield (14.4 $mmol \cdot g_{cat}^{-1} \cdot h^{-1}$) reached their highest values, indicating an optimal interaction between CO_2, hydrogen, and the catalyst surface. As illustrated in **Figure S4-7**, the $Si_1Al_1O_x$ catalyst also exhibits a similar trend, which can be deduced from the data that higher pressure appears to promote the reaction.

A reduction in space time has been shown to be an effective strategy for suppressing Fischer-Tropsch synthesis (FTS) type reactions, while concomitantly enhancing the formate pathway over the Cu_2Zr_1-H-MCM-22 catalyst. As demonstrated in **Figure 4-5**, a reduction in the space time leads to a significant improvement in dimethyl ether (DME) productivity, with

a maximum space time yield (STY) of approximately 17.5 $mmol \cdot g_{cat}^{-1} \cdot h^{-1}$, which significantly exceeds that of benchmark catalysts operating at higher space times.

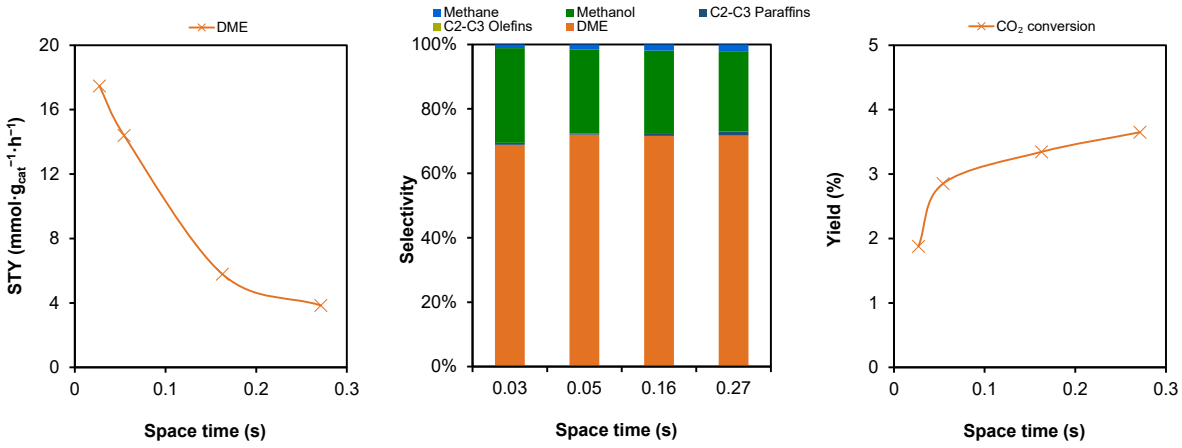

Figure. 4-5. (**Left**) DME space time yield (STY) for adjusted space time. (**Center**) Catalytic performance on 30 wt% Cu_2Zr_1-H-MCM-22 with space time shift. (**Right**) Catalytic yield for 30 wt% Cu_2Zr_1-H-MCM-22 with space time shift. All the experiments are regarded as CO free and analyzed at 300°C, 5.0 MPa, space time = 0.03-0.27 s, $H_2/CO_2 = 4$.

It is noteworthy that the selectivity towards DME attains a maximum of 68.9% under these optimal conditions and exhibits remarkable stability, maintaining approximately 70% across a range of space time, indicating robust catalytic performance and product stability. For the purpose of comparison, analogous trends were observed in the $Si_1Al_1O_z$ catalyst system (**Figure S4-8)**, which exhibited a comparatively lower DME space time yield (STY). With regard to the yield versus conversion, **Figure S4-9** provides further confirmation. The products of methane, C_2-C_3 paraffins and methanol yield a comparable slight increase trend for Cu_2Zr_1-H-MCM-22 and Cu_2Zr_1-$Si_1Al_1O_x$, while a gradual increase in DME is observed for both of them with increasing the CO_2 conversion. The findings demonstrate the superior efficiency of the catalysts in channeling the CO_2 hydrogenation reaction towards DME formation under kinetically favorable, a lower space time improves the space time yield, and a higher CO_2 conversion promotes the DME yield.

4.4.3 Optimizing the Bronsted acid sites to increase the DME formation

The influence of the Bronsted acid sites on the final selectivity for methanol and DME is a consequence of the varying ratio of Si/Al in the $Si_xAl_yO_z$ catalysts. As demonstrated by the results obtained, a gradual increase in the chemical composition of the $Si_xAl_yO_z$ is observable, given the selective atomic Si/Al ratio (20:1-1:1) exhibited by the hybrids (**Figure 4-6**).

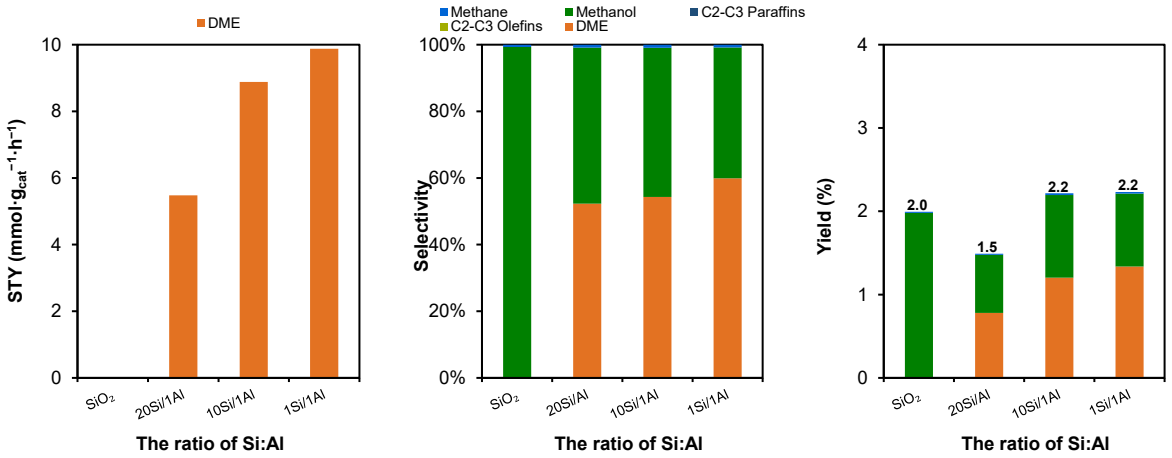

Figure. 4-6. (**Left**) DME space time yield (STY) for 30 wt% $Cu_2Zr_1O_x$ with different ratio of Si/Al on $Si_xAl_yO_z$ catalyst. (**Center**) Catalytic performance for 30 wt% $Cu_2Zr_1O_x$ with different ratio of Si/Al on $Si_xAl_yO_z$ catalyst. (**Right**) Catalytic yield for 30 wt% $Cu_2Zr_1O_x$ with different ratio of Si/Al on $Si_xAl_yO_z$ catalyst. All the experiments are regarded as CO free and analyzed at 300°C, 5.0 MPa, space velocity = 150 $L \cdot g_{cat}^{-1} \cdot h^{-1}$, $H_2/CO_2 = 4$.

Beyond acidity, the Si/Al ratio exerts a significant influence on hydrophilicity and framework stability, consequently impacting reaction kinetics. A high Si/Al ratio has been shown to result in a more hydrophobic framework, thereby improving water tolerance and minimizing competitive adsorption effects that could hinder catalytic performance. Meanwhile, a low Si/Al ratio, while advantageous for strong acidity, may result in coke deposition and catalyst deactivation due to excessive hydrocarbon formation and pore blockage, which underscores the limited efficacy of optimizing the Si/Al ratio to achieve a balance between acidity, stability, and product selectivity. Further insights from in situ spectroscopy and kinetic modelling could provide a deeper mechanistic understanding of how zeolite acidity governs CO_2 hydrogenation pathways, enabling rational catalyst design for sustainable DME production.

4.4.4 Reaction stability and kinetics analysis for promoting DME STY

The present study investigates the stability of activated Cu_2Zr_1-H-MCM-22 under conditions of 50 bar (H_2:CO_2 = 4:1) with a space velocity of 150 $L \cdot g_{cat}^{-1} \cdot h^{-1}$ at 300 °C. Following a duration of 111 hours of operation, the selectivity for alcohols and paraffins exhibited a plateau phase (**Figure 4-7**). It was demonstrated that activated Cu_2Zr_1-H-MCM-22 exhibited sufficient stability during the pressure-induced CO_2 hydrogenation process under 50 bar.

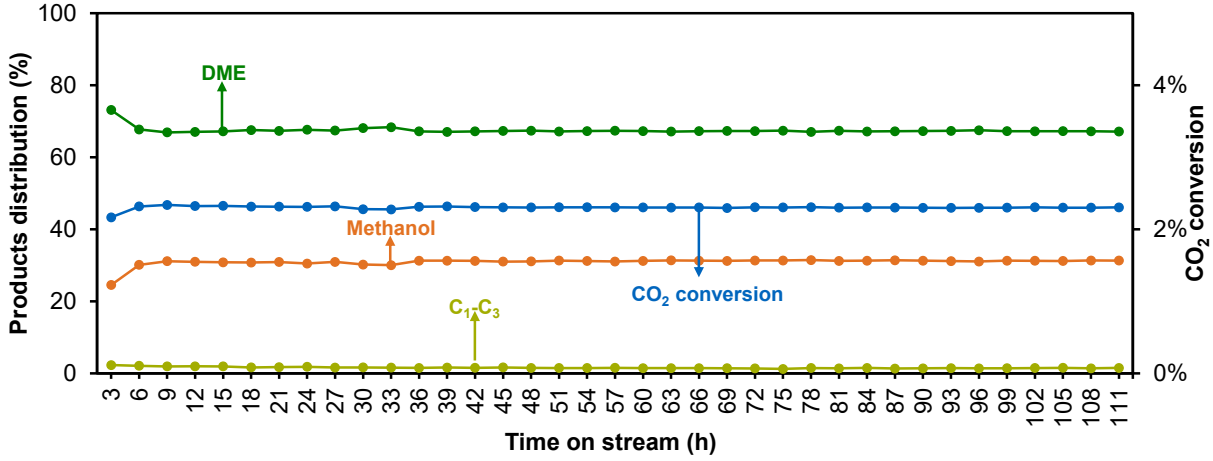

Figure 4-7. The stability of catalytic yield and selectivity of the products (methanol, Dimethyl ether and C_1-C_3 paraffins HCs) of 30 wt% Cu_2Zr_1-H-MCM-22. All the experiments are regarded as CO free and analyzed at 300°C, 5.0 MPa, space velocity = 150 $L \cdot g_{cat}^{-1} \cdot h^{-1}$, $H_2/CO_2 = 4$

The higher reaction orders of Cu_2Zr_1-H-MCM-22 (CO_2 $\alpha = 0.18$ and H_2 $\beta = 0.60$) indicate that the activation of both reactants plays a more critical role in the rate-determining step. This enhanced activation accelerates the formation of methanol intermediates, which subsequently undergo dehydration on the acid sites of H-MCM-22, ultimately leading to the preferential formation of DME. Compared to the reference catalyst, the reduced reaction orders of Cu_2Zr_1-$Si_1Al_1O_x$ (CO_2 $\alpha = 0.15$ and H_2 $\beta = 0.39$ imply that reactant activation barriers are largely overcome. As a result, the rate-determining step likely shifts toward intermediate conversion and methanol dehydration, highlighting the synergistic role of zeolite functionality in promoting DME selectivity (**Figure 4-8**). A comparison of Cu_2Zr_1-$Si_1Al_1O_x$ and Cu_2Zr_1-H-MCM-22 reveals that the limited availability of hydrogen hinders complete hydrogenation of CO_2 derived intermediates at a low H_2/CO_2 ratio of 1:4 (**Figure S4-1, S4-2 and S4-4, S4-5**), resulting in a low overall CO_2 conversion of 0.3% to 0.3%, and a dimethyl ether (DME) space time yield (STY_{DME}) of only 3.3 to 3.5 $mmol \cdot g_{cat}^{-1} \cdot h^{-1}$.

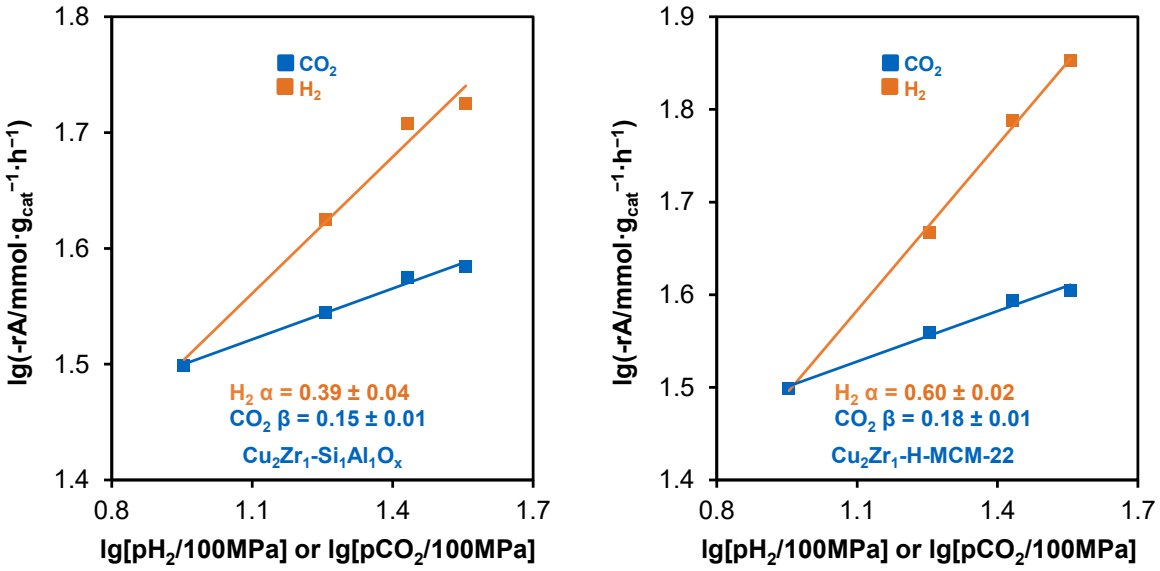

Figure 4-8. (**Left**) CO_2 and H_2 overall reaction orders for 30 wt% Cu_2Zr_1-$Si_1Al_1O_x$ catalyst. (**Right**) CO_2 and H_2 overall reaction orders for 30 wt% Cu_2Zr_1-H-MCM-22 catalyst. All the experiments are analyzed at 300°C, 5.0 MPa, space velocity = 150 $L \cdot g_{cat}^{-1} \cdot h^{-1}$, H_2/CO_2 = 1/4-4/1. A: the total conversion of CO_2.

It can be deduced from these findings that insufficient hydrogen restricts the formation and subsequent transformation of key methanol intermediates, thereby suppressing DME production. Conversely, an augmentation of the H_2/CO_2 ratio to 4:1 resulted in a substantial enhancement in both hydrogenation efficiency and DME yield. In the present study, the STY_{DME} demonstrated a maximum range of 9.9 to 14.4 $mmol \cdot g_{cat}^{-1} \cdot h^{-1}$ with a CO_2 conversion of 2.2% to 2.9%, underscoring the crucial role of excess hydrogen in facilitating complete reduction of surface bound intermediates and their effective dehydration over the acidic sites of zeolite. The elevated reaction rate observed over Cu_2Zr_1-$Si_1Al_1O_x$ is highly dependent on the reactant concentrations, suggesting that the **adsorption and activation of** H_2 and CO_2 constitute the predominant **kinetic limitations**. In contrast, the Cu_2Zr_1-H-MCM-22 catalyst facilitates the concurrent adsorption and activation of both reactants, thereby diminishing the rate sensitivity to reactant concentration and resulting in a **lower apparent reaction order**. This behavior implies that the introduction of the H-MCM-22 framework effectively mitigates the adsorption-related kinetic barriers, promoting a more efficient catalytic pathway for CO_2 hydrogenation.

The multivariable analysis revealed that the optimal condition for DME selectivity occurs at 300 °C, 50 bar, and an H_2/CO_2 ratio of 4:1. The joint influence of these parameters is

conducive to the sequential conversion of CO_2 to methanol and its subsequent dehydration to DME. The interplay between thermal input, hydrogen availability, and system pressure underscores the imperative for integrated process optimization to direct the reaction pathway towards the synthesis of high value oxygenates, while concurrently minimizing byproduct formation.

It has been demonstrated that at moderate temperatures (220-300 °C), there is an optimal balance between CO_2 activation and hydrogenation is achieved, enhancing C-C coupling and promoting DME formation. This range also facilitates the reverse water-gas shift (RWGS) reaction, leading to the formation of CO, which can act as an intermediate for further chain growth. From a kinetic perspective, temperature exerts a significant influence on the rate-determining step of CO_2 hydrogenation, thereby affecting the equilibrium between CO production, methanol formation, and DME synthesis. It is therefore vital to optimize the reaction temperature in order to achieve high CO_2 conversion while maintaining selectivity towards the desired DME product. In order to elucidate the role of the zeolite component in catalytic performance, the specific activity of the catalyst was evaluated as a function of reaction temperature in the CO_2 to DME hydrogenation reaction. As demonstrated in **Figure S4-3 and S4-6**, both the CO_2 conversion and DME formation rates demonstrate a linear dependence on temperature, thus emphasizing the thermally driven nature of the process. The apparent activation energies (Ea) for DME and CH_3OH generation were estimated to be 52 $kJ \cdot mol^{-1}$ and 19 $kJ \cdot mol^{-1}$, respectively, on Cu_2Zr_1-$Si_1Al_1O_x$ compared to 43 $kJ \cdot mol^{-1}$ and 39 $kJ \cdot mol^{-1}$, respectively, on Cu_2Zr_1-H-MCM-22, revealing that DME formation is more challenging than that of methanol (**Figure 4-9**).

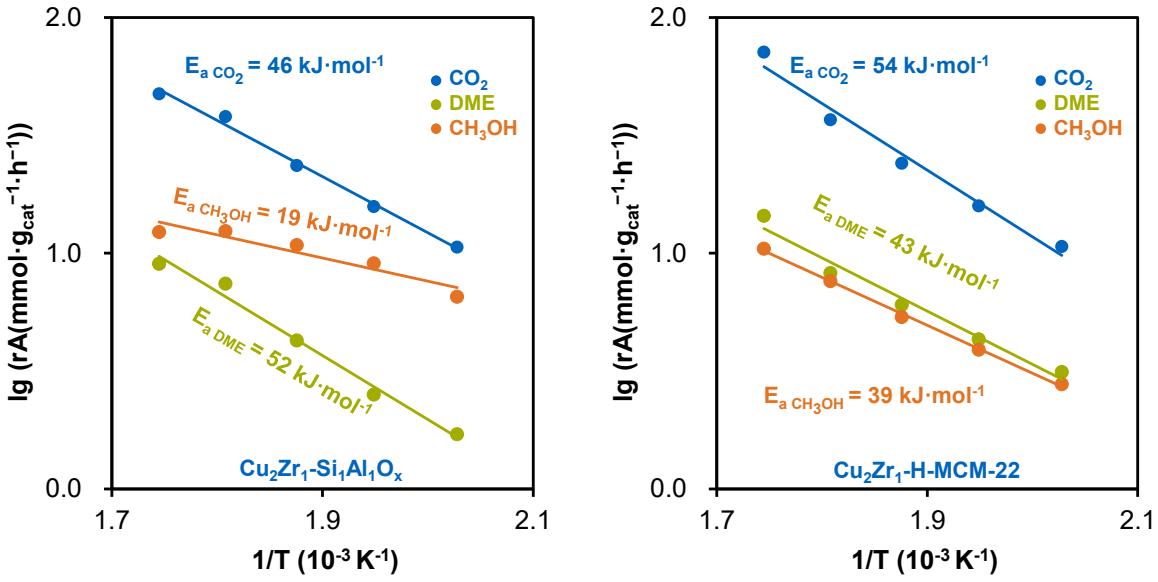

Figure 4-9. (**Left**) Apparent activation energies for overall CO_2, DME and CH_3OH formation on 30 wt% $Cu_2Zr_1Si_1Al_1O_x$. (**Right**) Apparent activation energies for overall CO_2, DME and CH_3OH formation on 30 wt% Cu_2Zr_1-H-MCM-22. All the experiments are analyzed at 220-300°C, 5.0 MPa, space velocity = 150 $L \cdot g_{cat}^{-1} \cdot h^{-1}$, H_2/CO_2 = 4:1.

As the temperature increased, the system demonstrated enhanced reactivity. The peak of the ethanol yield occurred at 300 °C, with a value of 14.4 $mmol \cdot g_{cat}^{-1} \cdot h^{-1}$ Concurrently, the productivity of DME attained its maximum at a maximum with a CO_2 conversion of 2.9 %. This enhancement in performance is attributed to the advantageous synergy between the Cu-Zr interface, which is responsible for C-O bond activation, and the acid sites of H-MCM-22, which facilitate the dehydration of methanol intermediates into DME.

The subsequent intermediate analysis was conducted using in situ diffuse reflectance infrared fourier transform spectroscopy (DRIFTS) experiments to probe the formation and evolution of surface intermediates involved in the hydrogen-assisted synthesis (HAS) reaction. The present study systematically examined the role of H-MCM-22 support in modulating intermediate species was systematically examined, as illustrated in **Figures 4-10**.

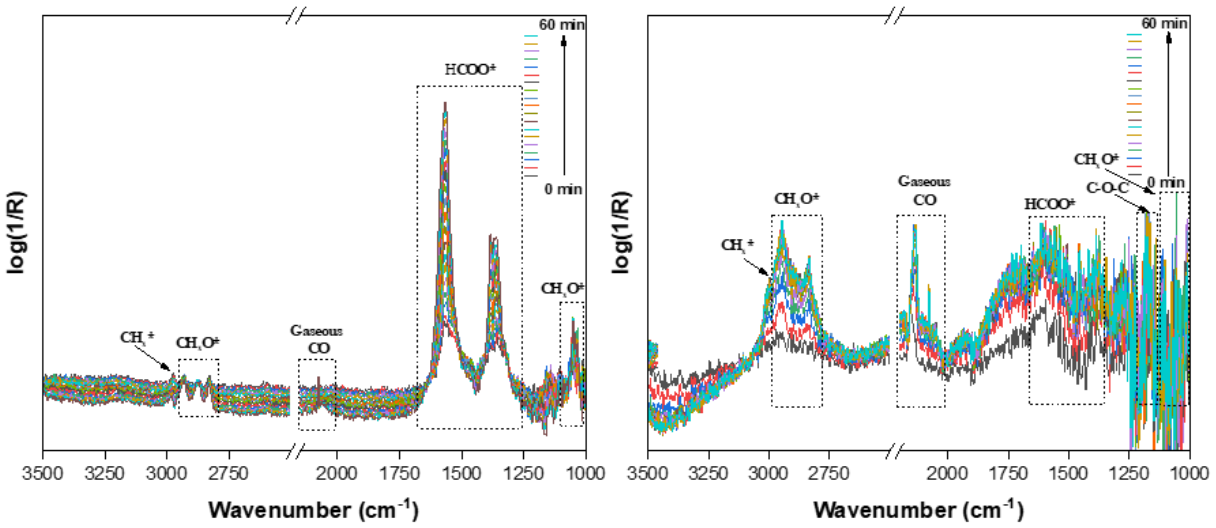

Figure 4-10. In situ DRIFTS spectra of the $CO_2 + H_2$ reaction over the $Cu_2Zr_1O_x$ and Cu_2Zr_1-H-MCM-22 samples. (**Left**) dynamic spectra at the region of 1000-3500 cm^{-1} of $Cu_2Zr_1O_x$ and (**Right**) dynamic spectra at the region of 1000-3500 cm^{-1} of Cu_2Zr_1-H-MCM-22 under the reaction conditions of 2 MPa, H_2/CO_2 = 4 and 523 K.

Distinct vibrational bands corresponding to $*CH_x$, $*CH_xO$ and *HCOO, as well as adsorbed CO species were observed, indicating the participation in C-C coupling pathways leading to C-O-C intermediate and DME formation (**Table S4-2**). Time-resolved DRIFTS spectra recorded at 250 °C revealed the progressive intensification of bands attributed to $*CH_x$,

*CH_xO and *HCOO, as well as adsorbed CO with increasing reaction time, thereby supporting a CO mediated mechanism. The peaks at 1800-1900, 1900-2000, 2176, 2110, and 2085 cm^{-1} for adsorbed CO* appear and the amount of CO* increases rapidly within the initial 20 min, indicating the formation of CO at 250 °C. It is proposed that H-MCM-22 support enhances the coupling of *CH_xO (1070-1082, 2824-2826, 2937-2941, 1270 and 1034 cm^{-1}) intermediate, C-O-C (1100-1200 cm^{-1}) which are subsequently coupled into DME, highlighting the critical function of Bronsted acid sites in steering the reaction selectivity towards DME.

The active sites will be the surface of Cu-Zr for the synthesis of methanol and the Bronsted acid sites of H-MCM-22 for the intermediate's dehydration. The reduction properties were initially determined by examining the in-situ XRD patterns of as-prepared 30wt% Cu_2Zr_1-H-MCM-22 in H_2 atmosphere. The X-ray diffraction (XRD) patterns of the synthesized catalysts exhibited distinct peaks that corresponded to the phase of zeolite H-MCM-22 and CuO catalysts (**Figure 4-11**). As the temperature increased in the 30wt% Cu_2Zr_1-H-MCM-22 sample with hydrogen flow, a slight shift from CuO to metallic Cu diffraction peaks was observed, suggesting the total reduction of 30wt% Cu_2Zr_1-H-MCM-22 into metallic Cu, H-MCM-22 and amorphous ZrO_2 at approximately 413 K. However, for amorphous ZrO_2, this shift was not noticeable due to the amorphous structure. The $Cu_2Zr_1O_x$ results demonstrate an evident shift in the peaks from CuO to metallic copper, they also indicate the presence of ZrO_2, representing different ZrO_2 structures with zeolite support.

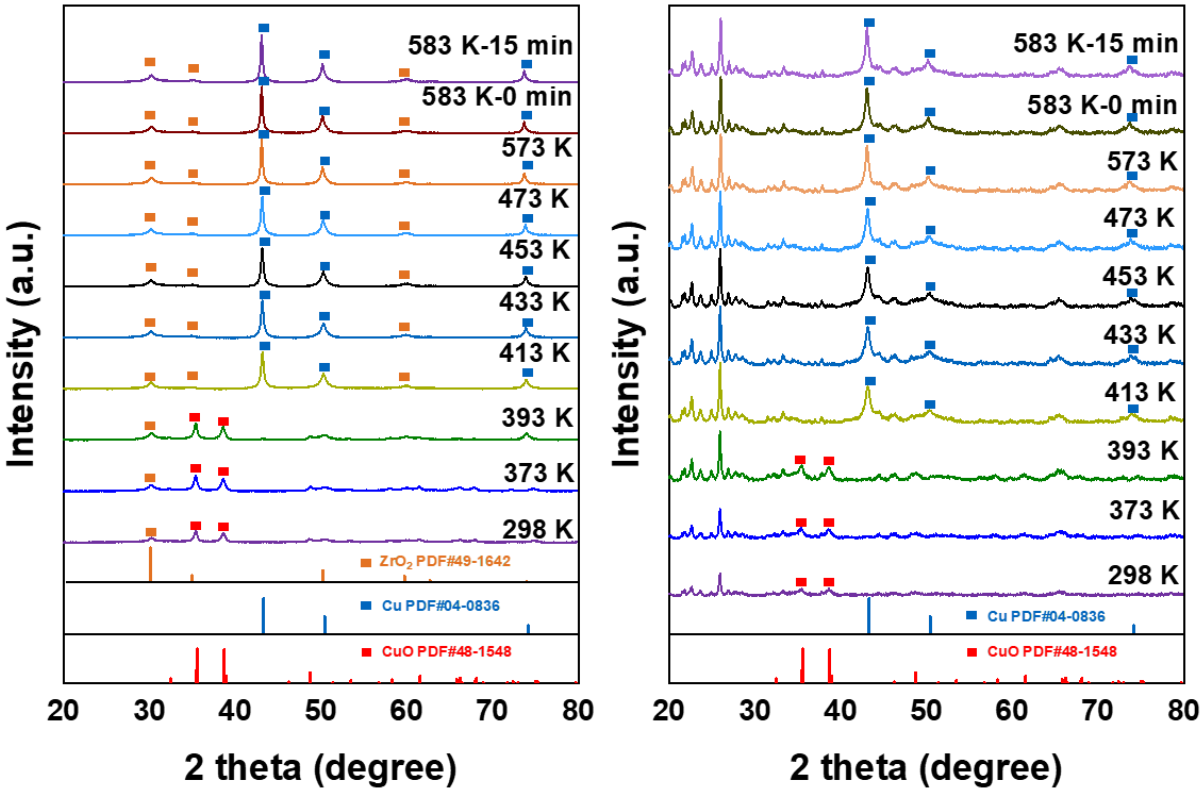

Figure 4-11. In situ XRD patterns of (**Left**) $Cu_2Zr_1O_x$ and (**Right**) 30wt% Cu_2Zr_1-H-MCM-22 in CO_2 hydrogenation at 1bar.

4.4.5 Comparison with other catalytic systems

The establishment of the references space time yield (STY) and conversion of DME for one step to synthesis DME from CO_2 hydrogenation is demonstrated in **Figure 4-12**[19-30]. A comparison of Cu_2Zr_1-H-MCM-22 with the other benchmark catalysts reveals that the space time yield (STY) of DME is significantly higher than that of all other catalysts and exceeds the highest STY_{DME} reference value. It is evident that the Cu_2Zr_1-H-MCM-22 catalyst demonstrates a high level of foresight in the synthesis of DME in a single step.

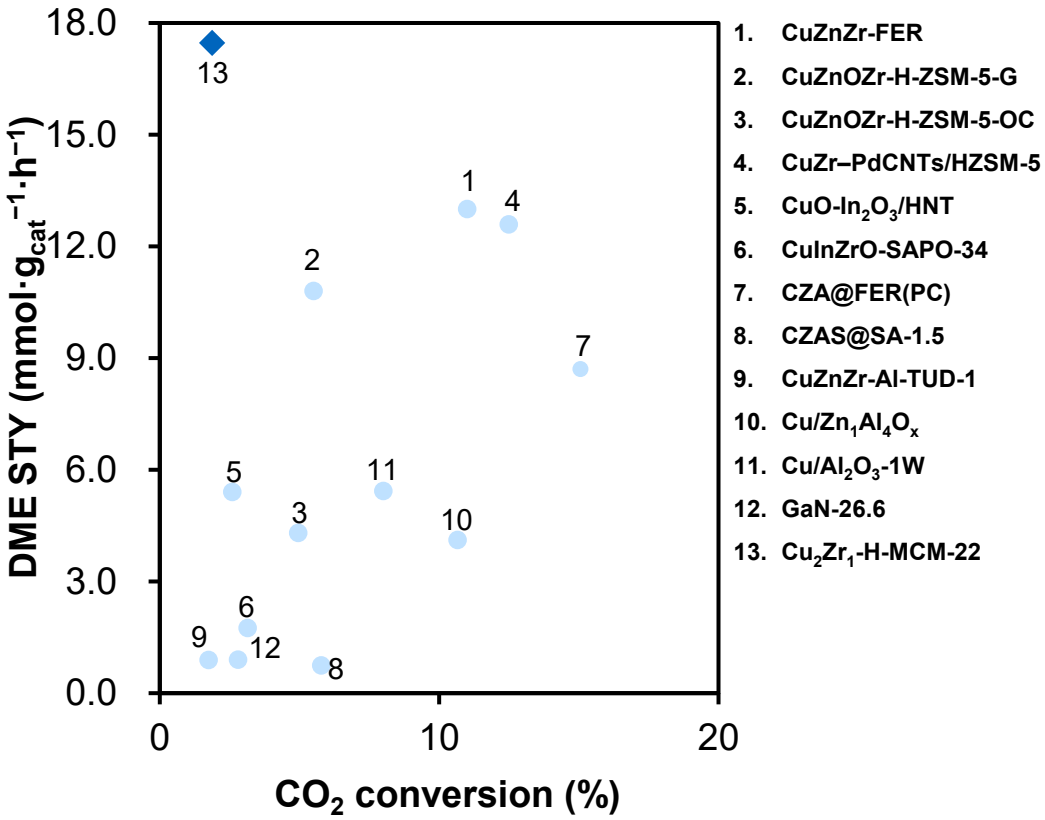

Figure 4-12. Comparison of the Cu_2Zr_1-H-MCM-22 catalyst with the reported DME synthesis catalysts. All the experiments are regarded as CO free and analyzed at 1-5 MPa, 1-150 $L \cdot g_{cat}^{-1} \cdot h^{-1}$, and 150-350 °C.

4.5 Conclusion

The direct synthesis of dimethyl ether (DME) from CO_2 hydrogenation represents a promising pathway for carbon-neutral fuel production, integrating methanol synthesis (MS) and CH_xO intermediate dehydration (MD) into a single-step process. This approach has been demonstrated to enhance CO_2 conversion efficiency and eliminate the need for intermediate methanol separation, thereby improving process economics and energy utilization. The catalytic performance in the one-step CO_2 to DME reaction is governed by the interplay between the metal oxide component, responsible for CO_2 activation and hydrogenation, and the solid acid component, which facilitates methanol intermediate dehydration. Optimized bifunctional catalysts, such as Cu-ZrO_x combined with H-MCM-22, exhibit superior activity and selectivity due to their well-balanced metal-acid synergy. It is imperative to suppress the reverse water-gas shift (RWGS) reaction in order to minimize CO formation and optimize DME yield.

Notwithstanding the considerable progress that has been made, challenges persist with regard to catalyst stability, deactivation due to water accumulation, and undesired secondary reactions that result in hydrocarbon formation. Future research should focus on improving catalyst durability, optimizing reaction conditions, and developing novel hybrid catalytic materials with enhanced metal-support interactions and tailored acidity. Additionally, mechanistic insights from operando spectroscopy and kinetic modeling will be crucial for guiding the rational design of next-generation catalysts.

In conclusion, the one-step CO_2 to DME synthesis provides an efficient and scalable route for CO_2 valorization, offering a sustainable alternative to produce clean fuels and chemicals in the transition toward a low carbon economy.

4.6 Acknowledgements

C. L. is grateful to the Chinese Scholarship Council for financial support.

4.7 Appendix

Figure. S4-1.

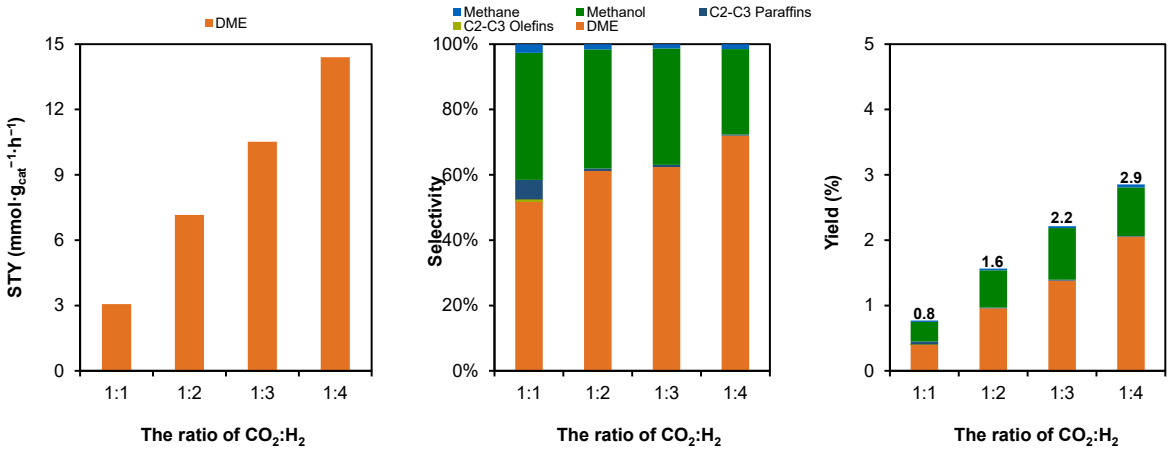

Figure. S4-1. Catalytic performance of Cu_2Zr_1-H-MCM-22 catalysts prepared using different CO_2/H_2 ratio from 1/1-1/4. All the experiments are regarded as CO free and analyzed at 300 °C, 5.0 MPa, space velocity = 150 $L \cdot g_{cat}^{-1} \cdot h^{-1}$. Controlling CO_2 as 9 mL/min and changing the ratio of H_2.

Figure. S4-2.

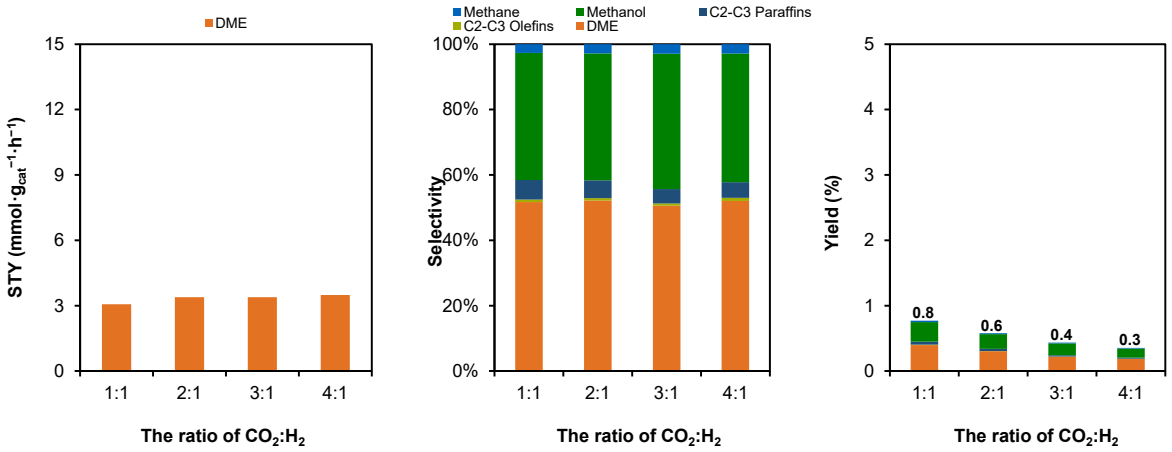

Figure. S4-2. Catalytic performance of Cu_2Zr_1-H-MCM-22 catalysts prepared using different CO_2/H_2 ratio from 1/1-4/1. All the experiments are regarded as CO free and analyzed at 300 °C, 5.0 MPa, space velocity = 150 $L \cdot g_{cat}^{-1} \cdot h^{-1}$. Controlling H_2 as 9 mL/min and changing the ratio of CO_2.

Figure. S4-3.

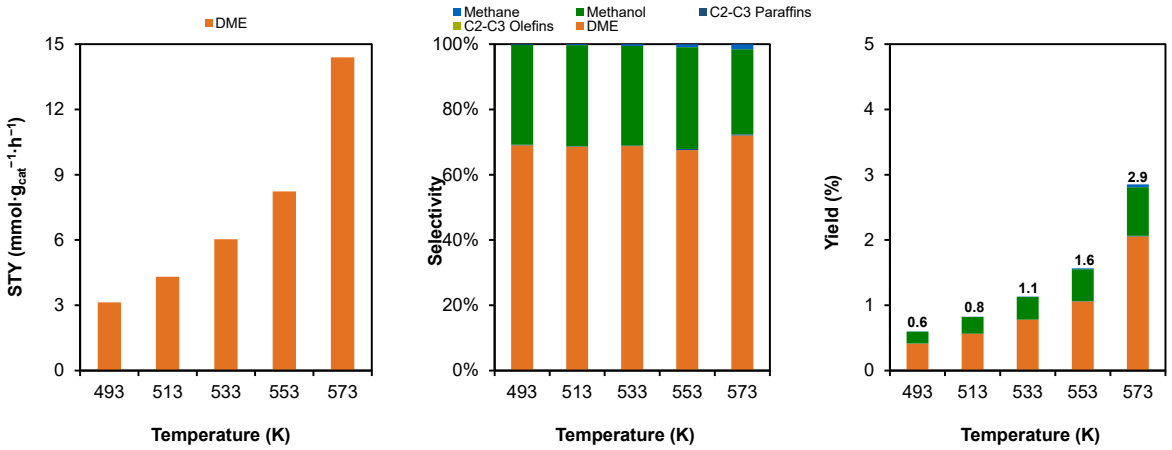

Figure. S4-3. Catalytic performance of Cu_2Zr_1-H-MCM-22 catalysts prepared using different temperatures. All the experiments are regarded as CO free and analyzed at 220-300 °C, 5.0 MPa, space velocity = 150 $L \cdot g_{cat}^{-1} \cdot h^{-1}$.

Figure. S4-4.

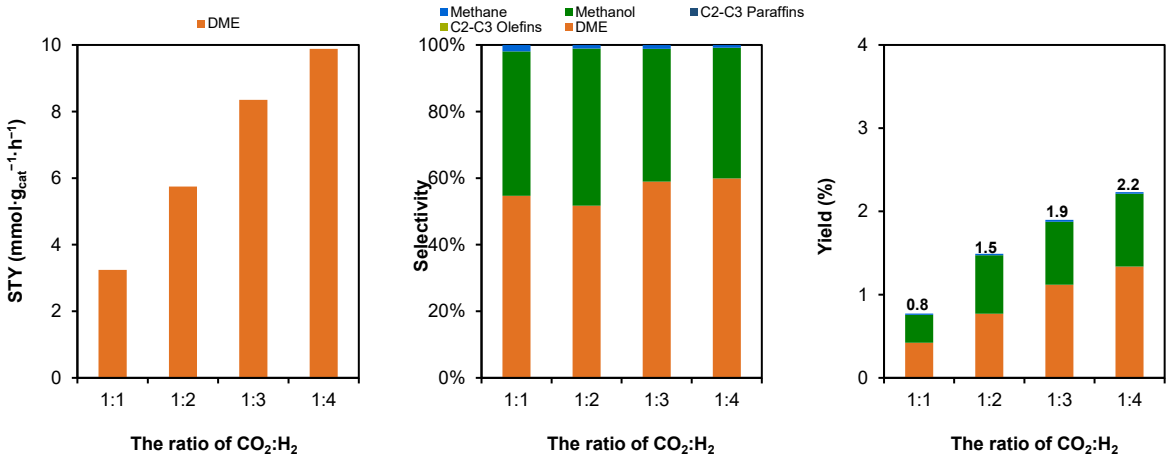

Figure. S4-4. Catalytic performance of Cu_2Zr_1-$Si_1Al_1O_x$ catalyst prepared using different CO_2/H_2 ratio from 1/1-1/4. All the experiments are regarded as CO free and analyzed at 300 °C, 5.0 MPa, space velocity = 150 $L \cdot g_{cat}^{-1} \cdot h^{-1}$. Controlling CO_2 as 9 mL/min and changing the ratio of H_2.

Figure. S4-5.

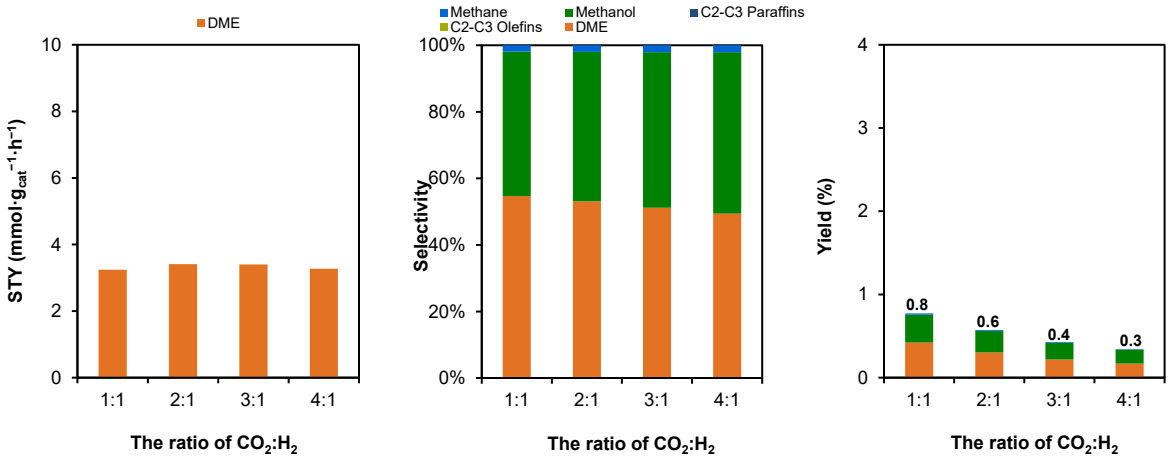

Figure. S4-5. Catalytic performance of Cu_2Zr_1-$Si_1Al_1O_x$ catalyst prepared using different CO_2/H_2 ratio from 1/1-4/1. All the experiments are regarded as CO free and analyzed at 300 °C, 5.0 MPa, space velocity = 150 $L \cdot g_{cat}^{-1} \cdot h^{-1}$. Controlling H_2 as 9 mL/min and changing the ratio of CO_2.

Figure. S4-6.

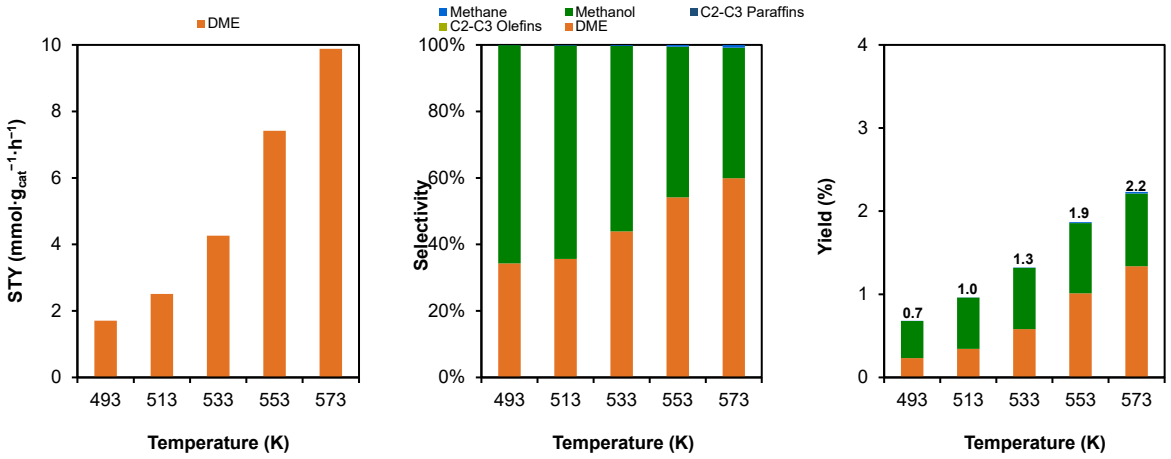

Figure. S4-6. Catalytic performance of Cu_2Zr_1-$Si_1Al_1O_x$ catalysts prepared using different temperatures. All the experiments are regarded as CO free and analyzed at 220-300 °C, 5.0 MPa, space velocity = 150 $L \cdot g_{cat}^{-1} \cdot h^{-1}$.

Figure. S4-7.

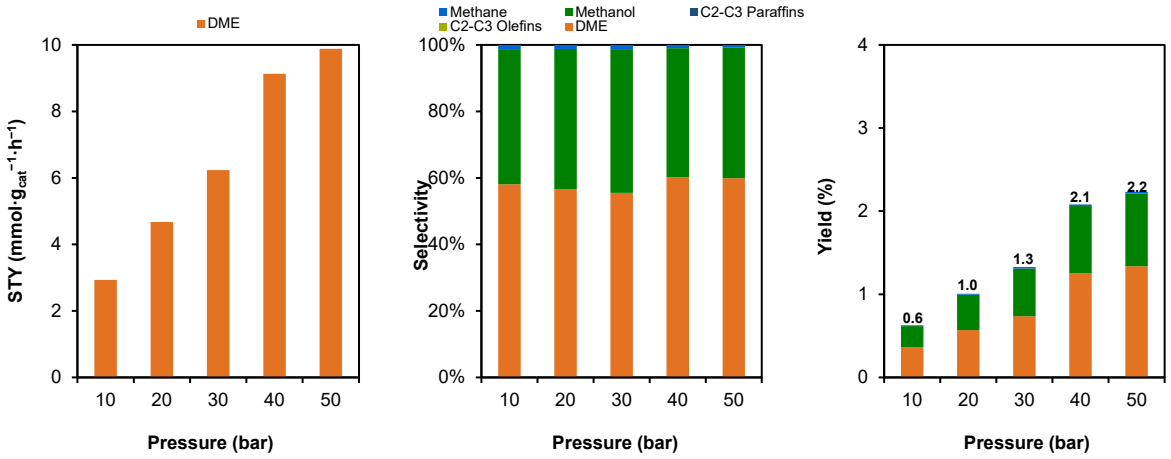

Figure. S4-7. Catalytic performance of Cu_2Zr_1-$Si_1Al_1O_x$ catalysts prepared using different pressures. All the experiments are regarded as CO free and analyzed at 300 °C, 1.0-5.0 MPa, space velocity = 150 $L \cdot g_{cat}^{-1} \cdot h^{-1}$.

Figure. S4-8.

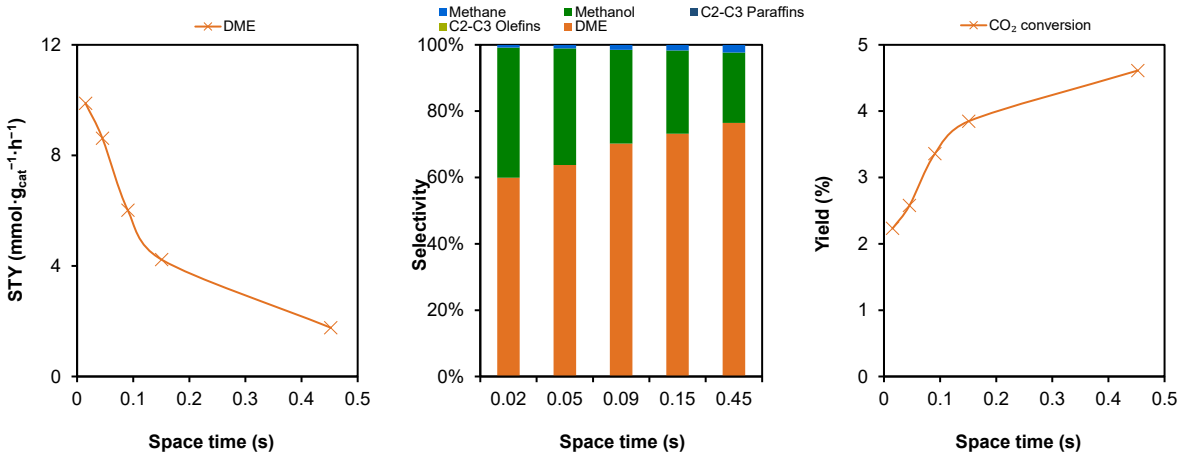

Figure. S4-8. Catalytic performance of Cu_2Zr_1-$Si_1Al_1O_x$ catalysts prepared using different space time. All the experiments are regarded as CO free and analyzed at 300 °C, 5.0 MPa, Space time = 0.02-0.45 s.

Figure. S4-9.

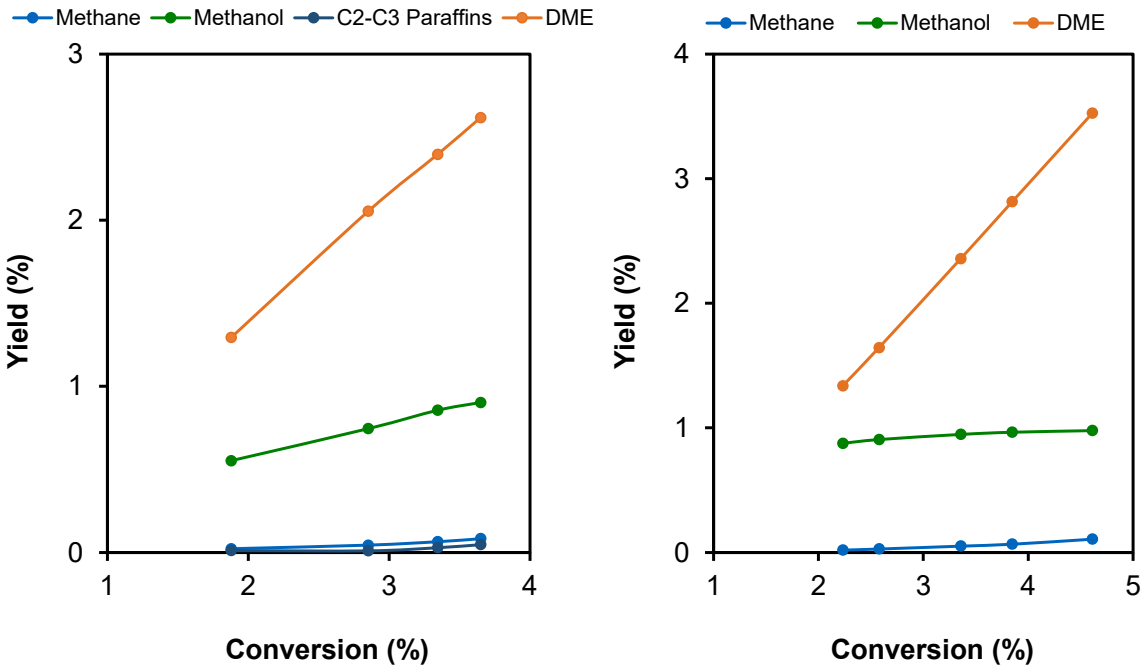

Figure. S4-9. (**Left**) Methane, methanol, C_2-C_3 paraffins and DME catalytic yield for 30 wt% Cu_2Zr_1-H-MCM-22 with CO_2 conversion shift. (**Right**) Methane, methanol and DME catalytic yield for 30 wt% Cu_2Zr_1-$Si_1Al_1O_x$ with CO_2 conversion shift. All the experiments are regarded as CO free and analyzed at 300°C, 5.0 MPa, space time = 0.02-0.45 s, H_2/CO_2 = 4.

Figure. S4-10.

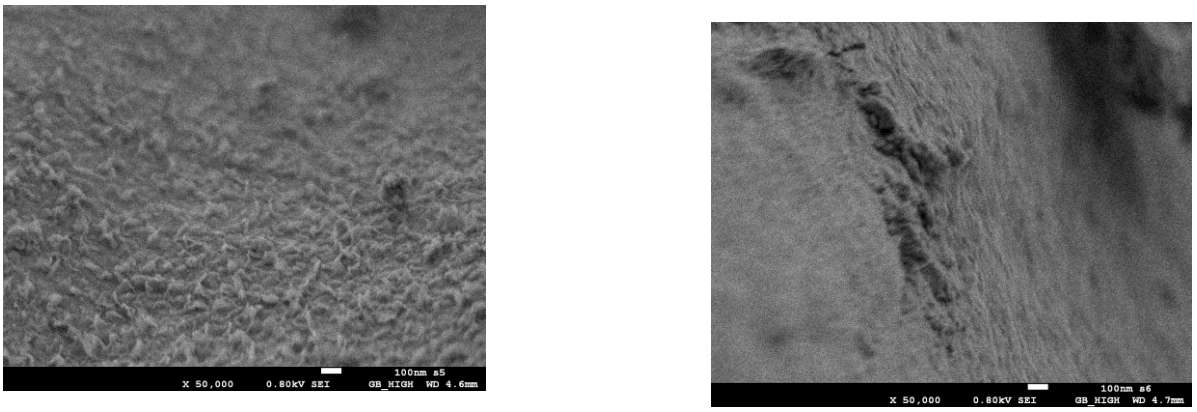

$Si_1Al_1O_x$ 30wt% Cu_2Zr_1-$Si_1Al_1O_x$

Figure. S4-10. SEM images of $Si_1Al_1O_x$ and 30wt% Cu_2Zr_1-$Si_1Al_1O_x$ catalysts.

Figure. S4-11.

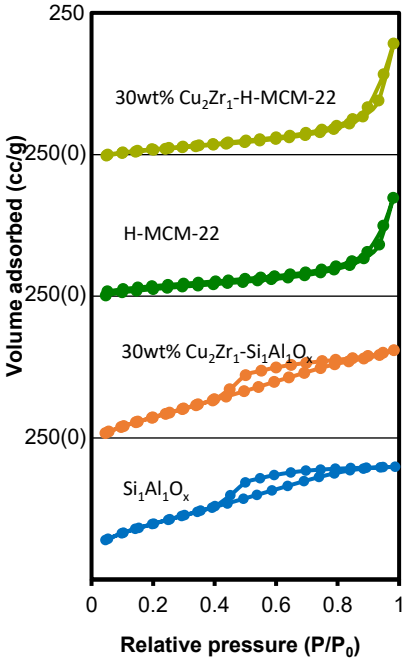

Figure. S4-11. N_2 adsorption-desorption isotherm of H-MCM-22, 30wt% Cu_2Zr_1-H-MCM-22, $Si_1Al_1O_x$ and 30wt% Cu_2Zr_1-$Si_1Al_1O_x$ catalysts

Table. S4-1.

Catalysts	Surface area (m^2/g)
H-MCM-22	**281.52**
30wt% Cu_2Zr_1-H-MCM-22	**299.38**
$Si_1Al_1O_x$	**350.45**
30wt% Cu_2Zr_1-$Si_1Al_1O_x$	**354.46**

Table. S4-1. The surface area of all the reduced catalyst.

Table. S4-2.

Surface species	Wavenumber (cm^{-1})	Ref.
CH_4	3015, 1303	ACS Catal. 2023, 13, 7, 4667–4674 Angew. Chem. Int. Ed. 2020, 59, 19983–19989
$*CH_x$	3017, 2966, 2956, 2928, and 2856	Appl. Catal., B 2021, 298, 120567 J. Phys. Chem. C 2011, 115, 1361–1367
$*CH_xO$	2937-2941 1070-1082 2824-2826 1270, 1034	ACS Catal. 2020, 10, 24, 14516–14526 ACS Catal. 2023, 13, 7, 4667–4674 ACS Catal. 2020, 10, 21, 12828–12840
Gaseous CO	2176, 2110, 2085	ACS Catal. 2020, 10, 9, 5250–5260 ACS Catal. 2023, 13, 7, 4667–4674
Bridged carbonyl species	1900-2060	Nat. Catal., 2018, 127–134
*HCOO	1337-1393 1593-1622	ACS Catal. 2023, 13, 7, 4667–4674 ACS Catal. 2020, 10, 24, 14516–14526
-C-O-C-	1100-1200	Chem. Eng. Technol 2025, 48, 5, e70004
$*CO_3$	1393, 1325 and 1274	ACS Catal. 2023, 13, 7, 4667–4674 Appl. Catal., A 2025, 288, 126-133

Table. S4-2. The assignments of IR bands in the DRIFTS spectra.

4.8 Reference

1 C. Niamnuy, P. Prapaitrakul, N. Panchan *et al.* Synthesis of Dimethyl Ether via CO_2 Hydrogenation: Effect of the Drying Technique of Alumina on Properties and Performance of Alumina-Supported Copper Catalysts. *ACS Omega*, 5 (2020) 2334-2344.

2 W. Zhou, J. Kang, K. Cheng *et al.* Direct Conversion of Syngas into Methyl Acetate, Ethanol, and Ethylene by Relay Catalysis via the Intermediate Dimethyl Ether. *Angew. Chem. Int. Ed*, 57 (2018) 12012-12016.

3 K. P. Cao, D. Fan, L. Y. Li *et al.* Insights into the Pyridine-Modified MOR Zeolite Catalysts for DME Carbonylation. *Acs Catal.*, 10 (2020) 3372-3380.

4 W. H. Feng, M. M. Yu, L. J. Wang *et al.* Insights into Bimetallic Oxide Synergy during Carbon Dioxide Hydrogenation to Methanol and Dimethyl Ether over $GaZrO_x$ Oxide Catalysts. *ACS Catal.*, 11 (2021) 4704-4711.

5 N. Mota, E. M. Ordoñez, B. Pawelec, J. L. G. Fierro & R. M. Navarro. Direct Synthesis of Dimethyl Ether from CO_2: Recent Advances in Bifunctional/Hybrid Catalytic Systems. *Catalysts*, 11 (2021) 411.

6 J. Sun, G. H. Yang, Y. Yoneyama & N. Tsubaki. Catalysis Chemistry of Dimethyl Ether Synthesis. *ACS Catal.*, 4 (2014) 3346-3356.

7 H. Bahruji, R. D. Armstrong, J. R. Esquius *et al.* Hydrogenation of CO_2 to Dimethyl Ether over Brønsted Acidic PdZn Catalysts. *Ind. Eng. Chem. Res.*, 57 (2018) 6821-6829.

8 H. Ham, S. W. Baek, C. H. Shin & J. W. Bae. Roles of Structural Promoters for Direct CO_2 Hydrogenation to Dimethyl Ether over Ordered Mesoporous Bifunctional Cu/M–Al_2O_3 (M = Ga or Zn). *ACS Catal.*, 9 (2018) 679-690.

9 A. A. Ye, Z. R. Li, J. Q. Ding, W. Xiong & W. X. Huang. Synergistic Catalysis of Al and Zn Sites of Spinel $ZnAl_2O_4$ Catalyst for CO Hydrogenation to Methanol and Dimethyl Ether. *ACS Catal.*, 11 (2021) 10014-10019.

10 S. J. Ren, W. R. Shoemaker, X. F. Wang *et al.* Highly active and selective Cu-ZnO based catalyst for methanol and dimethyl ether synthesis via CO_2 hydrogenation. *Fuel*, 239 (2019) 1125-1133.

11 T. T. N. Vu, A. Desgagnés & M. C. Iliuta. Efficient approaches to overcome challenges in material development for conventional and intensified CO_2 catalytic hydrogenation to CO, methanol, and DME. *Appl. Catal., A*, 617 (2021) 118119.

12 G. Bonura, C. Cannilla, L. Frusteri & F. Frusteri. The influence of different promoter oxides on the functionality of hybrid CuZn-ferrierite systems for the production of DME from CO_2-H_2 mixtures. *Appl. Catal., A*, 544 (2017) 21-29.

13 M. Mureddu, S. Lai, L. Atzori *et al.* Ex-LDH-Based Catalysts for CO_2 Conversion to Methanol and Dimethyl Ether. *Catalysts*, 11 (2021) 615.

14 A. D'Ambrosio, A. Bertino, S. Todaro *et al.* Kinetic Modeling of the Direct Dimethyl Ether (DME) Synthesis over Hybrid Multi-Site Catalysts. *Catalysts*, 14 (2024) 61.

15 D. Kubas, M. Gierse, O. Salem & I. Krossing. Is Direct DME Synthesis Superior to Methanol Production in Carbon Dioxide Valorization? From Thermodynamic Predictions to Experimental Confirmation. *ACS Catal.*, 13 (2023) 3960-3970.

16 X. Wang, S. Y. Jeong, H. S. Jung & J. W. Bae. Tandemly coupled CO_2 hydrogenation and carbonylation on SiO_2-encapsulated Cu-ZnO nanoparticles with Ferrierite zeolite toward selective synthesis of oxygenates. *Appl. Catal., B*, 348 (2024) 123829.

17 A. Alvarez, A. Bansode, A. Urakawa *et al.* Challenges in the Greener Production of Formates/Formic Acid, Methanol, and DME by Heterogeneously Catalyzed CO_2 Hydrogenation Processes. *Chem. Rev.*, 117 (2017) 9804-9838.

18 C. Liu & Z. W. Liu. Perspective on CO_2 Hydrogenation for Dimethyl Ether Economy. *Catalysts*, 12 (2022) 1375.

19 G. Bonura, M. Cordaro, L. Spadaro *et al.* Hybrid Cu–ZnO–ZrO_2/H-ZSM5 system for the direct synthesis of DME by CO_2 hydrogenation. *Appl. Catal., B*, 140-141 (2013) 16-24.

20 X. J. Cui, W. J. Yan, H. H. Yang *et al.* Preserving the Active Cu–ZnO Interface for Selective Hydrogenation of CO_2 to Dimethyl Ether and Methanol. *ACS Sustainable Chem. Eng.*, 9 (2021) 2661-2672.

21 F. Frusteri, M. Cordaro, C. Cannilla & G. Bonura. Multifunctionality of Cu–ZnO–ZrO_2/H-ZSM5 catalysts for the one-step CO_2-to-DME hydrogenation reaction. *Appl. Catal., B*, 162 (2015) 57-65.

22 F. Frusteri, M. Migliori, C. Cannilla *et al.* Direct CO_2-to-DME hydrogenation reaction: New evidences of a superior behaviour of FER-based hybrid systems to obtain high DME yield. *J. CO2 Util.*, 18 (2017) 353-361.

23 Q. Jiang, Y. F. Liu, T. Dintzer *et al.* Tuning the highly dispersed metallic Cu species via manipulating Brønsted acid sites of mesoporous aluminosilicate support for CO_2 hydrogenation reactions. *Appl. Catal., B*, 269 (2020) 118804.

24 A. Pechenkin, D. Potemkin, M. Rubtsova *et al.* CuO-In_2O_3 Catalysts Supported on Halloysite Nanotubes for CO_2 Hydrogenation to Dimethyl Ether. *Catalysts*, 11 (2021) 1151.

25 L. X. Song, G. B. Liu & Z. P. Qu. Controlling CO_2 hydrogenation selectivity by tuning surface properties of Cu/$Zn_xAl_yO_z$ catalysts. *Chem. Eng. J.*, 494 (2024) 153206.

26 X. Wang, S. Y. Jeong, H. S. Jung *et al.* Catalytic activity for direct CO_2 hydrogenation to dimethyl ether with different proximity of bifunctional Cu-ZnO-Al_2O_3 and ferrierite. *Appl. Catal., B*, 327 (2023) 122456.

27 L. B. Yao, X. C. Shen, Y. B. Pan & Z. M. Peng. Unravelling Proximity-Driven Synergetic Effect within CIZO–SAPO Bifunctional Catalyst for CO_2 Hydrogenation to DME. *Energy Fuels*, 34 (2020) 8635-8643.

28 M. H. Zhang, Z. M. Liu, G. D. Lin & H. B. Zhang. Pd/CNT-promoted $CuZrO_2$/HZSM-5 hybrid catalysts for direct synthesis of DME from CO_2/H_2. *Appl. Catal., A*, 451 (2013) 28-35.

29 C. Liu, J. Kang, Z. Q. Huang *et al.* Gallium nitride catalyzed the direct hydrogenation of carbon dioxide to dimethyl ether as primary product. *Nat. Commun.*, 12 (2021) 2305.

30 X. W. Song, C. S. Yang, X. H. Li *et al.* On the Role of Hydroxyl Groups on Cu/Al_2O_3 in CO_2 Hydrogenation. *ACS Catal.*, 12 (2022) 14162-14172.

Chapter 5

Summary and Conclusions

The catalytic hydrogenation of CO_2 into value added chemicals and fuels represents a cornerstone challenge in sustainable chemistry, vital for achieving carbon neutrality and advancing carbon management technologies. This dissertation systematically explores rational catalyst design strategies to direct CO_2 hydrogenation toward targeted products like paraffins, olefins, oxygenates (e.g., ethanol), and ethers (notably dimethyl ether, DME) by precisely controlling key elementary steps, including C-O bond cleavage, C-H bond formation, and C-C coupling. Through the synthesis of three distinct catalyst systems, comprehensive mechanistic investigations, and kinetic analyses, this work establishes fundamental principles for selectively valorizing CO_2.

In the first part, Na doped Co_3O_4 catalysts were designed to modulate the electronic and structural properties of cobalt active sites. Sodium incorporation induced the formation of oxygen vacancies and altered the electron density around cobalt centers, thereby weakening the adsorption strength of CO_2 derived intermediates and suppressing excessive C-O and C-H bond cleavage. Characterization via H_2 TPD, H_2 TPR, XPS, and in situ DRIFTS revealed that Na doping reduced catalyst reducibility and stabilized intermediate species against deep hydrogenation. As a result, the catalysts displayed enhanced selectivity toward C_2+ hydrocarbons, particularly paraffins and olefins with lower reaction temperatures. These findings underscore the importance of electronic structure regulation and surface basicity enhancement in steering CO_2 hydrogenation pathways.

The second strategy focused on bimetallic $CoCuZrO_x$ catalysts and their Na-modified variants to promote oxygenate formation through CH_x and CH_xO coupling mechanisms. Here, as for fcc-Co, CO* is easier to desorb to CO product with a lower CO* desorption energy comparing with hcp-Co, appearing lower C-O bond cleavage and higher oxygenates selectivity by combining CH_x and CH_xO intermediates. Sodium doping further suppressed over hydrogenation steps from CH_2 to CH_3, stabilizing reactive CH_x intermediates and enhancing C-C bond formation between CH_x and CH_xO fragments. Operando spectroscopy and kinetic isotope labeling studies confirmed that modulating hydrogen spillover dynamics and balancing intermediate reactivity were critical for maximizing ethanol selectivity. This work highlights the value of engineering synergistic metal and metal oxide interfaces and controlling intermediate lifetimes for selective CO_2 conversion to oxygenates.

In the third section, a bifunctional catalyst combining $CuZrO_x$ nanoparticles with H-MCM-22 zeolite was developed to achieve direct one-step CO_2 to DME synthesis. Cu-ZrO_x domains catalyzed CO_2 hydrogenation to methanol, while the adjacent H-MCM-22 acid sites

facilitated intermediate methanol dehydration to DME. This spatial integration minimized the diffusion length for methanol intermediates and overcame thermodynamic equilibrium limitations. Mechanistic studies revealed that proximity between hydrogenation and dehydration sites significantly enhanced tandem reaction efficiency and suppressed undesirable side reactions, such as RWGS and methanol over-hydrogenation. Moreover, the microporous structure of H-MCM-22 provided a confined environment that stabilized reactive intermediates and improved dehydration kinetics, demonstrating the critical role of pore architecture and proximity engineering in tandem catalysis.

Overall, this dissertation establishes a unified mechanistic framework for CO_2 hydrogenation, emphasizing that precise control over elementary reaction steps, intermediate coupling, adsorption energies, and catalyst site architecture is essential to achieving high selectivity and efficiency. Major scientific contributions include the demonstration of Na doping for tuning cobalt catalysts' reactivity, the elucidation of bimetallic synergy in promoting oxygenate formation, and the successful design of spatially coupled bifunctional systems for DME production.

Looking ahead, future advances in CO_2 hydrogenation could be realized through atomically engineered active sites, such as single-atom catalysts or heterostructure alloys, and by integrating thermal catalysis with emerging fields such as plasma activation or electrocatalysis. Furthermore, coupling operando spectroscopy with microkinetic modeling will deepen the understanding of transient intermediates and guide rational catalyst optimization. Lastly, scaling up these processes with renewable hydrogen sources and integrating with efficient CO_2 capture technologies will be critical to closing the carbon loop and enabling industrial implementation.

This work not only advances fundamental knowledge of CO_2 hydrogenation mechanisms but also lays important groundwork for the next generation of catalyst systems capable of selectively transforming carbon dioxide into strategic fuels and chemicals under industrially relevant conditions.

Chapter 6

Zusammenfassung und Folgerungen

Die katalytische Wasserstoffierung von CO_2 zu wertvollen Chemikalien und Kraftstoffen stellt eine Schlüsselherausforderung in der nachhaltigen Chemie dar, die von entscheidender Bedeutung für das Erreichen von Klimaneutralität und die Weiterentwicklung von Kohlenstoffmanagement Technologien ist. In dieser Dissertation wurden Strategien zur rationalen Katalysatorentwicklung untersucht, um die CO_2 Wasserstoffierung gezielt auf verschiedene Zielprodukte, Paraffine, Olefine, Sauerstoffverbindungen (z. B. Ethanol) und Ether (insbesondere Dimethylether, DME) zu lenken, indem zentrale elementare Reaktionsschritte wie C-O Bindungsspaltung, C-H Bindungsbildung und C-C Kopplung gezielt gesteuert wurden. Durch die Synthese von drei unterschiedlichen Katalysatorsystemen, umfassende mechanistische Untersuchungen und kinetische Analysen wurden grundlegende Prinzipien für eine selektive CO_2 Valorisierung etabliert.

Im ersten Teil wurden Na dotierte Co_3O_4 Katalysatoren entwickelt, um die elektronischen und strukturellen Eigenschaften der aktiven Kobaltzentren gezielt zu modulieren. Die Einführung von Natrium förderte die Bildung von Sauerstoffleerstellen und veränderte die Elektronendichte an den Kobaltzentren, wodurch die Adsorptionsstärke von CO_2 abgeleiteten Intermediaten verringert und eine übermäßige Spaltung von C-O und C-H Bindungen unterdrückt wurde. Charakterisierungen mittels H_2 TPD, CO_2 TPD, XPS und in-situ DRIFTS zeigten, dass die Natriumdotierung die Reduzierbarkeit der Katalysatoren minderte und die Stabilisierung reaktiver Zwischenprodukte begünstigte. Daraus resultierte eine erhöhte Selektivität hin zu C_2+ Kohlenwasserstoffen, insbesondere Paraffinen und Olefinen, bei niedrigeren Reaktionstemperaturen. Diese Ergebnisse verdeutlichen die Bedeutung der elektronischen Feinabstimmung und Oberflächenbasizitätskontrolle für die Lenkung von CO_2 Hydrierungspfaden.

Die zweite Strategie konzentrierte sich auf bimetallische $CoCuZrO_x$ Katalysatoren und deren Na-modifizierte Varianten zur Förderung der Sauerstoffatombildung durch CH_x und CH_xO Kopplungsmechanismen. Hier ist CO* wie bei fcc-Co leichter zu CO-Produkt zu desorbieren, da es im Vergleich zu hcp-Co eine geringere CO* Desorptionsenergie aufweist, was zu einer geringeren C-O-Bindungsaufspaltung und einer höheren Selektivität für Sauerstoffverbindungen durch die Kombination von CH_x und CH_xO Zwischenprodukten führt. Die Natriumdotierung unterdrückte zudem die Überhydrierung von CH_2 zu CH_3, stabilisierte reaktive Zwischenprodukte und erhöhte die C-C Kopplungseffizienz zwischen CH_x und CH_xO Fragmente. Operando-Spektroskopie und kinetische Isotopenmarkierungsstudien bestätigten, dass die Steuerung der Wasserstoff Übertragung (Spillover) und die Reaktivitätsbalance der

Zwischenprodukte entscheidend für eine hohe Ethanolausbeute waren. Diese Arbeiten unterstreichen die Bedeutung der gezielten Gestaltung synergistischer Metall metalloxid schnittstellen.

Im dritten Abschnitt wurde ein bifunktionaler Katalysator bestehend aus $CuZrO_x$ Nanopartikeln und H-MCM-22-Zeolith entwickelt, um die direkte einstufige CO_2 zu DME synthese zu realisieren. Cu-ZrO_x Bereiche katalysierten die CO_2 Wasserstoffierung zu Methanol, während angrenzende saure Zentren im H-MCM-22 den Zwischenstufige Methanol-Dehydratisierung zu DME ermöglichten. Diese räumliche Integration minimierte Diffusionswege für Zwischenprodukte und überwand thermodynamische Gleichgewichtsbeschränkungen. Mechanistische Untersuchungen zeigten, dass die Nähe der aktiven Zentren die Tandemreaktionseffizienz erheblich verbesserte und Nebenreaktionen wie die RWGS-Reaktion und Überhydrierung von Methanol unterdrückte. Die mikroporöse Struktur von H-MCM-22 stabilisierte zudem reaktive Zwischenprodukte und beschleunigte die Dehydratisierungskinetik.

Zusammenfassend etabliert diese Dissertation ein umfassendes mechanistisches Rahmenwerk für die CO_2 Hydrierung und zeigt auf, dass die präzise Kontrolle elementarer Reaktionsschritte, die gezielte Kopplung von Zwischenprodukten, die Steuerung von Adsorptionsenergien sowie die architektonische Gestaltung der aktiven Zentren entscheidend für eine hohe Selektivität und Effizienz sind. Wesentliche wissenschaftliche Beiträge dieser Arbeit umfassen den Nachweis der Reaktivitätsmodulation von Kobaltkatalysatoren durch Natriumdotierung, die Aufklärung der synergistischen Mechanismen in bimetallischen Systemen zur Förderung von Sauerstoffaten sowie die erfolgreiche Gestaltung von bifunktionalen Katalysatorsystemen für die direkte DME synthese.

Zukünftige Fortschritte auf diesem Gebiet könnten durch die Entwicklung atomar präziser aktiver Zentren und beispielsweise Ein Atom Katalysatoren oder Heterostrukturlegierungen und die Integration thermischer Katalyse mit aufkommenden Technologien wie Plasmaaktivierung oder Elektrokatalyse erzielt werden. Darüber hinaus wird die Kombination von operando-Spektroskopie mit mikroskopischer Kinetikmodellierung das Verständnis transienter Zwischenprodukte vertiefen und eine gezielte Katalysatoroptimierung ermöglichen. Schließlich wird die Skalierung dieser Prozesse durch die Nutzung erneuerbarer Wasserstoffquellen und die Kopplung mit effizienten CO_2 Abscheidungstechnologien entscheidend für die industrielle Umsetzung sein.

Diese Arbeit leistet nicht nur fundamentale Beiträge zum besseren Verständnis der CO_2 Hydrierungsmechanismen, sondern legt auch das wissenschaftliche Fundament für die

Entwicklung der nächsten Generation von Katalysatorsystemen, die CO_2 selektiv und effizient unter industrierelevanten Bedingungen in strategische Produkte umwandeln können.

List of Publications

Journals

Chuanlei Li, Xiaonan Tan, Jiahai Ma, Concerted high innergenerated-H_2O_2 photocatalysis and Photo-Fenton degradation of organic pollutants over SCNO@CdS. J. Photochem. Photobiol. A: Chem., 420 (2021) 113477

Chuanlei Li, Ruixue Zhao and Johannes A. Lercher* "Tuning sodium mass ratio in cobalt oxide catalysts to modulate paraffin and olefin selectivity in CO_2 hydrogenation", (in preparation)

Chuanlei Li, Ruixue Zhao and Johannes A. Lercher* "Optimizing Co-Cu-ZrO_x catalysts for enhanced ethanol production from CO_2 through intermediate modulation", (in preparation)

Chuanlei Li, Ruixue Zhao and Johannes A. Lercher* "Multifunctionality of Cu_2Zr_1-H-MCM-22 catalysts for the one-step CO_2 hydrogenation to DME", (in preparation)

Poster Presentation

Chuanlei Li, Ruixue Zhao and Johannes A. Lercher* "Optimizing $CoCuZrO_x$ catalysts for enhanced ethanol production from CO_2 through intermediate modulation", P40. 100 Years Fischer-Tropsch Process, Mülheim an der Ruhr (Germany), 05/2025.